Université de Québec

Institut National de la Recherche Scientifique

Énergie Matériaux Télécommunications

Transparent Conducting Oxides and Multiferroic Perovskites for Solar Energy Conversion Applications

Wei Huang

Thèse présentée pour l'obtention

du grade de Philosophiæ Doctor (Ph.D.)

en Sciences de l'énergie et des matériaux

Jury d'évaluation

Président du jury et examinateur interne	Emanuele Orgiu INRS ÉMT
Examinateur externe	Jonathan Spanier Drexel University
Examinateur externe	Jean-Michel Nunzi Queen's University
Directeur de recherche	Federico Rosei INRS ÉMT
Co-directeur de recherche	Mohamed Chaker INRS ÉMT
Co-directeur de recherche	Riad Nechache ÉTS

Contents

Abstract

Clean and sustainable solar energy is regarded as one of the most reliable and abundant energy sources to replace fossil fuels. To harvest this energy, in the past several decades, the research trend has been towards exploring novel materials and photon-to-electron mechanisms to achieve higher efficiency in solar energy conversion applications, such as photovoltaic (PV) cells. The PV effect is used to directly harvest solar energy by converting the incident photons into following free charge carriers and thus produce electricity. The emerging PV cells mainly differ in how they operate in practice, that is, in the mechanisms that make the sequence of the generation, separation and transport of electronic charge carriers possible. Elucidating those mechanisms is of fundamental importance for understanding the working principle of each solar cell type, and for its further performance optimization. In conventional *p-n* junction based PV cells, the charge separation is determined by the existence of a gradient in the electrochemical potential, also known as intrinsic built-in electric fields. Moreover, solar-driven water splitting and hydrogen generation technologies that produce hydrogen (H_2 gas) and oxygen (O_2 gas) by directly decomposing water using an artificial photocatalytic electrode have been extensively studied as a fundamental technology for the future, due to its simplicity, low-cost operation and the use of nearly neutral pH water, such as seawater for large scale solar-fuel production. In the semiconductor photocatalysts, the carrier extraction is no longer limited by thermodynamic diffusion, but the transport of spatially separated electron-hole pairs to the photocatalyst surface is determined by the surface band bending.

Ferroelectric (FE) oxides have recently emerged as a new alternative pathway to achieve the separation of photo-generated charge carriers, and their application in photon-to-current (e.g., PV cells, photodetectors) and photoelectrochemical (PEC) devices was recently started to be explored. Since the discovery of PV effect in these materials over 50 years ago, ferroelectric devices including solar cells (FESC) and PEC cells have attracted significant attention owing to many unique advantages. This technology involves a simplified structure and fabrication methods as well as stable and abundant materials. Different from the *p*-*n* diode or Schottky diode solar cells, in the FESC, FE polarization plays a dominant role in charge separation and transport. FESC provides reversible directions of photocurrent and photovoltage by polarization direction switching, and also generates above bandgap open-circuit voltages (V_{oc} up to 40 V), which potentially permit to surpass the Shockley-Queisser limit observed in traditional semiconductors cells.

While for a long time such devices were characterized by weak performance values, recent advances led to significant breakthroughs by using multiferroic materials. Multiferroics combine two ferroic functionalities (specifically FE, ferromagnetic or ferroelastic), and typically possess a magnetic order parameter besides the FE one and the electron-electron interaction regulating the magnetic ordering induced a smaller gap (e.g., 2.6–2.7 eV for $BiFeO_3$ and 1.4–2.4 eV for Bi_2FeCrO_6) than other FE materials (e.g., 3.2–3.6 eV for La–doped $Pb(Zr,Ti)O_3$ and 3.2 eV for $BaTiO_3$). Among these multiferroics, double-perovskite Bi_2FeCrO_6 (BFCO) is highly promising in PV and photocatalytic applications due to its nontoxicity, chemical stability, narrow bandgap, huge light absorption coefficient (2.5×10^5 cm^{-1}), large

remnant polarization (55 μC cm^{-2} at room temperature (RT)) and magnetization (160 emu cm^{-3}).

A breakthrough in the field of PV and PEC devices occurred through our recent study on multiferroic BFCO epitaxial thin films, which demonstrated a high efficiency solar energy conversion (solar to electrical or chemical energy). In such material, lower band gap and large FE polarization promote an effective charge carrier generation and separation. Single crystalline BFCO with higher ratio of Fe/Cr cation ordering (R≈0.5−5.1%) showed a lower bandgap (E_g≈1.4−1.8 eV) accompanied with weak FE polarization (P≈5−20 μC cm^{-2}), which exhibit thus a semiconductor behavior. In despite of a larger absorption of sun light by semiconducting BFCO films, the weak FE polarization induced internal electric field decreases the separation power of photogenerated carriers and increases the recombination loss. This dramatically affects the performance of the devices. These results clearly suggest a relationship between the optical property, ferroelectricity and crystal structure of BFCO thin films. To advantageously exploit the semiconducting properties of BFCO for PV application, the *p*-*i*-*n* device architectures have to be designed and developed. Here, an intrinsic semiconductor is sandwiched between a heavily doped *p*- and *n*-layers. Semiconductor material absorbs a certain portion of the solar spectrum and adjacent layers (electrodes) are required to extract the photo-generated carriers for conveyance to an external electrical load.

The *p*-type layer in *p*-*i*-*n* devices is possible incident photons enter the intrinsic absorber layer (*i*-) of the device for conversion into charge carriers. This requires that all other "photo-passive" but functional layers in the PV cell that lie in the path of photons traversing to the absorber should not absorb or back reflect any of the light before it reaches the intrinsic

absorber. That is, the window layers must be highly transparent, i.e., having a wider bandgap than the absorber and thus a much lower absorption coefficient in the spectral range of light used for photo-conversion. Electrically, the *p*-layer should have hole conduction in order to transport the photogenerated holes and block the electrons. Based on these requirements, the *p*-type layer in *p*-*i*-*n* devices should be the *p*-type transparent conducting oxides (*p*-TCOs).

The work performed in this thesis was therefore driven by two main objectives: (1) synthesis and understanding the fundamental physical properties (i.e., structural, electrical, and optical) of *p*-TCOs thin films; (2) design and investigating the multiferroic BFCO thin-film absorber based devices for efficient solar energy conversion applications including photodetectors, PV and PEC devices. The results obtained in this work are resumed in two sections as follows:

In the first section, we synthesized the *p*-type transparent conducting thin films and studied their structural, electrical and optical properties. (1) Perovskite *p*-type In-doped $SrTiO_3$ ($SrIn_xTi_{1-x}O_3$ with In concentration in the range $0 \leq x \leq 0.15$) thin films were grown on $LaAlO_3$ substrates using a pulsed laser deposition (PLD) and molecular beam epitaxy (MBE) combination technique. (2) The In-STO (ISTO, $0.1 \leq x \leq 0.15$) films grown under oxygen pressure of $10^{-7} - 10^{-3}$ Torr show an optimal range of high transmittance (~70%), low resistivity (~10^{-2} Ω cm), high carrier concentration of ~3×10^{19} cm^{-3} with mobility of ~5 cm^2/Vs, and large $E_g \geq 3.2$ eV.

The second section is focused on solar energy conversion applications of BFCO thin films based devices: (1) the photodiodes based on the epitaxial BFCO/$SrRuO_3$ (SRO) thin films were fabricated by using PLD techniques. The photodiodes with a large ideality factor (n≈5.0)

exhibits a substantial photocurrent at forward biased voltages (photoconductive effect) and a fast transient response (in the order of 10^{-2} s). The tailoring of photoelectric performance was achieved by switching FE polarization state of BFCO (E_g≈2.5 eV; P≈40 μC cm^{-2}). The ultrafast charge transfer at BFCO/SRO heterojunction was investigated by time-resolved photoluminescence. A peak sensitivity was measured as 0.38 mA/W at 500 nm by photoresponsivity spectroscopy. (2) We reported the fabrication of multiferroic BFCO thin films (E_g≈1.7−2.4 eV; P≈14−44 μC cm^{-2}) based PV devices with *p*-*i*-*n* heterojunction by PLD. A *p*-type NiO thin film acting as hole-transporting/electron-blocking layer and a typical *n*-type Nb-STO acting as electron-transporting layer were used to form the double-interfaced heterojunctions. Under 1 sun illumination, the optimized *p*-*i*-*n* devices yielded an open-circuit voltage of ~0.53 V and a short-circuit current density of ~8.0 mA cm^{-2}, leading to a PCE of ~2.0%, a four-fold enhancement compared to that of the *i*-*n* device architecture. (3) The *n*-type BFCO thin films coated with a *p*-type transparent conducting NiO layer were implemented as a heterojunction photoelectrode by PLD for solar-driven water splitting. The tailoring of PEC performance of the bare BFCO (E_g≈1.8 eV; P≈20 μC cm^{-2}) based photoanodes was achieved by effectively tuning the FE polarization state, and thus resulted in a 1.5-fold increase in photocurrent density. A 4-fold enhancement of photocurrent density, up to 0.4 mA cm^{-2} (at +1.23 V vs. RHE) in 1 M Na_2SO_4 (pH 6.8) electrolyte under 1 sun illumination was carried out by coating the bare BFCO photoanodes with a *p*-type transparent conducting NiO layer acting as an electron-blocking and protection layer. The stable operation of *p*-NiO/*n*-BFCO heterojunction photoanodes was confirmed by observing a constant current density over 4 hours.

Acknowledgements

During the period working on my Ph.D., I received tremendous help and encouragement from my colleagues, friends, and families, without whom the completion of this dissertation would never come true. I would like to express the deepest appreciation and send my gratitude from the bottom of my heart to those people, who helped me with their intelligence and patience along the working period.

First of all, I would like to thank my supervisor, Professor Federico Rosei, who kindly accepted me being his fellow as a graduate student. He guided me through the whole journey of study and research and provided me financial support. Under his supervision, I not only made a progress in academic field but also developed and polished my personality. Without Federico, I would not be able to accomplish my goal. I am very thankful to my co-supervisor, Dr. Riad Nechache, whom I closely worked with, both for fantastic ideas he generously gave to me, and valuable discussion we had through my entire work. Besides, he gave me a bunch of suggestion in term of study field I need to explore deeper and academic direction I need to work toward more. I always admire his insightful opinion. Even more, his industriousness makes him a role model as a scientist and I always get motivated from his hard-working spirit. I am also very thankful to my co-supervisor, Prof. Mohamed Chaker, whom I collaborated with for a large portion of my experiment work in field of pulsed laser deposition techniques.

Secondly, I would like to thank our group members and collaborators named below: Dr. Catalin Harnagea, Joyprokash Chakrabartty, Dr. Shun Li, Daniele Benetti, Xin Tong (with Prof. Rosei), Dr. Dawit Gedawu, Dr. Ibrahima Ka, Prof. Shuhui Sun and Xin Tong (with Prof. Sun).

I would like to thank those people for their help on the devices fabrication and characterizations, by which I could develop my study further.

Thirdly, I would like to show my appreciation to all the staff in LMN lab: Boris Le Drogoff, Etienne Charette, Amine Zitounie, Sébastien Delprat. I want to thank those people for working with me on the PLD setup, four-point probe station, ellipsometry spectroscopy, and UV laser lithography.

I would like to thank Prof. Dongling Ma and Prof. Aycan Yurtsever for early working on my doctoral examination. I would like to thank Dr. David Barba and Prof. Andreas Ruediger for the helpful work he did on photoluminescence measurements.

I would like to thank all staff in INRS-EMT, especially Mr. Christophe Chabanier, for working on the use of x-ray diffraction, x-ray photoelectron spectroscopy, and ultraviolet photoelectron spectroscopy.

I also would like to thank our Nano-Femto Lab (NFL) group members named below: Dr. Haiguang Zhao, Daling Cui, Lei Jin, Yufeng Zhou, etc. They always be with me and support me to get over the difficulties I confronted along the journey.

Finally moreover most importantly, I want to express my gratitude to my parents for their endless love and support during my entire Ph.D. study period.

List of Figures

Figure 13. (a) Different types of Fe and Cr octahedral stacking in BFCO along (001) and (111) cubic directions; (b) RSM scan around (111) reflection for (001)-oriented BFCO films. (c) Sketch of the double-perovskite crystal structure and corresponding pseudo-cubic unit cell of BFCO, showing (111) direction.[63]

Figure 14. Optical dielectric functions (a) and electric conductivity (b) as functions of photon energy, both real (solid) and imaginary (dotted) parts of double-perovskite BFCO.[28]

Figure 15. UV-visible absorption coefficient of 100 nm-thick BFCO films grown on STO substrates by PLD with various cationic ordering R and compared with $BiCrO_3$ and $BiFeO_3$ thin films.[64]

Figure 16. Long range B-site ordered double-perovskite structure of Bi_2FeCrO_6 with the arrangements of octahedral FeO_6 and CrO_6. Adapted from [63].

Figure 17. (a) $M(H)$ curves measurement of mutilferroic BFCO at 300 and 10 K temperature. (b) Current vs. applied voltage curve and the corresponding FE hysteresis loop obtained at RT for a 200 nm-thick BFCO film. The solid line corresponds to the polarization hysteresis loop after subtracting the leakage contribution. PFM images of multiferroic BFCO thin films: (c) as-grown and (d) after switching FE domains. (e) Corresponding FE hysteresis loops at nanoscale.[56, 71]

Figure 18. Efficiency−cost comparison of various solar energy conversion technologies.[72]

Figure 19. Current (I)-voltage (V) characteristic of a photodiode. The linear load lines represent the response of the external circuit: I = (Applied bias voltage − Diode voltage)/Total resistance. The points of intersection with the curves represent the actual current and voltage for a given bias, resistance and illumination.[74]

Figure 20. Schematic illustrations of (a) PN junction and (b) PIN junction photodiodes, showing the process of photocurrent generation.[75]

Figure 21. Schematic representation of a typical Si based p-n junction PV cell under light.[81]

Figure 22. NREL best research cell efficiencies.[87]

Figure 23. Schematic representation of dark (blue) and light (red) current voltage characteristics of a PV cell. The different quantities like open circuit voltage V_{oc} and short circuit current density J_{sc} are shown.[88]

Figure 24. (a) The Shockley-Queisser (S-Q) limit for the efficiency of a solar cell, without concentration of solar radiation. (b) Maximum V_{oc} in the S-Q model vs. bandgap of materials.[89, 90]

Figure 25. Simplified schematics for (a) the interfacial PV effect in a semiconductor *p*-*n* junction and (b) the BPV effect in a FE thin film. E: Electric field.[92]

Figure 26. (a) Schematics of the *I*−*V* curves measurements involved into the multiferroic BFO with geometry of electrodes for electric transport measurements perpendicular (DW⊥). (b) Corresponding *I*–*V* measurements yielding a V_{oc} of about 16 V.[93]

Figure 27. Principle of hydrogen production by water electrolysis using a semiconductor photoelectrode.[97]

Figure 28. Theoretical photocurrent densities for semiconductors under one-sun illumination. The blue curve is the integrated photon flux at different cutoff energies, based on the AM 1.5G solar spectrum. The green arrows at the bottom indicate the regions of ultraviolet (UV) (below 400 nm), visible (400−750 nm), and infrared (IR) spectra.[100]

Figure 29. Schematic of carrier generation, radiative and non-radiative recombination processes. The four electron–hole water splitting mechanism is illustrated on *n*- (*p*-) doped semiconductors with upward- (downward-) surface band bending in the two bottom panels.[94]

Figure 30. (a) Sketch of the multiferroic BFO based photodetector involved into a measurement circuit. (b) Corresponding photocurrent as a function of applied voltage.[80]

Figure 31. Photocurrent as a function of time under the illumination of weak visible light at an interval of 250 s. Schematic outlook of in-plane BFO based photodetector is given in the inset.[106]

Figure 32. (a) Layout of multiferroic BFO based PV device. (b) *J*-*V* measurements for ITO/BFO/SRO heterostructures reveal polarization (P) dependent changes in the PV properties of the device.[107]

Figure 33. (a) Layout of multiferroic Bi_2FeCrO_6 thin films based PV cells. (b) J_{sc}-*V* characteristics of devices (S1-S2) on basis of Bi_2FeCrO_6 with various bandgaps (1.5−2.2 eV) underwent different electric poling.[64]

Figure 34. *J-V* curves of Ag/$KBiFe_2O_5$/Ag device in the dark and under UV illumination at RT. Inset shows the measurement setup schematically.[108]

Figure 35. (a) Energy band diagrams for (001)-oriented BFO thin-film photoanodes in PEC water splitting cells in the no-polarization state. (b) Linear sweep voltammetry curves for BFO thin films in various thicknesses based photoanodes obtained in 0.5 M Na_2SO_4 (pH = 5.67) under light.[110]

Figure 36. (a) Diagram of a PEC cell showing the *p*-type BFCO thin film used as the photocathode designed for water reduction. (b) Variations of *J-V* (vs. Ag/AgCl) in 1 M Na_2SO_4 at pH 6.8 under chopped simulated 1 sun illumination and visible light illumination ($\lambda > 420$ nm) of BFCO thin film grown on $CrRuO_3/SrTiO_3$ substrate by PLD.[65]

Figure 37. Schematic of a typical Molecular Beam Epitaxy (MBE) chamber.[114]

Figure 38. Schematic illustration of the pulsed laser deposition (PLD) setup.[115]

Figure 39. Schematic illustration of the hybrid deposition setup combined PLD+MBE.[112]

Figure 40. Representative core level spectra of (a) Sr 3*d*, (b) In 3*d*, (c) Ti 2*p* and (d) O 1*s* from ISTO film ($x = 0.15$) using XPS.

Figure 41. (a) XRD profiles of the ISTO films ($x = 0$–0.15) grown on LAO (100) substrate; (b) XRD profiles of the ISTO films ($x = 0$–0.15) with 2θ between 40–50˚; (c) (e) (g) Φ-scan profiles around the (110) plane of ISTO films ($x = 0.01, 0.1, 0.15$); (d) (f) (h) Phi-scan profiles around the (110) plane of LAO (100) substrate.

Figure 42. (a) RSM profiles around (203) reflection of the ISTO film ($x = 0.1$) grown on LAO (100) substrate; (b) OP and IP lattice parameters vs. In concentration *x* for ISTO films ($x = 0$–0.15); (c) AFM images from the ISTO film ($x = 0.15$) and the root-mean-square roughness is measured to be ~0.57 nm over the area 5×5 μm^2.

Figure 43. (a) Resistivity, carrier concentration and mobility vs. In concentration *x* for the ISTO films ($x = 0.005$–0.15) at RT; (b) Resistivity vs. variant temperatures (-10 to 200˚C) for the ISTO film ($x = 0.01$) and (c) Current vs. voltage characteristic measured at RT for a junction composed of $SrIn_{0.15}Ti_{0.85}O_3$ // $SrNb_{0.05}Ti_{0.95}O_3$.

Figure 44. (a) Optical transmission spectra of ISTO films S1-S8 ($x = 0$–0.15) and single crystal STO. (b) Indirect optical transitions of ISTO films S1-S6 ($x = 0$–0.15) and single crystal STO.

(c) Indirect optical transitions of ISTO films S6-S8 (x = 0.15) grown under oxygen pressures ranging from 10^{-7} to 10^{-3} Torr.

Figure 45. (a) PL spectra for ISTO films (x = 0.05, 0.10, 0.15) measured at RT. (b) Energy band diagram of an ideal ISTO (x = 0.15)/NSTO *p-n* junction at thermal equilibrium.

Figure 46. (a) θ-2θ scan of a BFCO thin film grown on STO (001) substrate. (b) Φ-scan profiles around the (110) plane of BFCO thin film and STO (100) substrate. (c) RSM measurement of BFCO thin film on STO, around the (204) reflection of STO showing the spot related the disordered (d-) BFCO phase in film. (d) Optical absorbance spectrum of BFCO/STO. Inset shows corresponding direct optical transitions at visible range.

Figure 47. (a) Layout of ITO/BFCO/SRO heterostructures devices and the representation of FeO_6/CrO_6 arrangements of the double-perovskite BFCO crystal. (b) Variation in $J(E)$ device characteristics under illumination with intensity varying from 50 to 100 mW/cm^2. Inset shows the same curves as semi-log-plots.

Figure 48. (a) Sketch of the setup for PFM measurement. (b) AFM topography and PFM images after applied ±8 V pulses. (c) Local FE hysteresis loop for BFCO thin film. (d) Macro FE polarization measurement of devices at 2 kHz frequency at RT.

Figure 49. (a) J(E) curves for BFCO at virgin state and underwent ±15 V electric poling under illumination (100 mW/cm^2). (b) Schematic of simplified energy band alignments for heteroepitaxial structures for an ideal metal–semiconductor interface without polarization (top of panel: virgin state), and positively/negatively poled at ±15 V (middle and bottom of panel, respectively). (d) UPS valence band structure of BFCO.

Figure 50. (a) Reversible switching of electrical current at 0.3 V under illumination for photodiodes. (b) The rise (top of panel) and decay (bottom of panel) of the current in time for a single pulse in (a). (c) PL spectra of the heteroepitaxial structures under an excitation of 383 nm; Inset shows the schematic illustration of charge transfer at interfacial region of BFCO/SRO. (d) TRPL decay measured at 500 nm for the heteroepitaxial structures. Inset shows a magnified region of the TRPL spectra between 2–15 ns.

Figure 51. Photoresponsivity spectra of the device at 500 nm at zero bias. Inset shows a semi-log curve of measured spectrum.

Figure 52. (a) θ-2θ scan of BFCO films grown on NSTO (001) substrate; (b) (111) asymmetrical scan for BFCO #1 and #2. The BFCO (1/2 1/2 1/2) reflection demonstrating Fe/Cr cationic ordering in the films; (c)(d) RSM measurements of BFCO #1 and #2 films on NSTO, respectively, around the (204) reflection of NSTO showing the two spots related the coexistence of ordered (o-) and disordered (d-) BFCO phases in films.

Figure 53. (a) Schematics of the ordered domain in the disordered region of BFCO, and corresponding representation of FeO_6/CrO_6 arrangements in disordered and ordered domain of the double perovskite BFCO. (b) 2 × 2 μm^2 AFM image for 120 nm-thick BFCO #1 and (b) BFCO #2, the RMS roughness is ~6 nm.

Figure 54. 5 × 5 μm^2 PFM images after switching FE domains for: (a) BFCO #1 and (b) BFCO #2. Corresponding local FE hysteresis loops for (c) BFCO #1 and (d) BFCO #2; (e) FE properties of BFCO #1and BFCO #2 were measured at 2 kHz at RT.

Figure 55. (a) UV-visible absorption spectra of BFCO films; (b) Corresponding direct optical transitions; (c) Bandgap threshold (o-BFCO) and corresponding absorption area vs. R in BFCO films grown using different growth parameters.

Figure 56. High resolution XPS spectra of (a) Fe 2*p* (b) Cr 2*p* in BFCO #1; (c) Fe 2*p* and (d) Cr 2*p* in BFCO #2.

Figure 57. (a) PL spectra of *i*-*n* and *p*-*i*-*n* devices measured at RT; (b) UV-visible optical absorbance of NiO film; Inset: corresponding direct optical transition. High resolution XPS spectra of (c) Ni 2*p* and (d) O 1*s* in NiO.

Figure 58. *J*-*V* characteristics under AM 1.5G illumination for: (a) *i*-*n* devices and (c) *p*-*i*-*n* devices; Layout of the devices for: (b) *i*-*n* and (d) *p*-*i*-*n*, and showing one possible FE polarization controlled separation.

Figure 59. (a) Representative UPS measurements of NiO, BFCO #1, BFCO #4 and NSTO; (b) the detailed UPS valence band structure of films between 0 to 6 eV. Energy-level diagram based on UPS results showing the valence, Fermi and conduction energy of each component material included in: (c) device #1 (*i*-*n*), and (d) device #4 (*p*-*i*-*n*).

Figure 60. EQE measurements of device #1 (*i*-*n*) and device #4 (*p*-*i*-*n*).

Figure 61. (a) Plots of the real and imaginary components of the complex impedance of device #4 (*p*-*i*-*n*) and device #1 (*i*-*n*) heterojunction under a dark condition. The inset shows the details between 0 and 6000 Ω; (b) The trend of the real part of the capacitance (left axes) and the phase (right axes) as a function of the frequency obtained at short-circuit condition in dark.

Figure 62. (a) Double-perovskite structure of ordered BFCO crystals using ball-and-stick style. (b) θ-2θ scan for BFCO thin film epitaxially grown on (100) STO, buffered with SRO layer. (c) Asymmetric scan around (111) plane of (100) STO for BFCO. (d) 5×5 μm^2 AFM topography image for 90 nm-thick BFCO film grown on SRO/STO substrate.

Figure 63. (a) 3×3 μm^2 PFM image of BFCO on SRO/STO underwent ±8 V pulse switching FE domains, and (b) Corresponding FE hysteresis loop. Inset shows the setup of PFM. (c) FE polarization−electric field hysteresis loop measured on BFCO thin films at 2 kHz at RT; (d) Visible-light absorption spectra of BFCO thin films and corresponding direct optical transitions.

Figure 64. (a) Optical transmission and absorbance of NiO films grown on transparent STO substrate; Inset shows corresponding direct optical transition. (b) Conductivity−temperature measurements of NiO thin films. (c) XPS spectra of NiO thin films for: Ni 2*p* and O1*s*.

Figure 65. (a) Diagram of a BFCO based photoanode, showing one possible FE polarization direction. (b) Variations of the *J*-*V* curves of samples at virgin state, P_{up} and P_{down} in Na_2SO_4 under chopped light. Inset shows the open-circuit potential (V_{oc}) vs. time, and (c) Corresponding photoresponse before and after poling with two opposite directions under chopped light at +0.6 V (vs. RHE). (d) Mott–Schottky (M-S) measurements of samples at 0 V with frequency of 1 and 2 kHz.

Figure 66. Simplified energy band diagrams of a PEC cell based on an *n*-type BFCO thin film in electrolyte at pristine state (a), and either polarization down (b) or polarization up (c).

Figure 67. (a) A schematic diagram of the experimental setup used for the PEC measurements; and the proposed layout of NiO/BFCO/SRO heterojunction photoanode for water splitting shows that light is absorbed by BFCO thin films and the photogenerated holes transfer to the NiO, at which O_2 is produced; (b) *J*-*V* curves for the samples coated with 10 and 20 nm NiO layer under chopped light, respectively; Inset shows corresponding V_{oc} vs. time. (c) M-S

measurements of NiO/BFCO at 0 V with 1 and 2 kHz. (d) Band alignment and charge transfer at the interfacial regions of electrolyte/NiO/BFCO.

Figure 68. (a) Stability test of photoanodes with/without 10 nm thick-NiO layer at +0.9 V bias (vs. RHE) in 1 M Na_2SO_4 electrolyte under 1 sun illumination. The inset shows the SEM image to surface of NiO/BFCO photoanodes after stability tests of several hours. (b) IPCE spectra for BFCO-based photoanodes with/without 10 nm thick-NiO layer at 1.23 V (vs. RHE). The inset shows the corresponding ABPE as a function of applied potential.

List of Tables

Chapter 1. Introduction

1.1. Basics

1.1.1. Transparent conducting oxides

Transparent conductive oxides (TCOs) are multifunctional materials which simultaneously exhibit two contrasting properties, namely high metallic conductivity due to massive structural nonstoichiometry and nearly complete and insulator-like transparency in the visible range [1]. The unique properties of TCOs make them useful in many important technological applications such as flat-panel display, electrochromic window, optical communication, light-emitting diodes (LED), and photovoltaic (PV) devices, as shown in **Figure 1** [2]. The first TCO was a thin film of CdO prepared by thermally oxidizing a vacuum sputtered film of cadmium metal in 1907 [3]. While CdO is not widely used because of toxicity, it remains of theoretical interest because of its high electron mobility due to a low effective electron mass. The most important TCO used in practice is tin doped indium oxide (In_2O_3:Sn), also called indium-tin-oxide (ITO). ITO is used as a transparent electrode in all flat panel displays, due to its high optical transmission (>80% in visible range), electrical conductivity (~10^4 S cm^{-1}) and large optical band gap (E_g≈3.8 eV) [4].

To date, most of the commercial TCOs are *n*-type, which have larger electron concentrations than hole concentrations, such as ITO, Aluminium-doped ZnO (AZO), Fluoride-doped SnO_2 (FTO), etc. **Table 1** summarizes the typical *n*-type oxides thin films in the literatures [4-8]. However, in contrast to *n*-type TCOs, there are only a limited number of materials which show *p*-type conductivity and transparency at the same time. The scarcity of

p-type TCOs which have larger hole concentrations than electron concentrations is due to the strong localization on the upper edge of the valence band to oxide ions in electronic structure of oxides. Many works have been made to solve this problem by engineering electronic structures based on hybridization of O 2*p* orbitals with closed-shell Cu $3d^{10}$ orbitals. Recently, the Cu-based oxides have been investigated, such as delafossite materials $CuAlO_2$ [9]. **Table 2** summarizes the *p*-type oxides thin films in the recent literatures [9-13].

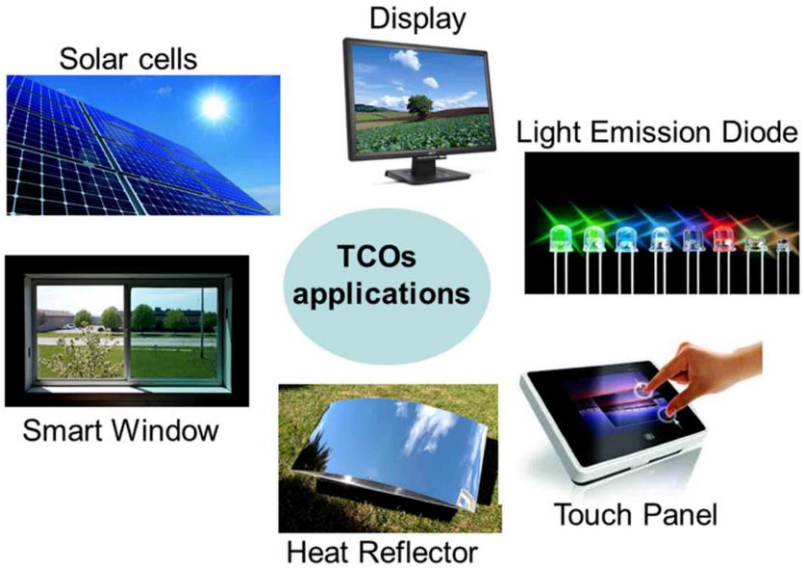

Figure 1. Various applications of transparent conducting oxides (TCOs). Adapted from [2].

Table 1. A brief summary *n*-type TCOs thin films in the literatures.

TCO thin films	Growth methods	E_{opt} (eV)	T (%) in vis.	ρ (Ω cm)	μ ($cm^2\ V^{-1}\ s^{-1}$)	n (cm^{-3})	Ref.
ITO	sputtering	3.8	80	10^{-4}	26-33	10^{21}	[4]
FTO	spray pyrolysis	3.4	80	10^{-4}	12-24	10^{20}	[5]
AZO	PLD	3.7	75-90	10^{-4}	16	10^{21}	[7]
Ga:ZnO	PLD	3.5	90	10^{-3}	31	10^{22}	[6]
La:$SrTiO_3$	PLD	3.3	80	10^{-3}	4	10^{20}	[8]

PLD: pulsed laser deposition; E_{opt}: optical band gap; T: optical transmittance; ρ: electrical resistivity; μ: carrier mobility; n: carrier concentration.

Table 2. A brief summary *p*-type TCOs thin films in the literatures.

TCO thin films	Growth methods	E_{opt} (eV)	T (%)	ρ (Ω cm)	μ ($cm^2 V^{-1} s^{-1}$)	n (cm^{-3})	Ref.
$CuAlO_2$	PLD	3.5	70	3	0.1	10^{19}	[9]
$CuGaO_2$	PLD	3.6	80	50	0.2	10^{18}	[12]
NiO	PLD	3.7	95	118	−	−	[13]
Li:NiO	sputtering	3.4	30	0.14	−	−	[11]
MoO_3	PLD	3.3	72	0.02	−	−	[10]

1.1.2. Epitaxial thin film

Thin film is coated onto a "substrate" surface to form layer whose material in thickness ranging from nanometers (nm) to micrometers (μm). The thin film deposition techniques including the physical and chemical deposition methods, are widely used in solar panels, disk drives, and optical devices [14]. Chemical deposition, i.e., chemical vapor deposition (CVD), is used to fabricate the high purity solid materials in a form of film, when a volatile fluid precursor produces a chemical change on a surface leaving a chemically deposited coating. Physical Deposition, i.e., physical vapor deposition (PVD) including thermal evaporation and sputtering, is the most common and useful physical technology where a material is released from a source and deposited on a substrate using electromechanical or thermodynamic processes [15].

Epitaxy is in regard to the growth of a crystalline thin film on the surface of a crystalline substrate whose crystal orientation imposes a crystalline order onto the thin film. Thus, the film can be grown up to a certain thickness (e.g., nanometers) in crystal structures differing from their bulks. The epitaxial growth of thin films is generally achieved by the film deposition techniques, including molecular beam epitaxy (MBE), CVD and pulsed laser deposition (PLD),

resulting in the lower density of defects in the films and the fabrication of films with different doping levels [16].

Moreover, understanding of the different mechanisms affecting the growth mode is necessary to control the surface morphology during thin film growth. Two independent processes: nucleation and growth of islands play an important role during vapor-phase epitaxial growth on an atomically flat surface. The thermodynamic approach to crystal growth is used to describe crystal growth close to equilibrium, that is, for a thermodynamically stable system. This thermodynamic approach has been used to determine growth modes of thin films close to equilibrium [17], that is, only at small or moderate supersaturation. Three different growth modes, schematically depicted in **Figures 2**(a) (b) (c) can be distinguished [18].

1) Island growth (Volmer-Weber)
   - form three dimensional islands;
   - film atoms more strongly bound to each other than to substrate;
   - and/or slow diffusion.
2) Layer by layer growth (Frank -van der Merwe)
   - generally highest crystalline quality;
   - film atoms more strongly bound to substrate than to each other;
   - and/or fast diffusion.
3) Mixed growth (Stranski-Krastanov)
   - initially layer by layer, and then forms three dimensional islands.

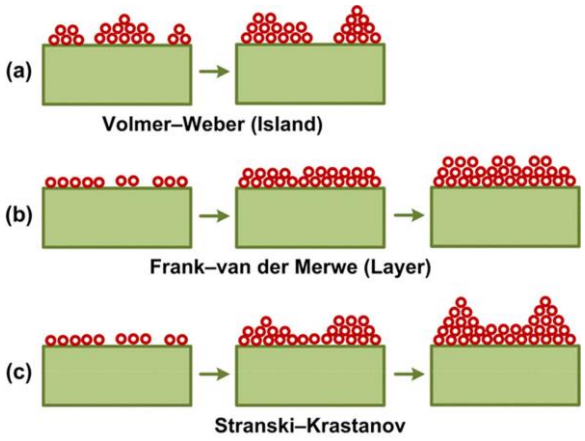

Figure 2. Three different growth mode: (a) Island growth; (b) Layer by layer growth; (c) Mixed growth.[18]

1.1.3. Perovskite oxides

Perovskite is a type of crystal structure in the family of transition metal (TM) oxides, in addition to the spinel, scheelite and pyrochlore. Perovskite oxides show the remarkably versatile chemical and physical properties due to the unique nature of TM's outer *d* orbital electrons. This gives cations with several oxidation states and the metal-oxygen bonding varying from nearly ionic to metallic. Perovskite oxides are used in electronics and telecommunication because of their prominent superconductivity, magnetoresistance, dielectric properties and ferroelectricity [19]. There are many different types of distortions in perovskites, including the tilting of the octahedra, distortions of the octahedra driven by electronic factors (i.e., Jahn-Teller distortions [20]), etc. This could reduce the symmetry of crystal structure, thus influences some physical properties such as the electronic, magnetic and dielectric properties.

Schematic diagram of the typical perovskites structure is shown in **Figure 3** [21]. The structure of perovskite is a primitive cubic structure of the general stoichiometry ABO_3 (space group *Pm*3-*m*), containing two kinds of cations and one kind of oxygen anion. One of the cation

sublattices is built-up by "*A*" cations with a coordination number of 12, surrounded by 8 corner-sharing BO_6 octahedra.

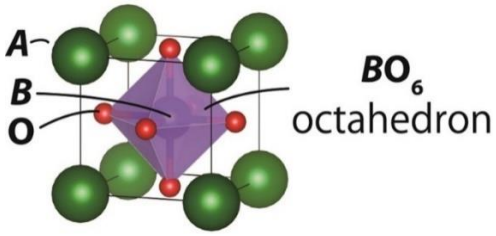

Figure 3. Schematic illustration of ideal perovskite structure ABO_3 [21].

The tailoring of the physical properties for perovskites from their parent compounds by substitutions could be achieved by the distortion of structures due to the *A* and/or *B* non-isovalent substitutions. Taking the typical cubic perovskite $BiFeO_3$ as example [22], the divalent (+2), trivalent (+3) or tetravalent (+4) cations (e.g., Sr, Cr, Pb, respectively) substitution or doping for *A* and *B*-sublattice have been extensively studied to optimize its FE and ferromagnetic properties [23]. The cations may be either randomly distributed or adopt an ordered configuration as the multiple cations substitution into either the *A* or *B*-sites, where the ordering of the cations strongly depends on the differences of their charges and sizes.

Double perovskites evolved from their primitive unit of perovskite ABO_3 (or $A_2B_2O_6$) can be represented by the general formula $AA'B_2O_6$ (1:1 *A*-site ordering) and $A_2BB'O_6$ (1:1 *B*-site ordering), exampling $CaFeTi_2O_6$ (**Figure 4**(a)) [24] and La_2NiMnO_6 (**Figure 4**(b)) [25], La_2BMnO_6 [26], La_2FeMnO_6 [27], Bi_2FeCrO_6 [28], respectively. Additionally, the $AA'BB'O_6$ also represents the double perovskite structure with both *A*- and *B*-site ordering, such as $NaLaMgWO_6$ (**Figure 4**(c)) [29].

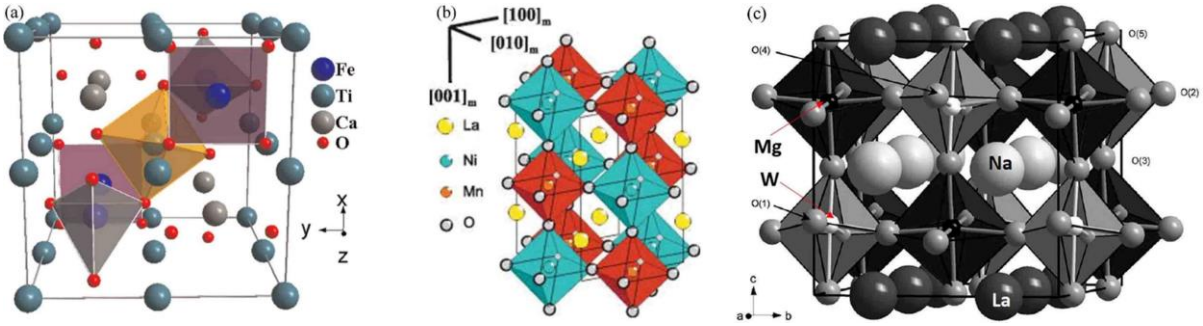

Figure 4. Crystal structure of (a) *A*-site ordered double perovskite $CaFeTi_2O_6$; (b) *B*-site ordered double perovskite La_2NiMnO_6 and (c) both *A*- and *B*-site ordered double perovskite $NaLaMgWO_6$.[24, 25, 29]

Among these types of double perovskites, the modified $A_2BB'O_6$ structure (see **Figure 5)** with *B*-site aliovalent substitutions and the BO_6 and $B'O_6$ octahedra which are alternatively arranged in two interleaving face-center-cubic (FCC) sublattices [30]. The *A* sites are usually occupied by alkaline ions, while the *B* sites correspond to TM ions. Double perovskites $A_2BB'O_6$ materials are the promising candidates for electronic devices owing to their physical characteristics (e.g., magnetic properties) resulting from the strong super-exchange couplings between various combinations of 3*d*, 4*d* and 5*d* elements [31].

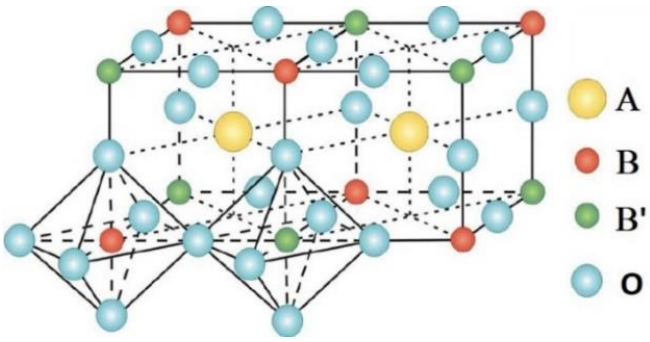

Figure 5. Representative crystal structure of double perovskite $A_2BB'O_6$ showing BO_6 and $B'O_6$ octahedra.[30]

1.1.4. Ferroelectricity

In dielectric materials, the presence of an external electric field (E_{ext}) induces an internal electric field (E_{int}) due to the free charges, electric dipoles or atomic polarizability which tend to screen the applied E_{ext}. Under certain conditions, electric dipoles of the material can be aligned in the same direction and give rise to a spontaneous polarization. This phenomenon discovered in 1920 is called ferroelectricity [32]. FE materials are characterized by a transition temperature, the Curie temperature T_C between paraelectric and FE phases. Ferroelectrics are a class of materials with a permanent polar axis, and the polarization direction can be switched by applying an E_{ext}. At temperatures above T_C, the crystals are non-polar and no longer FE and behave like normal dielectrics, as known as paraelectrics. One of the best known examples is $BaTiO_3$ (**Figure 6**) [33]. They are widely used for designing sensors, tunable capacitors, as well as FE random access memories in which the information is stored by the remnant polarization [34].

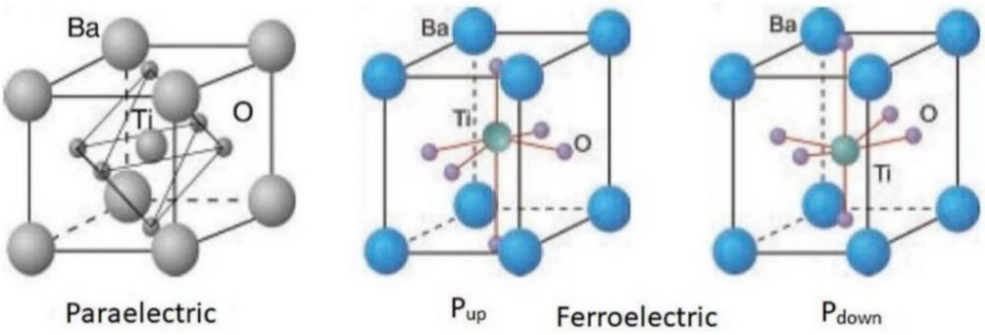

Figure 6. Atomic structures of perovskite $BaTiO_3$ in (a) the paraelectric cubic phase at high temperature and FE phase with upward (b) and downward (c) polarization at RT.[33]

In ABO_3 perovskites, a central positive *B*-ion is surrounded by an octahedron of oxygen ions with negative charges (O^{2-}), whose position shifting during structural phase transitions (e.g., cubic to tetragonal) would break the inversion symmetry and induces the dipole moment, thus demonstrating the FE order. For example, the $BaTiO_3$ with paraelectric cubic phase at high temperature transfers to $BaTiO_3$ with FE phase at RT (**Figure 6)** [34]. In the most of FE perovskites, the *B*-site atom has an empty *d* electron shell allowing covalent bonding with the full *p* orbitals of the O atoms. Ferroelectricity can also occur due to the existence of lone pairs of electrons on the outer shell of the *A*-site atom, which are highly susceptible to polarization [35].

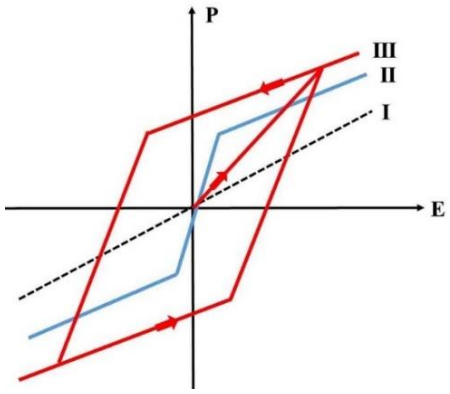

Figure 7. Polarization (*P*) − Electric field (*E*) characteristics for different polarization types: I: Dielectric polarization; II: Paraelectric polarization; III: FE polarization. Inspired from [36].

Some materials are polarized by an E_{ext} and show a linear relationship between polarization and electric field (*P*-*E*), as known as dielectric polarization (**Figure 7, I**). Some paraelectric materials demonstrate a more pronounced nonlinear polarization (**Figure 7, II**) [36]. The electric permittivity is a function of the E_{ext}, corresponding to the slope of the polarization curve. Additionally, FE materials show a spontaneous (zero field) polarization

(**Figure 7, III**). The direction of the spontaneous polarization can be reversed by an applied E_{ext}, and demonstrating a hysteresis loop.

1.1.5. Magnetism

The filling of the atomic orbitals with electrons is given by Hund's rules [37], and results from the competition between the Pauli Exclusion principle [38] and the Coulomb repulsion [39]. As the Pauli Exclusion prevents two spins to occupy the same quantum state simultaneously, two parallel spins have to occupy in different orbitals whereas two anti-parallel spins can occupy in the same orbital. Therefore two parallel spins save some Coulomb energy compared to two anti-parallel spins. A mechanism able to induce magnetic moments on atoms with partially filled external orbitals. The exchange interaction between magnetic species in a solid [40] leads to a magnetic order which depends of the system symmetry: (1) For positive exchange interaction, magnetic ordering leads to a net magnetic moment at zero field, called ferromagnetism. (2) For negative exchange interaction, magnetic ordering leads to a zero net magnetic moment, called antiferromagnetism. These energy terms are in competition with thermal agitation and above a T_C for ferromagnetism and Néel temperature (T_N) for antiferromagnetism, the magnetic order disappears in a paramagnetic phase [41].

The magnetic material displays the attractive or repulsive forces with another piece of the same material, which is widely used for recording and storing data devices [42]. Magnetic properties owing to the presence of unpaired electrons are mainly exhibited by materials containing TMs, which induced by their partially filled *d* orbitals. When the magnetic moments are oriented randomly, it is called a paramagnet, and the moments can be aligned by the applied external magnetic field (M_{ext}).

The main types of magnetic behaviors including paramagnetic, ferromagnetic and antiferromagntic are schematically illustrated in **Figure 8 (a)-(e)**.

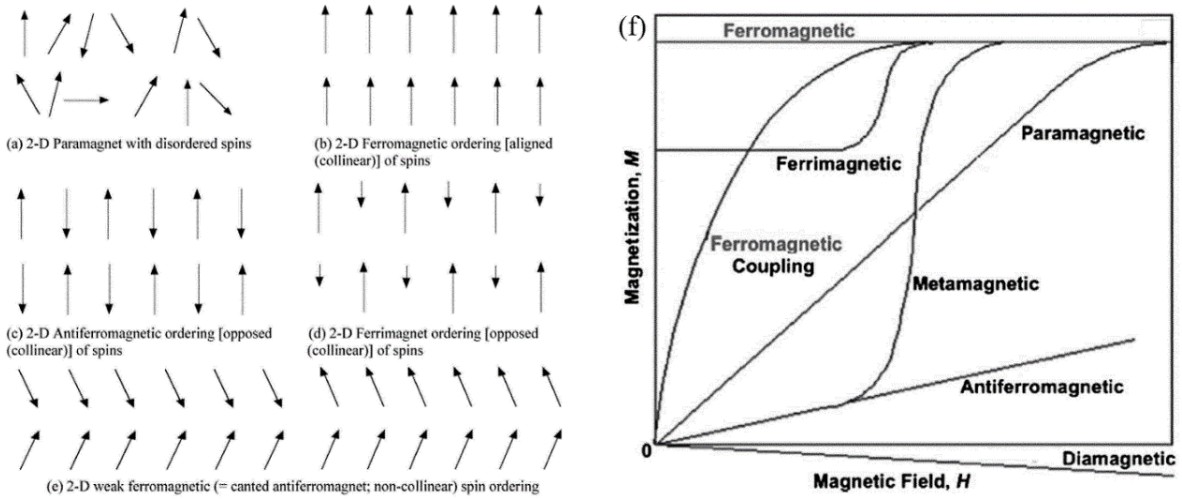

Figure 8. Schematic illustrations of spin interactions for several 2-D magnetic behaviors in 3-D magnetic phenomena: (a) 2-D paramagnetic disordered spins, (b) 2-D ferromagnetic ordered spins, (c) 2-D antiferromagnetic ordered spins, (d) 2-D ferrimagnetic ordered spins, and (e) 2-D weak ferromagnetic ordered spins. (f) Variation of M(H) for corresponding types of magnetic interactions.[43]

Figure 8(a) shows a paramagnetic behavior in ferromagnetic materials without any spins interaction. The spin coupling enables to demonstrate the parallel or antiparallel interactions for ferromagnetic or antiferromagnetic coupling, respectively (**Figure 8**(b)(c)). Ferrimagnet with an inverse spinel structure is caused by the antiferromagnetic coupling, and a net magnetic moment is induced, as shown in **Figure 8**(d). **Figure 8**(e) shows the magnetic ordering termed weak ferromagnet or equivalently canted antiferromagnet, which produced by the incomplete cancellation of magnetic moments in the systems where all spins are equivalent. The ferro-, antiferro-, ferrimagnetic, and weak ferromagnetic ordering occur below a critical

or magnetic ordering temperature, T_C. **Figure 8**(f) shows the magnetization−magnetic field (M(H)) variations for the corresponding types of magnetic interactions [43]. The magnetization, M (= χH), where H is the applied magnetic field and χ is susceptibility. M(H) increases with increasing H prior to reaching a maximum value (the saturation magnetization). Ferro- or ferrimagnets exhibit a spontaneous magnetization, although with different saturation magnetization values.

1.1.6. Multiferroic materials

In 19th century, Maxwell equations first combined the electronic and magnetic properties. The electric and magnetic ordering in solids are most often considered separately due to the charge effects of electrons and ions, whereas electron spins govern magnetic properties. For example, in spintronics [44], the effects of spins on the transport properties of solids allow the possibility to control one by the other.

In the recent few decades, multiferroic materials showing more than one type of ferroic order in one phase simultaneously (e.g., ferromagnetism, ferroelectricity or ferroelasticity) have been extensively studied for understanding the interaction between magnetic and electric coupling, and potential multifunctional applications [45-47]. Morever, the coupling between magnetic and electric properties, called magnetoelectric effect, induces the possibility of tuning electrical polarization and magnetization by applying an M_{ext} and E_{ext}, respectively [48, 49], as shown in **Figure 9**.

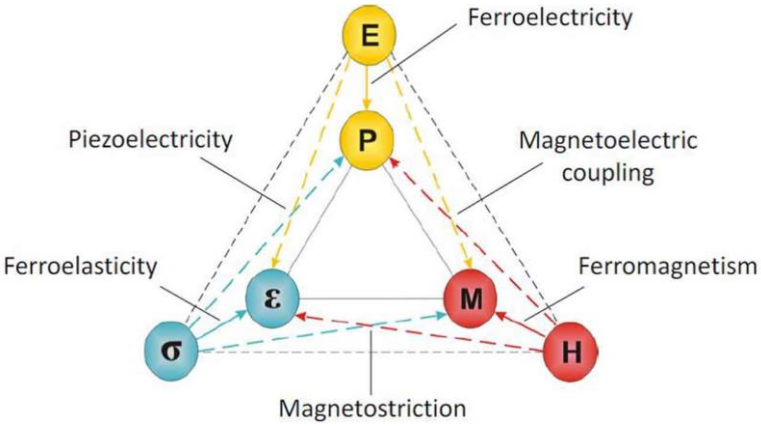

Figure 9. Summary of all the functionalities of multiferroic materials. *E* and *P* represent electric field and polarization, *H* and *M* represent magnetic field and magnetization, and σ and ε are stress and deformation, respectively.[30]

Generally, most of studied typical multiferroics are perovskite TM oxides like $TbMnO_3$, $HoMn_2O_5$ and bismuth compounds like $BiFeO_3$, $BiMnO_3$, as shown in **Figure 10**. The single-phase multiferroics comprise two types according the originality of ferroelectricity, including Type I: proper multiferroics and Type II: improper multiferroics.

Type I multiferroics have been known for a long time, which are good ferroelectrics and antiferromagnetic with high FE and lower magnetic ordering temperatures. The most typical materials are $BiFeO_3$ (T_C = 1100 K, T_N = 643 K) [50], $YMnO_3$ (T_C = 914 K, T_N = 76 K) [51], $BiMnO_3$ and $PbVO_3$ (**Figure 10**). The magnetoelectric coupling between the FE and magnetic ordering is usually weak due to the each other's independent properties.

Type II multiferroics include rare-earth manganites such as $TbMnO_3$, $HoMn_2O_5$ (**Figure 10)** with low ferroelectricity and ordering temperatures (e.g., 28 K for $TbMnO_3$ [52]), low net magnetization due to antiferromagnetic spin-spiral structures and low polarization in

the order of 10^{-2} μC cm^{-2} [53]. Other, non-perovskite multiferroic oxides, such as $LuFe_2O_4$ and $LiCu_2O_2$ and non-oxide multiferroics such as $BaNiF_4$ and $ZnCr_2Se_4$.

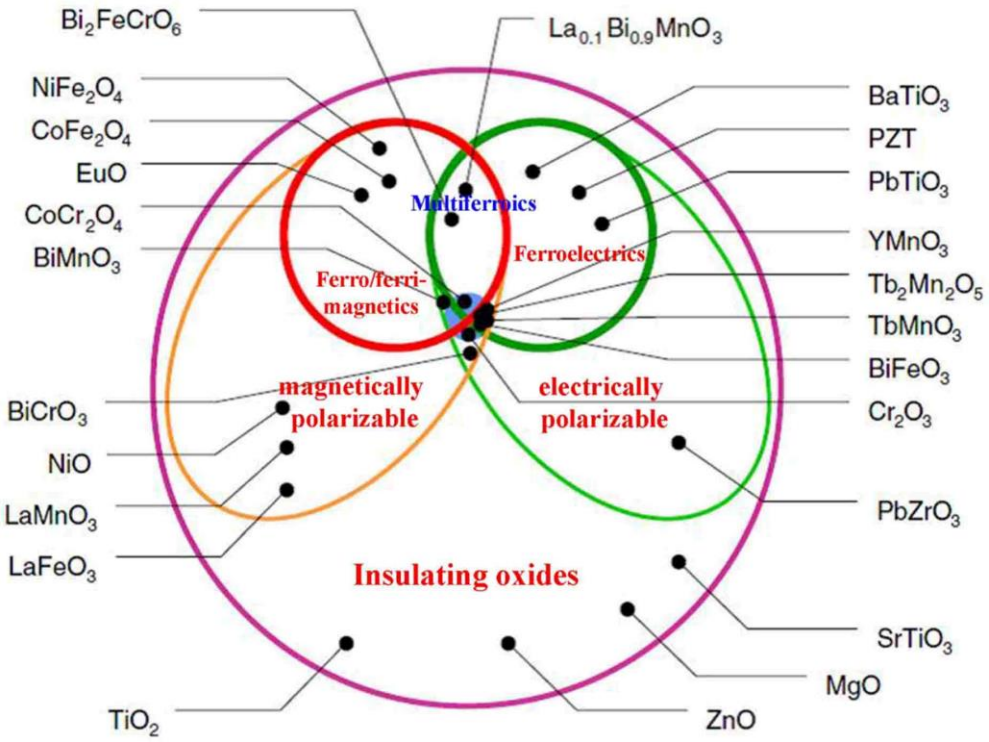

Figure 10. Classification of insulating oxides including FE, ferromagnetic and multiferroic materials and corresponding representative materials. [54]

1.2. Multiferroic Bi_2FeCrO_6

1.2.1. Synthesis method

Bi_2FeCrO_6 (BFCO) is expected to take in a simple perovskite structure with random occupancy of Fe^{3+} and Cr^{3+} on the *B* site, since the long range *B*-site ordered double-perovskite compound is not likely to form due to the same valence state and near ionic radii (r_{Fe}^{3+} = 0.645 Å and r_{Cr}^{3+} = 0.615 Å) of Fe^{3+} and Cr^{3+}. Whereas some experimental results demonstrated that the ceramic $Bi(Fe,Cr)O_3$ epitaxial thin films are isostructural to rhombohedral double-perovskite $BiFeO_3$,

showing a large FE polarization of ~55 μC cm^{-2} and a small magnetization at RT due to the lack of Fe/Cr cation ordering along the (111) cubic direction in the samples. Nechache *et al.*[55] firstly reported the growth of epitaxial BFCO multiferroic thin films on adequate substrates under controlled conditions using a physical synthesis method, that is pulsed laser deposition (PLD), and characterizations of the remarkable FE and ferrimagnetic properties.

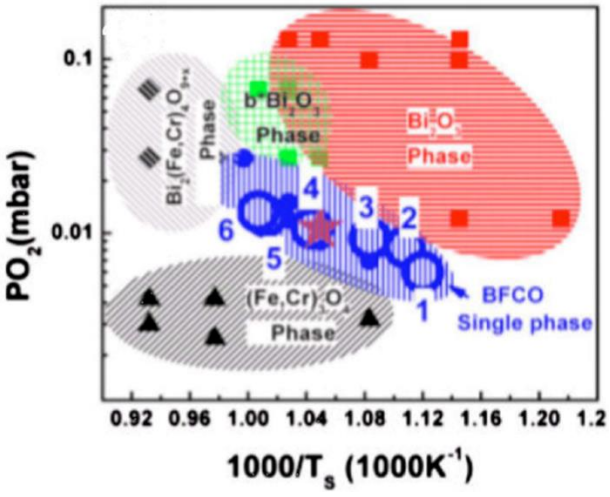

Figure 11. Pressure of oxygen (P_{O2}) − temperature of substrate (T_s) phase diagram for thin films of the Bi–Fe–Cr–O system grown by PLD.[56]

Pulsed Laser Deposition (PLD) is one of the most useful and simple synthesis method to grow complex oxides, like $LaBiFeCrO_6$ [57], BFCO, La_2FeCrO_6 [58] under controlled optimal conditions including laser fluence, substrate temperature, oxygen/gas partial pressure, etc. Thus, multiferroic BFCO thin film is fabricated by PLD techniques, generally grown on the crystalline substrates like $SrTiO_3$ (STO), $LaAlO_3$, $(LaAlO_3)_{0.3}(Sr_2AlTaO_6)_{0.7}$ (LSAT), MgO and metal-oxides coated Si wafer (e.g., Nb-STO/MgO/Si wafer [59]). Nechache *et al.*[55] reported that a single crystal (001)-oriented BFCO phase is obtained at a substrate temperature (T_S) of 680 °C and oxygen pressure (P_{O2}) of 8 mTorr. The deviation from this oxygen pressure

during the BFCO growth results in the appearance of secondary phases, such as the Bi_2O_3 (BO) at relatively high T_S and P_{O2}; and $(FeCr)_3O_4$ (FCO) at lower T_S and P_{O2}. This dependence on T_S and P_{O2} is due to the presence of highly volatile bismuth in the film which is sensitive to the deposition parameters. Several elements point toward a relationship between nonstoichiometry (i.e., oxygen vacancies and cation deficiency) and the destabilization of the BFCO single phase. The various phase formation under different growth conditions is graphically summarized in the phase diagram presented in **Figure 11**.

1.2.2. Crystal structure and cationic ordering

The lowest energy and stable structure of double perovskite BFCO has R3 symmetry (space group # 146, rhombohedral) which is different from the cubic double perovskite due to the alternating rotations of oxygen octahedra around Fe/Cr cations. The magnetic order becomes ferrimagnetic while every Cr spin orienting upward and Fe spin downward. The experimental lattice constant a = 5.537 Å and c = 13.502 Å (α = 60.20°) are intermediate values of existing experimental results [55, 60-62]. After internal structure optimization, every atom has a displacement from that of the cubic perovskite structure.

Table 3. Optimized internal structural parameters of BFCO with the Rc crystal structure [28].

Atom	Parameter	Values
Bi	Z_1	0.0005, 0.5040
Fe/Cr	Z_2	0.7330 / 0.2260
	x	0.5433, 0.0511
O	y	0.9542, 0.9043
	z	0.3937, 0.4459

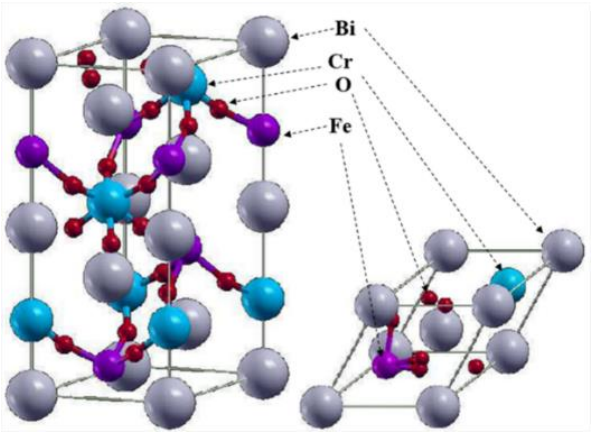

Figure 12. Crystal structure of double perovskite Bi_2FeCrO_6. The left-side is used to describe the relative positions of the atoms, and the right-side is the primitive cell.[28]

The crystal structure and primitive cell are illustrated in **Figure 12**. The optimized parameters are summarized in **Table 3**. The bond lengths and Fe-O-Cr bond angle can be calculated from the structural parameters. The calculated values are summarized in **Table 4**.

Table 4. Bond lengths (Å) and Fe-O-Cr angle (°) of BFCO with the Rc crystal structure [28].

Bond length	Fe-O	2.130, 1.971
	Cr-O	1.947, 1.994
	Bi-O	2.347, 2.387
		2.406, 2.416
Bond angle	Fe-O-Cr	153.7, 153.6

Furthermore, Nechache *et al.*[56] pointed out that the Fe/Cr cation ordering in epitaxial BFCO single phase plays a crucial role in establishing the good FE and ferromagnetic properties. They have demonstrated the presence of the Fe/Cr cation ordering and quantified it in the BFCO single phase through some experimental approaches. The alternation of octahedral FeO_6 and CrO_6 is achieved only in the (111) cubic direction of BFCO phase from different types of stacking in **Figure 13**(a). The superstructure reflections (00*l*), where *l* is 1, 2, 3, are

visible in the (001)-oriented BFCO thin films grown on single-crystal (100)-oriented STO substrates by PLD, not shown here. The reciprocal space mapping (RSM) of X-ray diffraction (XRD) around the (111) cubic reflection of STO was performed to determine the Fe/Cr cationic ordering. The RSM diagram in **Figure 13**(b) reveals the existence of two extra spots (1/2 1/2 1/2 and 3/2 3/2 3/2) in addition to the (111) main reflection of STO and BFCO. The periodicity of the superstructure reflections is about 4.58 Å, which is double the (111) perovskite cubic distance BFCO $d_{½½½}/2 \approx$ STO d_{111} (2.28 Å).

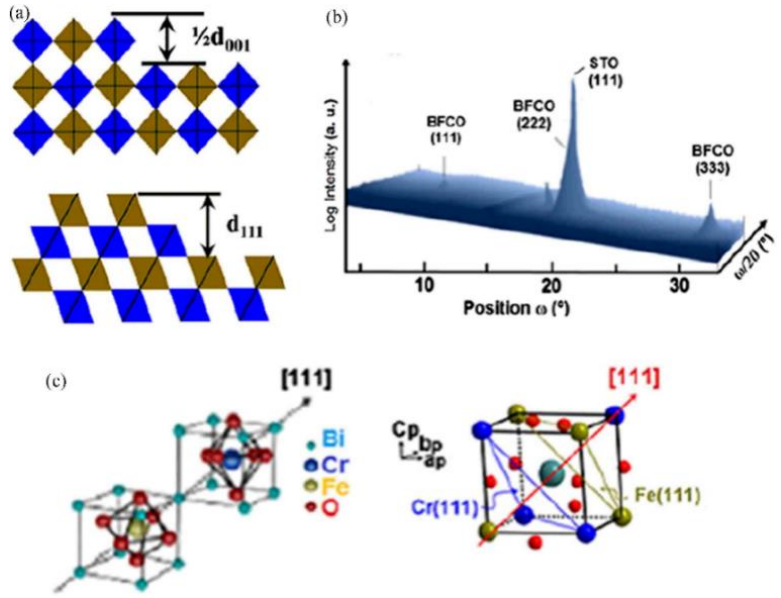

Figure 13. (a) Different types of Fe and Cr octahedral stacking in BFCO along (001) and (111) cubic directions; (b) RSM scan around (111) reflection for (001)-oriented BFCO films. (c) Sketch of the double-perovskite crystal structure and corresponding pseudo-cubic unit cell of BFCO, showing (111) direction.[63]

This doubling of the perovskite unit cell suggest the existence of the Fe/Cr ordering in the films along the (111) crystal structure (**Figure 13**(c)). A detailed analysis of the normalized intensity of the superstructure peaks was carried out to quantify the degree of Fe/Cr cationic

ordering, which was estimated from the normalized ratio of the superlattice peak intensity to the main (111) reflection intensity of BFCO. Thus, degree of cationic ordering, R = I_{222}/I_{111} × 100%.

1.2.3. Optical properties

Optical properties of BFCO relative to the optical dielectric function, optical conductivity and optical absorption are expected to further study in theoretical and experimental research. Song *et al.*[28] reported a study on electronic and optical properties of BFCO from first principle investigation using the combination of a full-potential density-functional-theory (DFT) method with Monte Carlo simulation. They calculated the direct electronic contributions of the optical dielectric function ε(ω) and optical conductivity σ(ω) curves of the BFCO as functions of photon energy (ω). Considering that the semiconductor gaps have important impact on the low-energy parts of these optical functions, they calculated them with both Generalized Gradient Approximation (GGA) and modified Becke-Johnson exchange potential (mBJ). These results, both real (Re) and imaginary parts (Im) between 0 and 12 (or 13) eV, are presented in **Figure 14**.

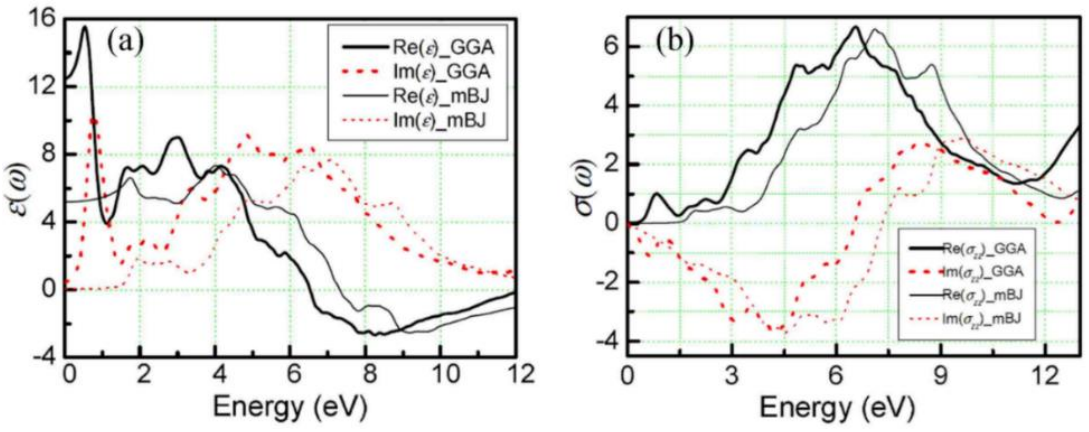

Figure 14. Optical dielectric functions (a) and electric conductivity (b) as functions of photon energy, both real (solid) and imaginary (dotted) parts of double-perovskite BFCO.[28]

For Re(ε), the GGA result of the low energy limit is higher than the mBJ one, having the similar trend at the energy ≥1.5 eV. For Im(ε), the main difference appears at low energy (<1.5 eV). There is a sharp peak at 0.75 eV for the GGA result, which is related to the steep decrease in the GGA curve of Re(ε) at the same photon energy. The mBJ result of Im(ε) is equivalent to zero in this region, which indicates the broad semiconductor gap from mBJ. For the σ(ω) curves, the main difference also appears at the low energy region. Re(σ(ω)) has a peak at 1.0 eV and Im(σ(ω)) has a valley at 0.5 eV. For the higher energy, both of the σ(ω) curves have similar behaviors [28]. These calculated optical functions could be useful in exploring the optical properties of double-perovskite BFCO and others similar materials.

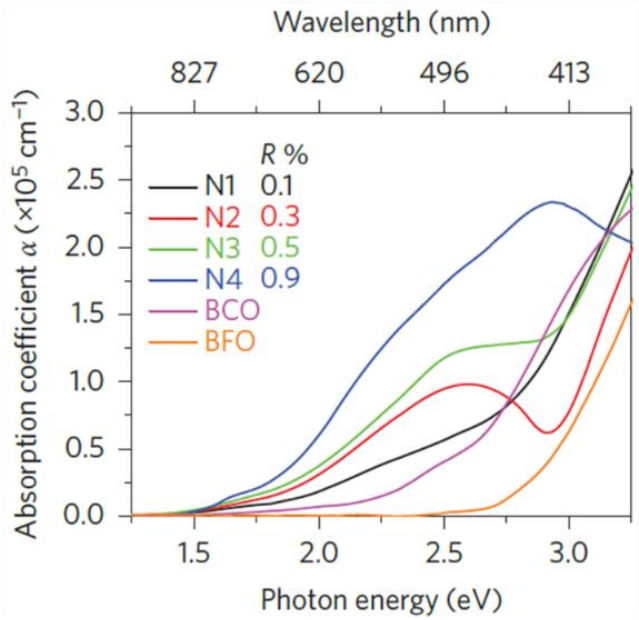

Figure 15. UV-visible absorption coefficient of 100 nm-thick BFCO films grown on STO substrates by PLD with various cationic ordering R and compared with $BiCrO_3$ (BCO) and $BiFeO_3$ (BFO) thin films.[64]

Additionally, the optical absorption coefficient is also a crucial important parameter for the double-perovskite multiferroic BFCO as a functional layer in solar energy conversion application. Nechache *et al.*[64] devoted to experimentally study the effect of Fe/Cr cationic ordering (the ratio of degree of Fe/Cr cationic ordering: R) in BFCO single phase on optical absorption properties. **Figure 15** shows that the higher value of R, the higher absorption coefficient α (up to ~2.3×10^5 cm^{-1}). Morever, the values of α for BFCO with various R are much more significant than both $BiCrO_3$ (absence of Fe^{3+}) and $BiFeO_3$ (absence of Cr^{3+}) thin films at visible range due to the modification of TM–oxygen bond lengths and their interaction energies including the hybridization energy and Coulomb repulsion caused by the absence of either Fe^{3+} or Cr^{3+} in perovskite structure (typical perovskite formula: ABO_3) [65].

1.2.4. Multiferroic properties

The B-site ordered double-perovskites oxides with general formula $A_2BB'O_6$ are two different 3*d* TM ions (*B* and *B*') inducing an intrinsic strong ferromagnetic interaction. According to the Kanamori-Goodenough rules [66, 67], ferromagnetism appears when one TM ion with e_g electrons (*B*) and another without e_g electrons (*B*') are ordered (*B*-O-*B*') at the *B*-sites of the perovskite structure. In the ferroelectricity-magnetism coexisted single phase, the atoms move off the center to induce electric dipole moment (i.e., FE polarization), different from the magnetic moment (i.e., magnetization).

Recently, the multiferroic and *B*-site ordered (*B*-O-*B*') double-perovskite BFCO has been extensively investigated. In the predicted BFCO material by first-principles calculations [28], the ferroelectricity is due to the $6s^2$ lone pair on Bi^{3+} ions, a well-established mechanism in other multiferroics, such as $BiMnO_3$ [68] and $BiFeO_3$ [69], while magnetism is introduced *via*

ferrimagnetic behaviour. The coupling between neighboring Cr and Fe magnetic moments is robustly antiferromagnetic and the difference between their magnetizations yields a net magnetization for BFCO. According to the works, the hypothetical double perovskites BFCO, where Fe^{3+}/Cr^{3+} should be long-range-ordered (**Figure 16**), would have a magnetic moment of ~2 μ_B per formula unit (~160 emu cm^{-3}) at 110 K [70] resulting from the antiferromagnetic exchange interaction between 5*d* Fe^{3+} and 3*d* Cr^{3+} in opposite directions and a FE polarization of ~80 μC cm^{-2}.

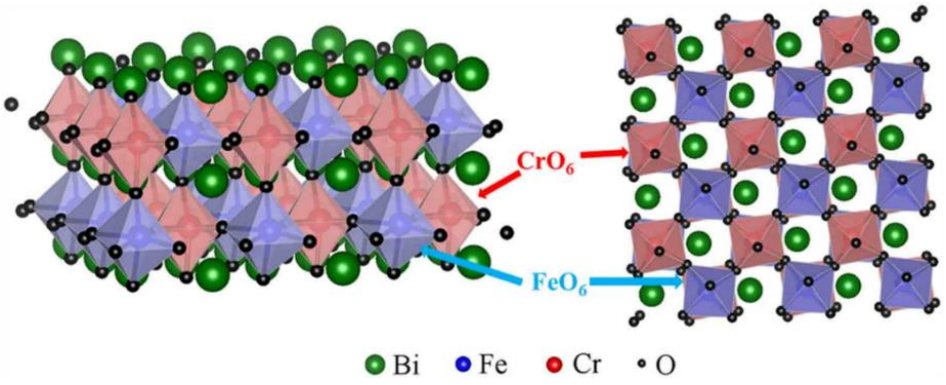

Figure 16. Long range B-site ordered double-perovskite structure of Bi_2FeCrO_6 with the arrangements of octahedral FeO_6 and CrO_6. Adapted from [63].

Nechache *et al.*[63] reported that *B*-site ordered double-perovskite BFCO single phase showed a large magnetization and FE polarization. Magnetic properties of BFCO thin films are shown in **Figure 17**(a) demonstrating a saturated magnetic moment of ~2×10^{-4} emu (electromagnetic units) measured at applied magnetic field of 5 kOe, at both 300 and 10K [56]. Additionally, the measurements of *M*(*H*) curves using SQUID magnetometer with an applied magnetic field of 10 kOe at both 300 and 10K were carried out and showed the saturation magnetization of ~145 emu per cubic centimeters (emu/cc), which corresponds to ~0.96 Bohr

magneton (μ_B) per cation site or ~1.91μ_B per Fe–Cr pair (i.e., ~1.91μ_B per BFCO formula unit) [56].

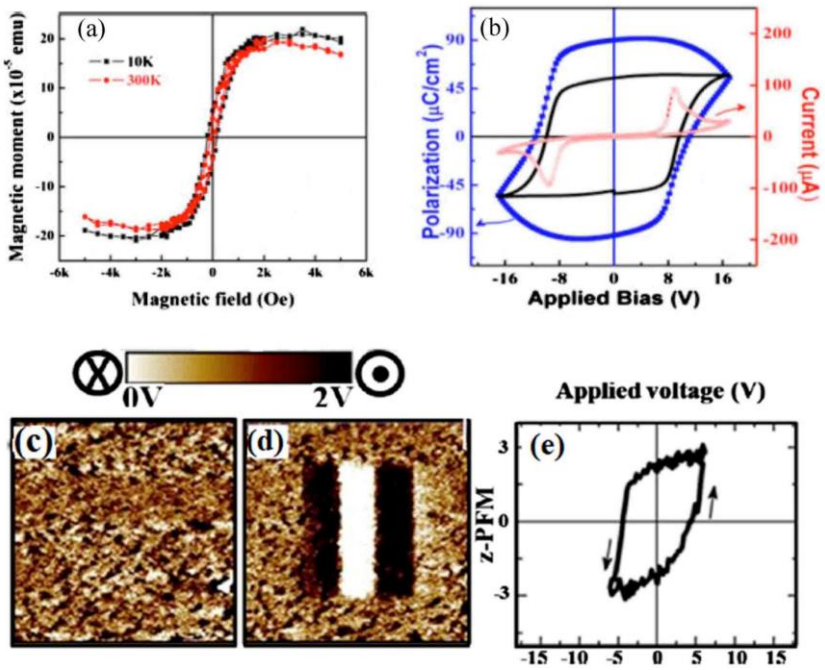

Figure 17. (a) *M*(*H*) curves measurement of mutilferroic BFCO at 300 and 10 K temperature. (b) Current vs. applied voltage curve and the corresponding FE hysteresis loop obtained at RT for a 200 nm-thick BFCO film. The solid line corresponds to the polarization hysteresis loop after subtracting the leakage contribution. PFM images of multiferroic BFCO thin films: (c) as-grown and (d) after switching FE domains. (e) Corresponding FE hysteresis loops at nanoscale.[56, 71]

The polarization effect could also govern the ferromagnetic super-exchange interaction. The large anisotropic overlap of the Bi 6s^2 lone pair electrons and the surrounding hybridized Fe 3*d*-O 2*p* orbitals induced built-in electric field can facilitate their coupling to the long-range spin order by minimizing the magneto-elastic energy [56]. Thus, this could not only allow the direct coupling between the magnetization and polarization but also strongly enhance the

ferromagnetic super-exchange interactions, leading to a magnetic T_C close to the FE transition. Recent infrared and magnetic characterization of 200 nm-thick BFCO film seems to confirm this fact [56]. FE properties of 200 nm-thick films deposited under optimum conditions are shown in **Figure 17**(b). BFCO films show FE property with a remnant polarization of 55–60 $\mu C\ cm^{-2}$ along the (001) direction (after subtracting the leakage current contribution). To further understand the FE properties of BFCO at nanoscale, **Figure 17**(d) demonstrate the FE polarization imprint was switched during scanning, by applying either negative or positive voltages between the conducting tip and the electrode or conducting substrate, compared with the as-grown BFCO as shown in **Figure 17**(c). Further analysis of the FE character of BFCO films was performed by local remnant piezoelectric hysteresis loops, as shown in **Figure 17**(e).

1.3. Multiferroic materials for solar energy conversion applications

Effective use of renewable energy: solar, geothermal, hydroelectric, wind and biomass, is important for reducing greenhouse gas (e.g., CO_2) emissions that does not lean upon fossil resources (e.g., coal, petroleum, natural gas, shell gas) [72]. Among them, solar energy is the most abundant, but limited by the utilization technologies. Although the harvesting and storage techniques of solar energy are attractive and promising to solve the environmental pollution problems, the implementation of solar energy technologies has been limited by high costs, relatively low efficiency and resource intermittency issues (**Figure 18**). Therefore, tremendous researches have been devoted to conversion and storage of solar energy, with a focus on increasing conversion efficiency and reducing manufacturing costs.

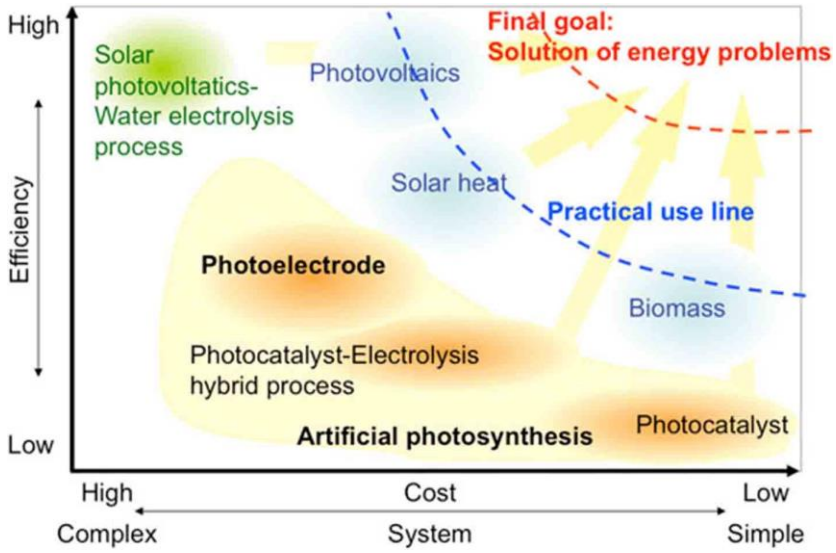

Figure 18. Efficiency−cost comparison of various solar energy conversion technologies.[72]

In **Figure 18**, the conversion efficiency of solar light directly into electricity (PV effect) has the highest theoretical efficiency, compared with that of biomass and solar heat. Moreover, artificial photocatalyst, especially in semiconductor materials, has been extensively investigated for directly converting sunlight into chemical energy for fuel gas (H_2, etc.) production due to low cost, simplified fabrication and flexibility [73]. Thus, these two methods of converting solar energy (PV and photocatalytic) with particularly focus on multiferroic materials will be discussed in the following parts.

1.3.1. Photoconductive and photovoltaic effects

Photodiode is a semiconductor device directly converting light into an electrical current which is generated when photons are absorbed in the photodiode generally in a *p*-*n* junction (PN) or *p*-*i*-*n* junction (PIN) configuration. A photon with sufficient energies ($\geq E_g$) is absorbed by the active absorber in diode, thus it creates a hole-electron pair. This phenomena is known as the photoelectric effect. If the absorption occurs in depletion region of PN or PIN junctions, these

charge carriers are separated by the built-in electric field in the depletion region, and collected by electrodes, thus photocurrents are produced.

The photodiode exhibits two type of work mode (**Figure 19**): one is photoconductive mode, also called as photodiode mode, such as photodetector, photosensor and another is PV mode like solar cell.

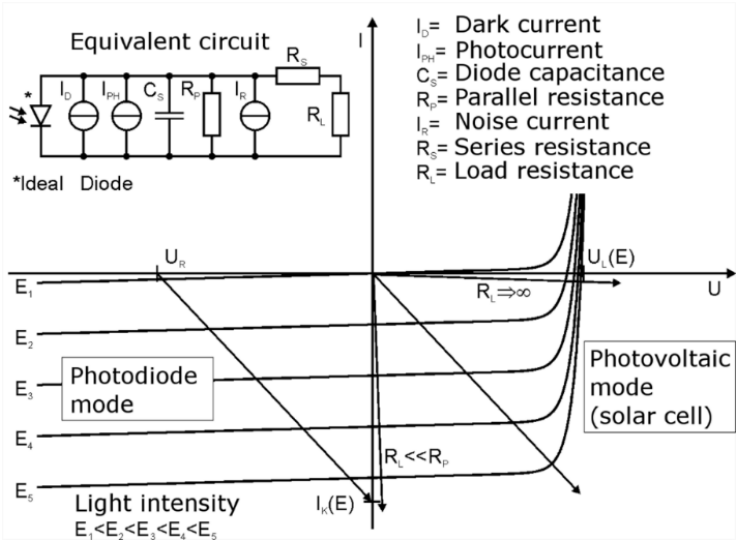

Figure 19. Current (*I*)-voltage (*V*) characteristic of a photodiode. The linear load lines represent the response of the external circuit: *I* = (Applied bias voltage − Diode voltage)/Total resistance. The points of intersection with the curves represent the actual current and voltage for a given bias, resistance and illumination.[74]

1.3.1.1 Photoconductive mode (photodiode mode)

In this photoconductive mode, also known as photodiode mode, the diode is often used at reverse biased (with the cathode driven positive with respect to the anode) and exhibiting a very low photocurrent (generally in the order of ~nA or μA). Thus it reduces the response time due to the increased width of the depletion layer by the additional reverse bias and decreasing capacitance of junction. The typical PN junction photodiode is very sensitive to light so when

light or photons falls on the photodiode it easily converts light into electric current (**Figure 20(a)**) [75]. It is sometimes referred as photo-detector, photo-sensor, or light detector. Solar cell is also known as large area photodiode because it converts solar energy or light energy into electric energy. However, solar cell works only at zero bias under light illumination.

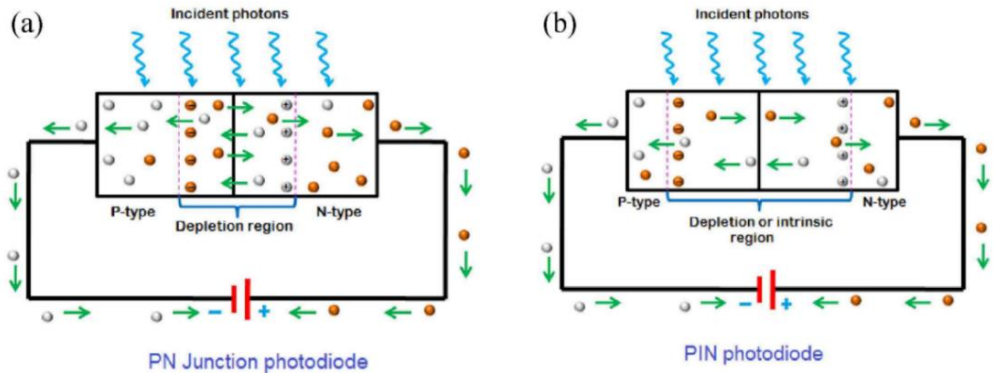

Figure 20. Schematic illustrations of (a) PN junction and (b) PIN junction photodiodes, showing the process of photocurrent generation.[75]

A PIN photodiode is made of heavily doped *p*-type material and *n*-type material separated by a highly resistive intrinsic absorber to increase the width of depletion region. Therefore, the *p* region and *n* region in the PIN photodiode have large number of charge carriers to carry electric current (**Figure 20**(b)). However, these charge carriers will not carry electric current under reverse bias condition. PIN structure is mostly used for constructing the photodiode instead of PN junction structure because PIN structure provide fast response time due to its larger depletion region. PIN photodiodes are mostly used in high-speed photoconductive applications.

Certain crystalline semiconductors, such as Si, Ge, CdS, and the related semimetal Se, are strongly photoconductive, even they are normally not electrical conductor due to less of

free electrons in semiconductors which move under voltage. For example, GaAs based PIN photodetectors [76], n-Ge/i-Ge/p-Si based PIN photodiodes [77]. Recently, graphene is widely studied for high-photoresponse photodetectors applications. Doped or intrinsic metal oxides are more and more attractive to use in photodiodes, such as ZnO nanowires based photodetectors [78], TiO_2 based photodiodes [79] and $BiFeO_3$ thin-film photodiodes [80].

1.3.1.2 Photovoltaic (PV) mode

Contrast to the photodiode mode, the diode is used at zero bias in PV mode, and the photocurrent is much higher than that of photodiodes (cf. **Figure 19**), but photon-to-current response time increased. This PV effect is the basis for solar cells, a kind of large area photodiode.

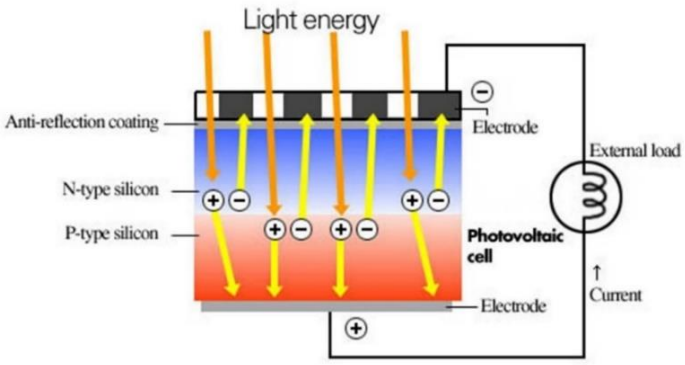

Figure 21. Schematic representation of a typical Si based *p-n* junction PV cell under light.[81]

Free electrons cross the junction between two different crystals of semiconductors more easily in one direction than in the other, giving one side of the junction a negative charge, and therefore, a negative voltage with respect to the other side, just as one electrode of a battery has a negative voltage with respect to the other. In *p-n* junction PV devices (**Figure 21**), the difference of the Fermi level of photogenerated carriers represents the photovoltage, which is

generally less than the bandgap of semiconductor and the total open-circuit voltage usually lower than 1 eV is determined by the difference in work functions of the two electrodes [82].

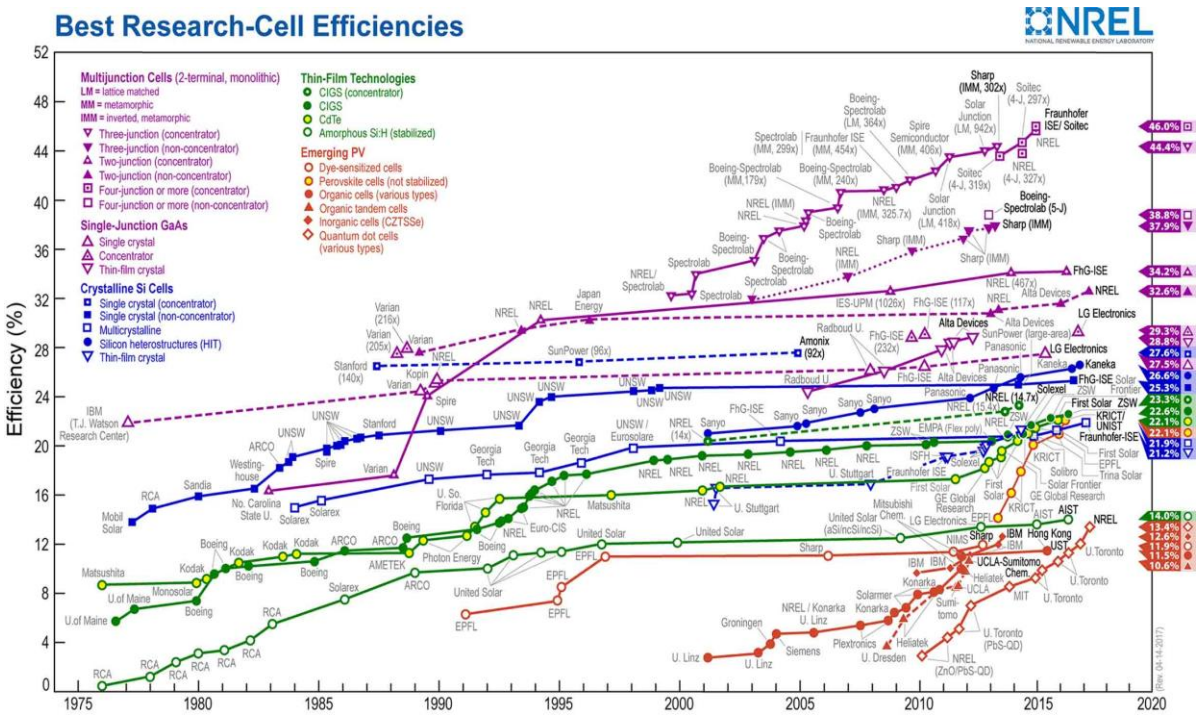

Figure 22. NREL best research cell efficiencies.[87]

While crystalline Si based devices have been the dominant solar cells in first generation type with the achieved highest power conversion efficiency (PCE) of ~27%, novel materials are being explored in pursuit of improved PCE and low cost. For examples, $Cu(In,Ga)Se_2$ (CIGS) [83], CdTe [84], GaAs [85] thin films devices have been studied as the second generation solar cells with achieved highest PCE of ~22% [86]. Meanwhile, the emerging PV cells have been also more and more attractive and promising for enhancing the PCE of solar cells, such as dye-sensitized cells, organic cells (polymer based), inorganic cells (metal oxides

based), perovskites based cells and the third generation solar cells on basis of quantum dots, as shown in **Figure 22**.

1.3.1.3 Power Conversion Efficiency (PCE)

The power conversion efficiency (PCE, η) of a solar cell, defined by the electric energy output divided by the solar energy it absorbs, is expressed as following **equation (1)**:

$$\eta = \frac{FF \times J_{sc} \times V_{oc}}{P_{in}} \times 100\% \quad , \qquad (1)$$

where J_{sc} is the short-circuit current density, V_{oc} is the open-circuit voltage, and FF is the fill factor, which is the ratio of maximum obtainable power ($P_{MPP} = V_{MPP} \times J_{MPP}$, MPP: maximum-power-point) to the product of the V_{oc} and J_{sc}, P_{in} is the power of incident light, as illustrated in **Figure 23**. To design an efficient solar cell, we have to consider to make these parameters J_{sc}, V_{oc}, and FF as optimum as possible.

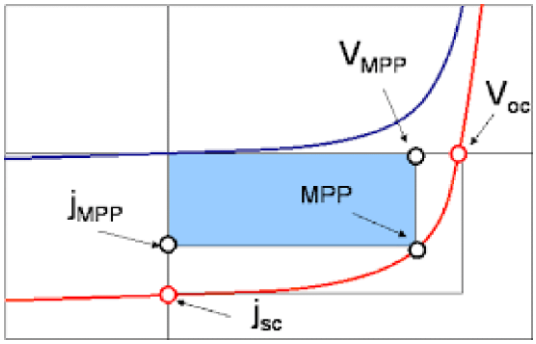

Figure 23. Schematic representation of dark (blue) and light (red) current voltage characteristics of a PV cell. The different quantities like open circuit voltage V_{oc} and short circuit current density J_{sc} are shown.[88]

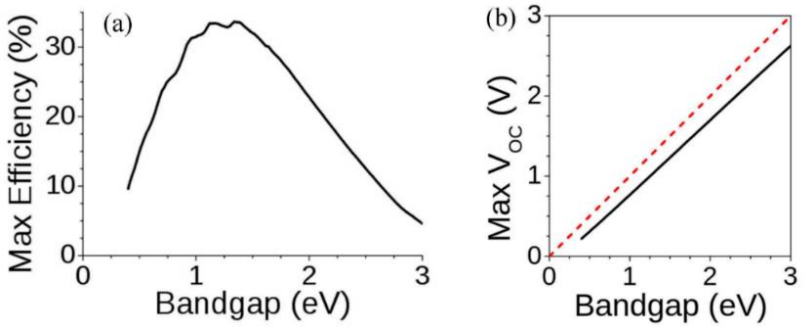

Figure 24. (a) The Shockley-Queisser (S-Q) limit for the efficiency of a solar cell, without concentration of solar radiation. (b) Maximum V_{oc} in the S-Q model vs. bandgap of materials.[89, 90]

The Shockley–Queisser (S-Q) limit [89] refers to the maximum theoretical PCE of a solar cell using a single PN junction to collect power from the cell. The maximum PCE around 34% assuming a single PN junction with a bandgap of 1.34 eV (using an Air Mass (AM) 1.5G solar spectrum). That is, of all the power contained in sunlight falling on an ideal solar cell (about 100 mW cm^{-2}, 1 sun), only 34% of that could ever be converting into electricity (34 mW cm^{-2}). For example, the crystalline Si, the dominant material of solar cells in industry, has a slightly smaller bandgap of 1.1 eV, yielding in a maximum PCE of ~ 32%, as shown in **Figure 24**(a) [89]. **Figure 24**(b) [90] shows the limit for V_{oc} in the S-Q model (i.e., voltage at zero current). The red dotted line shows that this voltage is always below the bandgap (the black line). This voltage is reduced by recombination of hole and electron and/or defects in semiconductor. For example, the maximum V_{oc} of Si based PV cells with bandgap of 1.1 eV under 1 sun illumination is about 0.8 V.

1.3.2. Bulk Photovoltaic Effect (BPV) in Ferroelectrics

FE materials exhibit unique peculiar PV effect called as bulk photovoltaic (BPV) effect due to their non-centrosymmetric structures, unlike conventional semiconductor PN junction [91]. A FE thin film could have an E_{int} throughout the bulk region originating from electrical polarization that is not completely canceled out by screening charges (**Figure 25**(b)). Thus, PV effects are not limited to an interfacial region (**Figure 25**(a)) [92] and they can be generated without forming complex structures. In addition, the photo-induced voltage output (photovoltage) in a FE thin film is not limited by an energy bandgap, as with semiconductor-based PV cells (in which the photovoltage is typically below 1 V).

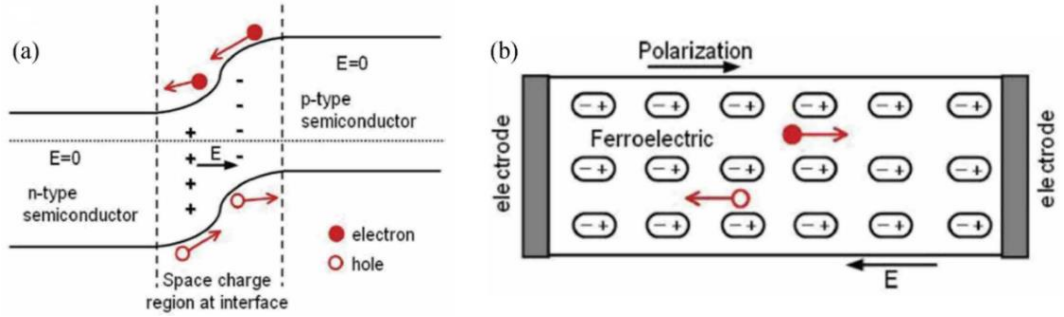

Figure 25. Simplified schematics for (a) the interfacial PV effect in a semiconductor *p-n* junction and (b) the BPV effect in a FE thin film. E: Electric field.[92]

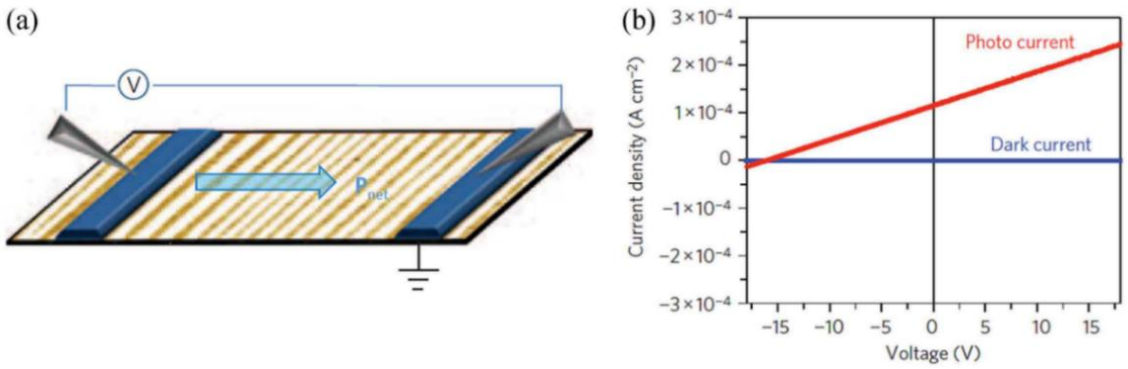

Figure 26. (a) Schematics of the *I*−*V* curves measurements involved into the multiferroic BFO with geometry of electrodes for electric transport measurements perpendicular (DW⊥). (b) Corresponding *I*–*V* measurements yielding a V_{oc} of about 16 V.[93]

It has been recently shown that BPV effect in FE materials has potential to boost the PCE and even to overcome the S-Q limit. For example, **Figure 26**(a) [93] shows the current–voltage (*I*-*V*) characteristics of BFO (E_g≈2.6−2.7 eV) with ordered arrays of 71° domain wall (DW), were measured under saturation illumination on the same film in both dark and white-light illumination (285 mW cm^{-2}). In the DW⊥ (electrodes for electric transport measurements perpendicular, domain wall perpendicular) direction, a large photo induced V_{oc} of 16 V, higher than its bandgap energy beyond the S-Q limit was achieved, as shown in **Figure 26**(b). Thus, ferroelectrics with the BPV effect are thought to have huge potential in PV applications.

1.3.3. Photocatalytic water splitting

Artificial photosynthesis is the fourth solar energy utilization technology to be developed, after solar power, solar heat, and biomass technologies (**Figure 18**). Among artificial photosynthesis technologies, the solar hydrogen production technology that produces hydrogen and oxygen by directly decomposing water with a semiconductor photoelectrode (**Figure 27)** is a low-cost technology and has been studied extensively as a fundamental technology for the future. The development of a solar hydrogen production system would contribute to solve the energy problems. However, the reported solar-to-hydrogen (STH) efficiencies for the typical oxide semiconductor photoelectrodes are as low as 0.69 % for only oxides based devices and 1.1 % for Pt/oxides based devices [72]. A high-performance system with different materials and

structures based photocatalysts therefore needs to be developed, such as InGaN nanowires [94], PbS/CdS quantum dots [95], FE oxide thin films [96].

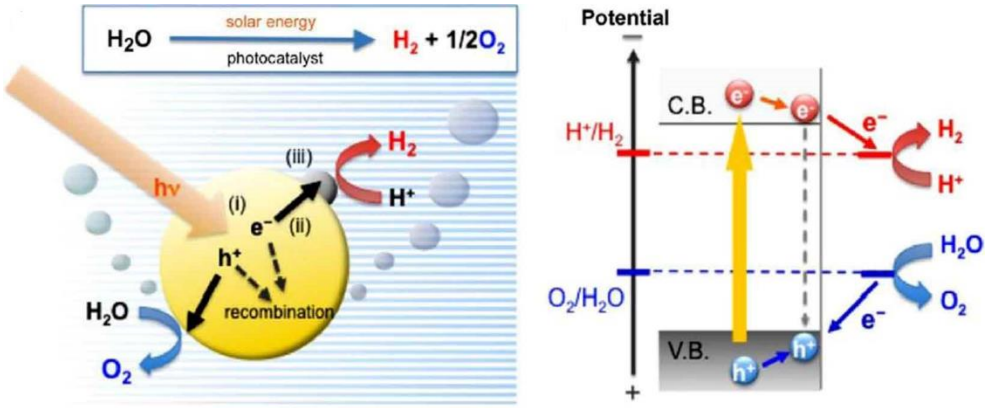

Figure 27. Principle of hydrogen production by water electrolysis using a semiconductor photoelectrode.[97]

Figure 28 shows the theoretical photocurrent as function to the bandgap (E_g) of materials. The theoretical photocurrent is calculated assuming that all incident photons above the semiconductor E_g contribute to the photocurrent. According to theoretical calculations that think about over-potentials and other losses, the target E_g for photoelectrodes are between 1.1 and 1.7 eV for optimized efficiency, relating to the materials like Si, InP, GaAs, CdSe. However, on the basis of looking for several typical semiconductors for photoelectrochemical (PEC) applications, the choice of available materials with E_g ranging between 1.5 and 2.0 eV is limited. In addition, unlike PV cells, which aim to maximize power output, the nature of the chemical reactions in artificial photosynthesis requires a minimum voltage output to drive the chemical reaction. Therefore, not only the E_g of the materials, but also the band alignment and the resultant photovoltage output of the junction are important.

For the photocathode, generally uses *p*-type materials for water reduction to hydrogen evolution, Si (E_g≈1.12 eV) [98] and InP (E_g≈1.34 eV) [99] have been reported to generate high current densities of 44 and 35 mA cm^{-2}, respectively, and V_{OC} of greater than 500 mV. Comparatively, the photoanode, which is made of *n*-type materials for water oxidation to oxygen evolution, is relatively seldom to study and thus deserves more attention. Currently, there is no stable photoanode capable of achieving a photocurrent of greater than 10 mA cm^{-2}, while at the same time providing adequate photovoltage to couple with the photocathode.

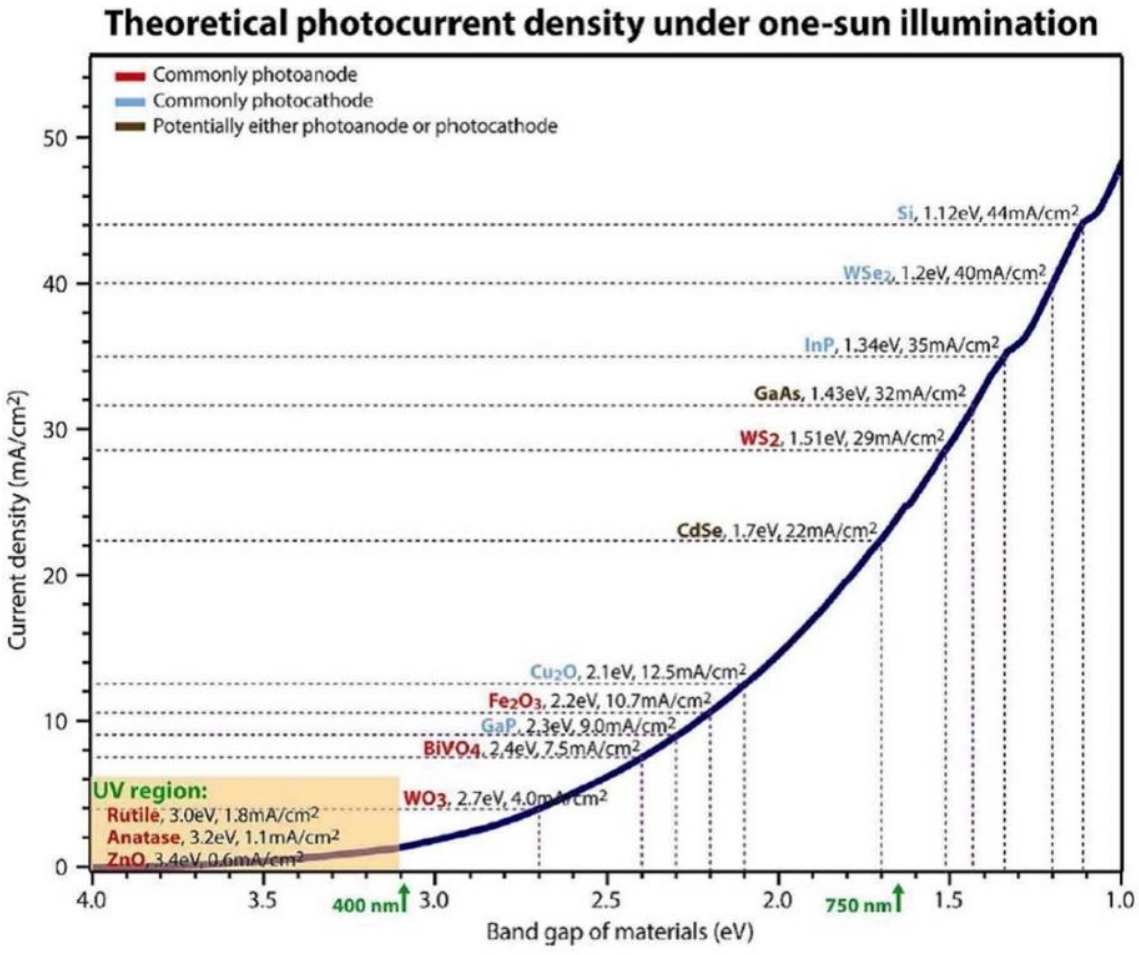

Figure 28. Theoretical photocurrent densities for semiconductors under one-sun illumination. The blue curve is the integrated photon flux at different cutoff energies, based on the AM 1.5G

solar spectrum. The green arrows at the bottom indicate the regions of ultraviolet (UV) (below 400 nm), visible (400−750 nm), and infrared (IR) spectra.[100]

In semiconductor photoelectrode for water splitting, after rapid non-adiabatic relaxation, photo-excited carriers may recombine radiatively or non-radiatively before diffusing to the near-surface region to drive redox reactions, as shown in **Figure 29**. In the crystalline semiconductor photocatalysts, wherein the carriers' extraction is no longer limited by thermodynamic diffusion, the transport of spatially separated electron–hole pairs to the photocatalyst surfaces is often determined by the surface band bending [101]. Shown in the insets of **Figure 29**, the presence of an upward- (downward-) surface band bending has been commonly measured for n- (p-) type semiconductor photocatalyst.

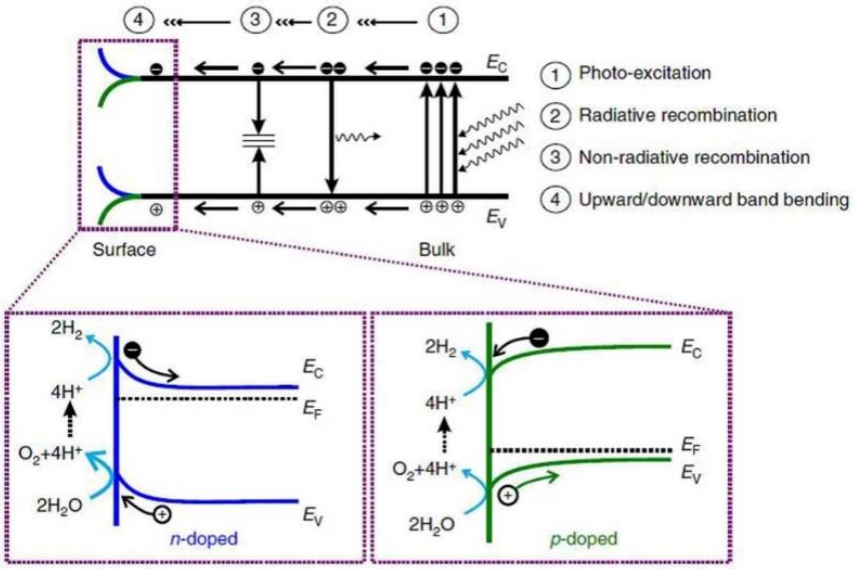

Figure 29. Schematic of carrier generation, radiative and non-radiative recombination processes. The four electron–hole water splitting mechanism is illustrated on *n*- (*p*-) doped semiconductors with upward- (downward-) surface band bending in the two bottom panels.[94]

The energy barrier induced by the upward band bending drives back the photo-excited electrons toward the bulk region, creating an electron depletion (hole accumulation) layer at the surface. While the oxidation reaction of water proceeds efficiently on *n*-doped semiconductor surface, the reduction reaction is suppressed due to the presence of upward band bending. In the case of *p*-doped semiconductor, the oxidation reaction and consequently the reduction reaction are suppressed due to the presence of downward band bending at the surface.

1.3.4. Multiferroics for solar energy conversion applications

Multiferroic systems have been recently explored as alternative materials for use in solar energy conversion applications, such as photodetectors, PV and photoelectrochemical (PEC) devices [102]. In these non-centrosymmetric systems, the low inversion symmetry state with spontaneous electric polarization induced by FE dipoles enhances the separation of photo-excited carriers and allows the generation of photovoltages larger than the E_g. This enables PCE exceeding the S-Q limit [91], a well-established concept in conventional semiconductor *p-n* junction solar cells. More interestingly, the tailoring performance of those devices could be achieved by tuning internal FE polarization state of multiferroics. This technology involves a simplified device architecture, low cost fabrication methods as well as chemically stable and earth-abundant starting materials.

1.3.4.1 Multiferroics based photodetector

The multiferroic materials also offer a potential opportunity for use in optoelectronic devices, including photodetectors, such as photodiodes, photomultipliers [80]. Among these applications, photodiodes are widely used in integrated circuitry (for control and switching, or digital signal processing); consumer electronics devices; optical communications, and light

regulation, due to its less complicated and low cost fabrication. It was previously demonstrated that the photodiode devices on photoconductive mode exhibit a higher sheet resistance (typically in the order of ~ MΩ/□) than that of its external loads and lower photocurrent density in order of ~μA/cm^2 or ~nA/cm^2 usually under reverse bias condition [103-106].

Taking the typical multiferroic $BiFeO_3$ (BFO) as example, Xing *et al.* [80] reported the fabrication of a photodetector based on BFO planar device (**Figure 30**(a)). The device exhibits a substantial zero-bias photocurrent with magnitude in order of ~nA and an open-circuit photovoltage after experiencing high voltage pulses, as shown in **Figure 30**(b). Additionally, the tailoring photocurrent was achieved by controlling the FE polarization state of BFO (not shown here). Moreover, the responsivity spectrum of devices under zero bias shows a peak sensitivity of 0.15 mA/W at 365 nm. The response time is on the order of tens of nanoseconds. All these fascinating characteristics recommend multiferroic BFO to be a potential candidate in highly-sensitive and switchable photodetectors.

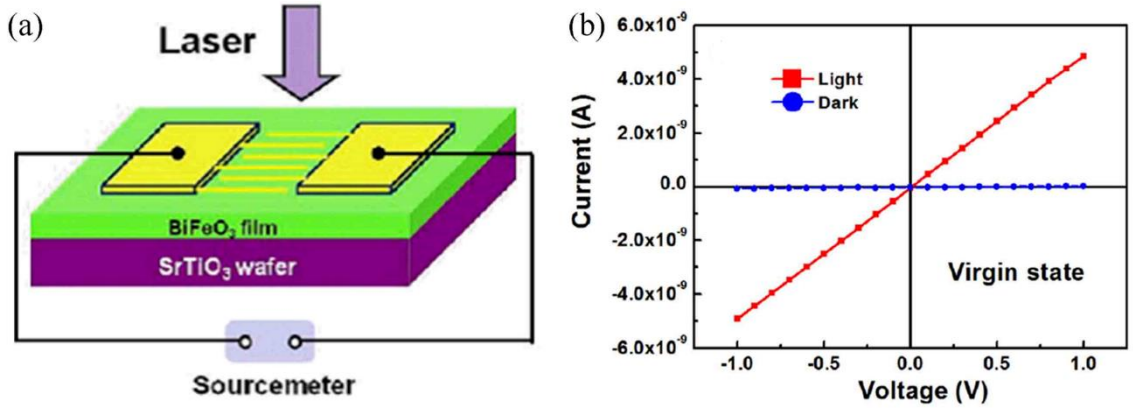

Figure 30. (a) Sketch of the multiferroic BFO based photodetector involved into a measurement circuit. (b) Corresponding photocurrent as a function of applied voltage.[80]

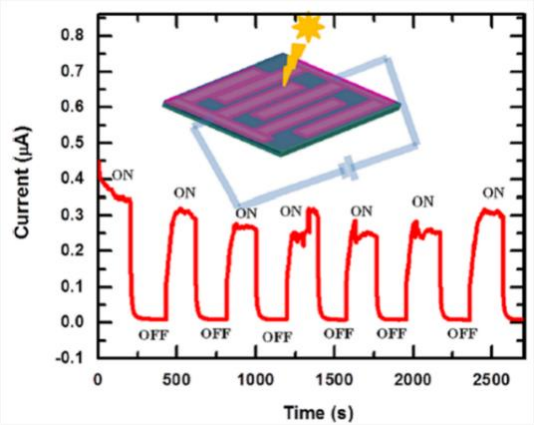

Figure 31. Photocurrent as a function of time under the illumination of weak visible light at an interval of 250 s. Schematic outlook of in-plane BFO based photodetector is given in the inset.[106]

Furthermore, Anshul *et al.*[106] reported visible-light detection with in-plane BFO thin films grown on pre-patterned inter-digital electrodes. A schematic diagram of the pre-patterned inter-digital electrodes with an arrangement of bias electric field is shown in the inset of **Figure 31**. Photocurrent in order of ~μA as a function of time is shown in **Figure 31** over large acquisition times with a period of 250 s. In-plane configured BFO film displayed photocurrents with a 40:1 photo-to-dark current ratio and improved photo-sensing ability for >4 hours under small bias voltage. They detailed only 60% of the photo-induced charge carriers' decay in 1 second with a double-exponential decay model. Sub-bandgap weak monochromatic light (1 mW cm^{-2}) shows one-fold increase in photo-charge carriers. It indicates robust reproducibility of switching states for a long time.

1.3.4.2 Multiferroics based photovoltaic device

Since the discovery of bulk photovoltaic effect (BPV) in FE materials, FESC has been extensively studied due to several unique advantages including their distinct photoelectric

conversion capability, large photo-generated voltage, and the regulation of electric field. Yang *et al.*[107] reported a PV effect in BFO (E_g≈2.6−2.7 eV) thin films. The all-oxide heterostructures with SRO bottom and ITO top electrodes (**Figure 32**(a)) are characterized by V_{oc} of about 0.8–0.9 V and external quantum efficiencies up to 10% when illuminated with the appropriate light (**Figure 32**(b)). Efficiencies are at least an order of magnitude larger than the maximum efficiency under sunlight AM 1.5G, thus far reported for FESC. The dependence of the measured efficiencies on electric poling suggests contributions to the enhanced photocurrents from the FE polarization state in BFO.

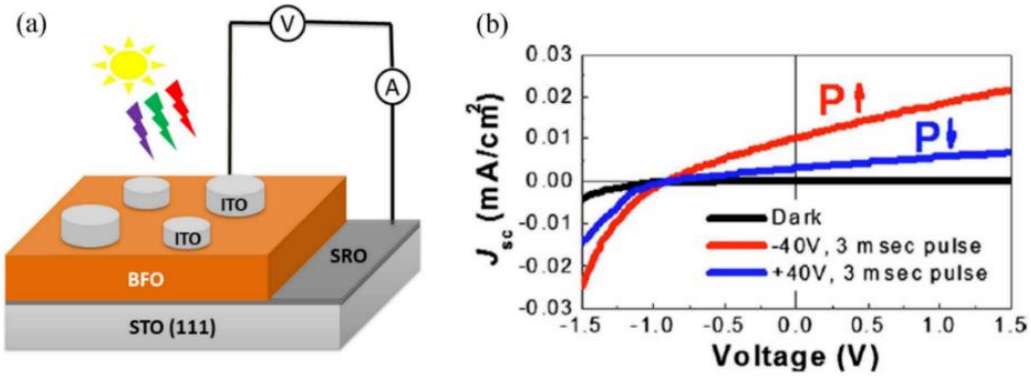

Figure 32. (a) Layout of multiferroic BFO based PV device. (b) J_{sc}-V measurements for ITO/BFO/SRO heterostructures reveal polarization (P) dependent changes in the PV properties of the device [107].

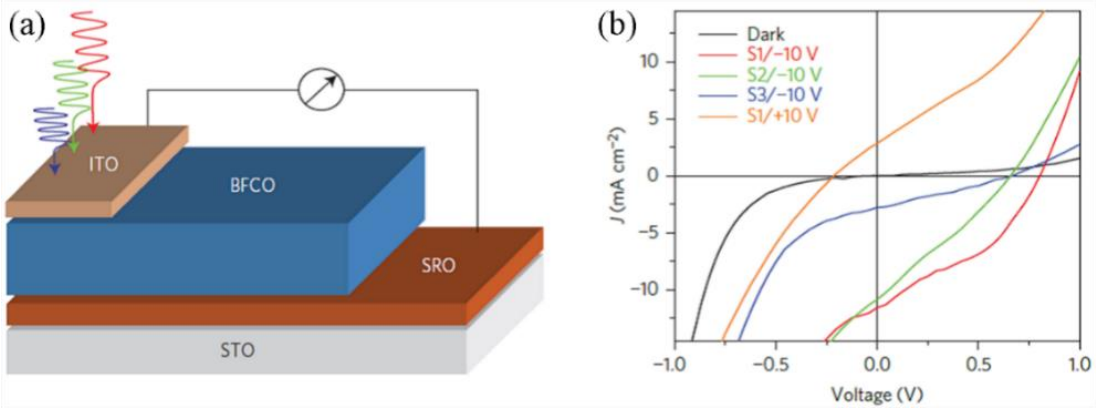

Figure 33. (a) Layout of multiferroic BFCO thin films based PV cells. (b) *J-V* characteristics of devices (S1-S2) on basis of BFCO with various bandgaps (1.5−2.2 eV) underwent different electric poling.[64]

Compared with BFO, B-site ordered double-perovskite BFCO is also multiferroics with smaller E_g varying from 1.2−2.4 eV. Nechache *et al.*[64] have devoted to study the thin films PV cells on basis of multiferroic BFCO in **Figure 33**(a), and reported a maximum PCE of ~3.3% for ITO/BFCO/SRO heterojunction device involved into a E_g of BFCO≈1.5 eV with a large photocurrent of 11.7 mA cm^{-2}. The same device underwent positively poled shows a huge reduction in photocurrent and photovoltage, yielding a diminuend efficiency owing to the unfavorable FE polarization state of BFCO, as shown in **Figure 33**(b).

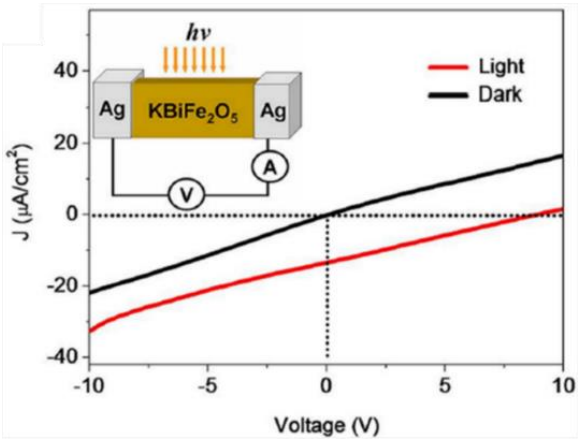

Figure 34. *J-V* curves of Ag/$KBiFe_2O_5$/Ag device in the dark and under UV illumination at RT. Inset shows the measurement setup schematically.[108]

Additionally, Zhang *et al.*[108] reported a multiferroic compound with TM oxides tetrahedral network, $KBiFe_2O_5$, which features narrow E_g (~1.6 eV) than multiferroic BFO, high T_C (780 K) and robust magnetic and photoelectric activities. The high photovoltage (~8.8

V) and photocurrent density (~0.015 mA cm^{-2}) were obtained (**Figure 34**), which is comparable to the reported BFO. The photoelectric responses were measured at RT using a single crystal illuminated by a UV-light (4 mW cm^{-2}, λ=254 nm) (inset of **Figure 34**). I–V characteristics in **Figure 34** reveal strikingly PV behavior, which is indicative of the polar nature of the sample. At zero bias, no dark current was seen but there is a negative photocurrent, with a large zero-current voltage (corresponding to the V_{oc}) of 8.8 V. This indicates that charge carriers have a preferred direction presumably because of an internal-field bias. The observation of a V_{OC} larger than E_g is a signature of PV effects in multi-domained ferroelectrics. This above-bandgap V_{oc} provides a promising platform for harvesting solar energy to generate electricity.

1.3.4.3 Multiferroics based Photoelectrochemical (PEC) cells

The remnant FE polarization induced electric fields extend over the entire volume of the film or bulk multiferroic materials, which may replace the electrical field that forms in a classical *p-n* junction, effectively separating electron-hole pairs and driving them towards electrodes. This FE polarization induced electrical field also gives rise to the modulation of the chemical potential and surface band bending of FE materials based photoelectrodes, thereby tailoring the PEC performance. Recent studies reported several FE materials based photoelectrodes such as BFCO [65], $Pb(Zr,Ti)O_3$ [109], BFO [110] and $KNbO_3$[111] demonstrating an enhanced PEC performance by regulating the FE polarization induced internal electric fields.

Song *et al.*[110] reported the fabrication of a photoelectrode on basis of the multiferroic *n*-type BFO thin films in various thickness and its application for solar water oxidation (**Figure 35**(a)). The maximum photocurrent density at 0 V vs. Ag/AgCl (reference electrode) in 0.5 M Na_2SO_4 (pH 5.67) electrolyte increases approximately to 0.01 mA cm^{-2} with 50 nm-thick BFO

film compared with other thickness oxidation (cf. **Figure 35**(b)). The enhanced PEC performance of BFO based photoanodes was achieved by tuning internal FE polarization state (not shown here). This study strongly suggests that FE materials can be used as effective charge separation and collection layers for efficient solar water-splitting photoanodes.

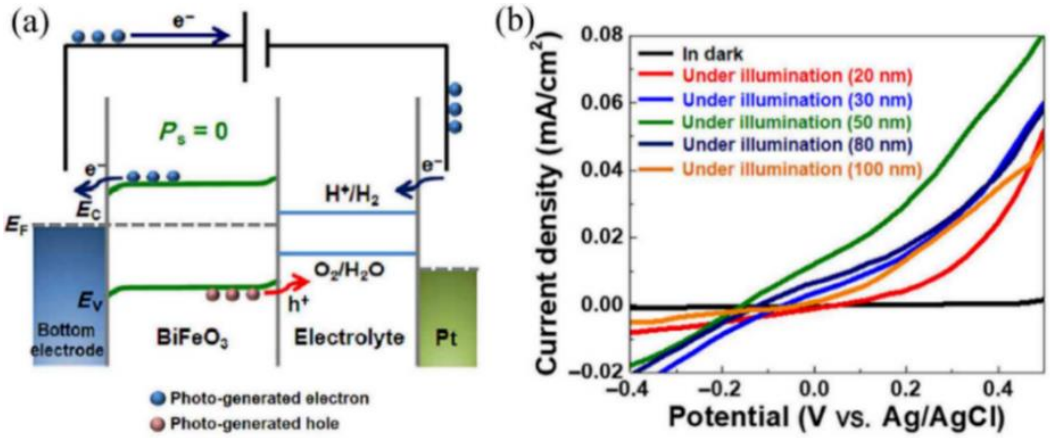

Figure 35. (a) Energy band diagrams for (001)-oriented BFO thin-film photoanodes in PEC water splitting cells in the no-polarization state. (b) Linear sweep voltammetry curves for BFO thin films in various thicknesses based photoanodes obtained in 0.5 M Na_2SO_4 (pH = 5.67) under light.[110]

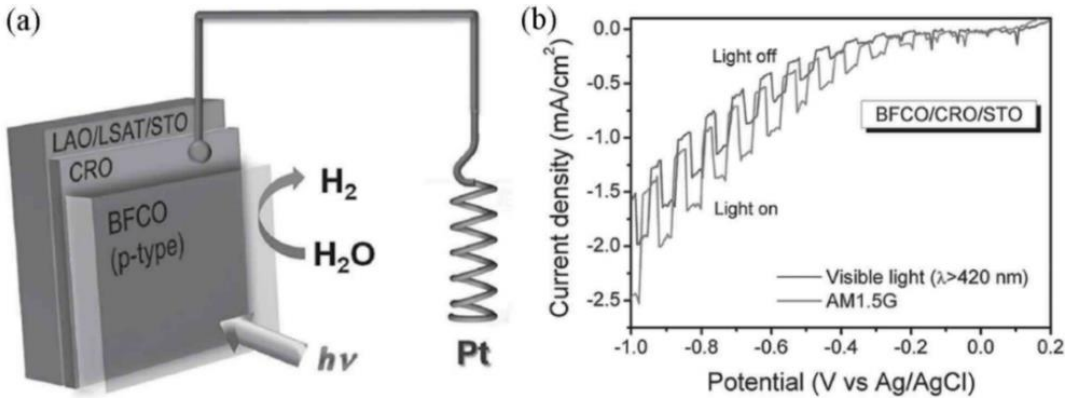

Figure 36. (a) Diagram of a PEC cell showing the *p*-type BFCO thin film used as the photocathode designed for water reduction. (b) Variations of *J*-*V* (vs. Ag/AgCl) in 1 M Na_2SO_4 at pH 6.8 under chopped simulated 1 sun illumination and visible light illumination ($\lambda > 420$ nm) of BFCO thin film grown on $CrRuO_3/SrTiO_3$ substrate by PLD.[65]

Moreover, multiferroics based photocathode for water reduction to hydrogen gas evolution was also studied in recent years. Li *et al.*[65] reported a photocathode consisting of an epitaxial double-perovskite BFCO multiferroic thin film with a suitable conduction band position and small bandgap (1.9–2.1 eV), for visible-light-driven reduction of water (**Figure 36**(a)). PEC measurements show that the highest photocurrent density up to −1.02 mA cm^{-2} at a potential of −0.97 V vs. reversible hydrogen electrode (RHE) is obtained in *p*-type BFCO thin film photocathode grown on STO substrate under AM 1.5G simulated sunlight (**Figure 36**(b)). In addition, a twofold enhancement of photocurrent density is obtained after negatively poling the BFCO thin film, as a result of modulation of the band structure by suitable control of the E_{int} gradient originating from the FE polarization in the BFCO films. Since STO is also active under UV light ($E_g \approx 3.2$ eV), they also performed *J-V* measurements under visible light ($\lambda > 420$ nm) to rule out any contributions from the STO substrate.

Chapter 2. Research Objectives and Thesis Organization

2.1. Research Objectives

The aim of this project is to elaborate approaches for (a) understanding the physical properties (e.g., structural, electronic, optical and multiferroic) of BFCO material and (b) exploit them to evaluate the potential for solar energy conversion applications including photodetectors, PV and PEC cells. The investigation will be focused on developing optimized devices based on BFCO epitaxial thin films. In *p*-*i*-*n* heterostructures, BFCO thin films will act as intrinsic absorber sandwiched between *p*- and *n*-type semiconductor oxides as hole and electron transporting layer (HTL and ETL), respectively. The BFCO combined with high internal electric field of *p*-*i*-*n* heterostructures will lead to achieve PV devices with enhanced carrier collection efficiency. For this part, my approach is outlined as follows:

(*i*) Fabrication of *p*-type transparent semiconductor.

1. Development of *p*-type transparent semiconductor based on perovskite STO. We will focus our efforts on growing epitaxially In-doped $SrTiO_3$ ($SrIn_xTi_{1-x}O_3$, $0 \leq x \leq 0.15$) thin films and optimizing of their electrical, electronic and optical properties to achieve high efficient hole transporter material with wide optical bandgap. Hybrid technique which combines PLD and MBE will be used for films deposition to control the Indium doping leading thus the investigation of its effect on physical properties of STO.

Moreover, we also fabricated the typical *p*-type NiO thin films involving into a *p*-*i*-*n* heterojunction by PLD, and investigated their structural, optical and electrical properties.

(*ii*) Design and fabrication of BFCO thin films based devices for solar energy conversion applications.

2. Fabrication of highly-sensitive switchable photodiodes based on BFCO epitaxial thin films. We investigated the switchable current−electric field characteristics by tuning FE polarization state of BFCO, and their phototransient and responsivity properties.

3. Fabrication of efficient solar cells based on BFCO thin films with *p*-*i*-*n* heterojunction. BFCO thin films sandwiched between perovskite *n*-type Nb-STO substrates and *p*-type NiO thin films were epitaxially fabricated by PLD, and we further investigated their structural, optical, FE properties and PV performances.

4. Finally, to understand the mechanism of photon-to-chemical energy applications in solar-driven water splitting, we fabricated heterojunction photoelectrodes based on multiferroic BFCO thin films coated with a *p*-type transparent conducting NiO layer by PLD. The tailoring PEC performance and enhancement of photocurrent density were achieved, and stable operation of *p*−NiO/*n*−BFCO heterojunction photoanode was confirmed by observing a constant current density over multihour.

2.2. Thesis organization

This thesis is divided into eight parts and organized as follows:

Chapter 1 generally introduces the background and basics about my projects;

Chapter 2 presents the motivation and main goals of my work;

Chapter 3 describes experimental method details, and the main characterizations for thin films and devices are also described in this chapter;

SECTION (I) *p*-Type Transparent Conducting Oxides

Chapter 4 presents the growth of single-crystalline In-doped $SrTiO_3$ epitaxial thin films with various indium concentrations by PLD+MBE and the investigation on their structural, electrical and optical properties. The publication related to this chapter is:

***W. Huang**, R. Nechache, S. Li, M. Chaker, F. Rosei, Electrical and optical properties of transparent conducting p-type $SrTiO_3$ thin films. J. Am. Ceram. Soc. **99** (1), 226–233, 2016.*[112]

SECTION (II) Bi_2FeCrO_6 Thin Films for Solar Energy Conversion Applications

Chapter 5 reports the fabrication of a sensitive switchable photodiode based on epitaxial multiferroic BFCO/SRO junctions by PLD technique. The photodiodes demonstrated a large ideality factor, a fast transient response and a large photoresponsivity. The publication related to this chapter is:

***W. Huang**, J. Chakrabartty, C. Harnagea, D. Gedamu, I. Ka, M. Chaker, F. Rosei and R. Nechache, Highly-Sensitive Switchable Heterojunction Photodiode based on Multiferroic Bi_2FeCrO_6 Epitaxial Thin Films, ACS Appl. Mater. Interface, **10** (15), 12790–12797, 2018.*

Chapter 6 presents a new device architecture to effectively enhance PV performance, *p*−*i*−*n* heterojunction PV device based on multiferroic BFCO thin films. Under 1 sun illumination, the optimized *p*−*i*−*n* device achieved a PCE of 2.0%, a 4−fold enhancement compared to the *i*−*n* device architecture. The publication related to this chapter is:

***W. Huang**, C. Harnagea, D. Benetti, M. Chaker, F. Rosei and R. Nechache, Multiferroic Bi_2FeCrO_6 based p-i-n Heterojunction Photovoltaic Devices, J. Mater. Chem. A, **5**, 10355–10364, 2017.*[113]

Chapter 7 reported a photoanode based on *p*-NiO/*n*-BFCO heterojunction. The *p*-NiO/*n*-BFCO heterojunction photoanodes demonstrated an enhanced photocurrent density and multihour stability in Na_2SO_4 (pH≈6.8) electrolyte under illumination. The publication related to this chapter is:

***W. Huang**, C. Harnagea, X. Tong, D. Benetti, S. Sun, M. Chaker, F. Rosei, and R. Nechache, Enhanced Photoelectrochemical Performance in Multiferroic Oxide Thin Films coated with p-Type Transparent Conducting Oxides, Submitted, 2018.*

Chapter 8 finally summarizes the most important contributions of this work and suggests future prospectives of BFCO in the field of solar energy conversion.

Following the main body of this thesis is an appendix containing a summary of this thesis in French according to INRS policy.

Chapter 3. Experimental Methods

3.1. Deposition Techniques

3.1.1. Molecular Beam Epitaxy (MBE)

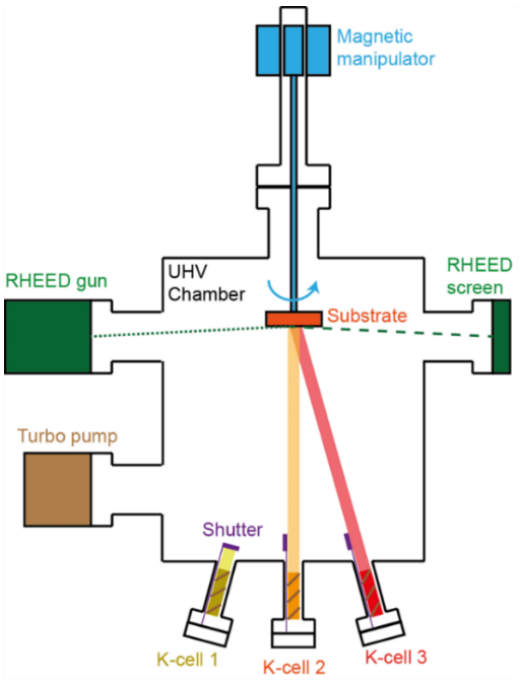

Figure 37. Schematic of a typical Molecular Beam Epitaxy (MBE) chamber.[114]

The most advanced growth method for achieving high quality thin films of metals oxides is molecular beam epitaxy (MBE), which builds crystals atomic layer by atomic layer by thermally evaporating the crystal's constituent elements. A schematic of a typical MBE system appears in **Figure 37**. Epitaxial growth is achieved in ultrahigh vacuum (10^{-10} Torr) chambers. The simplicity of MBE permits *in situ*, real-time analysis of crystal quality, using reflection high-energy electron diffraction (RHEED). The diffraction patterns from electrons incident upon the crystal provides information about the quality, and progression of growth. Sample

holder with a substrate is attached to a magnetic manipulator which can be rotated during growth. K-cells are attached to the bottom of the chamber, pointing towards the substrate. Selective opening of shutters on each K-cell ensures the growth using only specific elements.

3.1.2. Pulsed Laser Deposition (PLD)

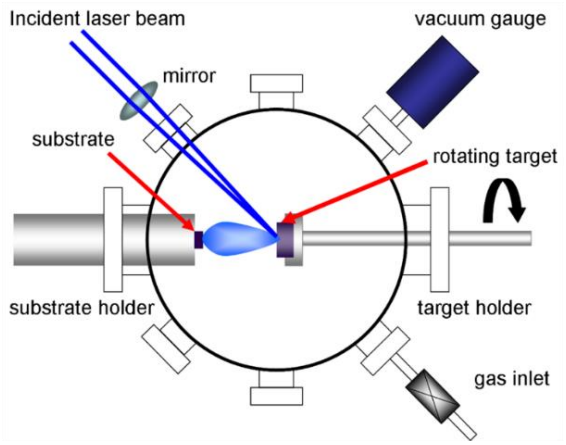

Figure 38. Schematic illustration of the pulsed laser deposition (PLD) setup.[115]

Pulsed laser deposition (PLD) is a thin film deposition technique where a high power pulsed laser beam is focused inside a vacuum chamber to strike a target of the material that is to be deposited, as shown in **Figure 38**. When the incident focusing laser beam bombards the rotating target, the rise of the localized temperature causes vaporization of the material. It is a feature of plasma plume with high energetic species, for example, ions, electrons, atoms, molecules, clusters, particulates and molten globules. This process can occur in ultra-high vacuum or in the presence of a background gas, such as oxygen. Inside the PLD chamber, a target and a substrate holder are aligned on the same line but are separated by a distance of 5 to 6 cm. Such distance range has been well experimentally confirmed for efficient laser ablation.

The PLD generally can be divided into the following four stages [116]:

1) Laser radiation interaction with the target;

2) Dynamic of the ablation materials;

3) Decomposition of the ablation materials onto the substrate;

4) Nucleation and growth of a thin film on the substrate surface.

The film growths depend on several parameters, such as laser fluence, laser repetition rate, substrate temperature and vacuum level. By adjusting the number of laser pulses on the targets, different layers with controllable thicknesses can reach.

In our experiment, PLD system (i.e., IPEX) using a KrF excimer laser (λ=248 nm, pulse duration=25 ns) was employed for ablation with an incidence angle of the laser beam on the target of 45º. In order to get high quality thin films, four parameters were carefully controlled: substrate temperature, energy of the atom flux, relative and absolute arrival rate of the atoms for compound films, and the partial pressure of oxygen in the chamber. All targets including BFCO, NiO, $SrRuO_3$ and ITO were purchased from commercial company. Substrates including single-crystalline perovskite $SrTiO_3$ and 0.5 *wt*% Nb-$SrTiO_3$ were purchased from MTI Company.

3.1.3. Hybrid Deposition (PLD + MBE)

A homemade hybrid PLD (i.e., Pulse Master)-MBE system was used to deposit indium-doped STO thin films using different growth parameters, as shown schematically in **Figure 39**. A bulk undoped STO target and indium beads were used as PLD target and MBE source, respectively. In our experiment, PLD system using a KrF excimer laser (λ=248 nm, pulse duration=25 ns) was employed for ablation. The chamber base pressure is 1.0×10^{-7} Torr. Indium beads (99.999% metals basis) for evaporation at different temperatures (RT−850 °C)

were purchased from Sigma-Aldrich Company. The STO target was purchased from Crystech Company. The double-polished transparent single-crystalline (100)-oriented $LaAlO_3$ substrates were purchased from MTI Company.

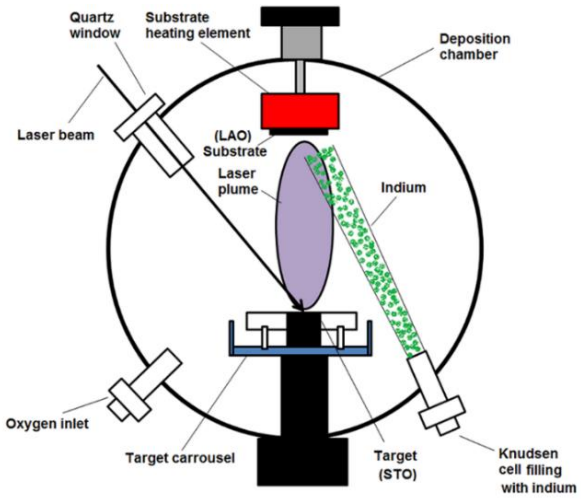

Figure 39. Schematic illustration of the hybrid deposition setup combined PLD+MBE.[112]

3.2. Characterizations

3.2.1. Characterizations of Thin Films

X-ray diffraction (XRD): The crystal structure, growth orientation and lattice parameters of the films were examined using XRD (Panalytical X'pert pro diffractometer using CuK_a radiation, Westborough, MA) by performing θ-2θ scan, Φ-scan, and reciprocal space mapping (RSM) measurements, respectively. The thickness of the films was measured by X-ray reflectometry (XRR) using the same XRD system.

Atomic Force microscopy (AFM) and **Piezoresponse force microscopy (PFM)**: AFM imaging was used to characterize the surface morphology and roughness of the grown films. PFM implemented on the same Veeco Enviroscope AFM instrument was used to study the FE

properties of BFCO films. Nanoscale measurements of FE properties were performed by PFM using the same AFM setup. We applied an AC voltage of 0.5 V at 26 kHz between the conductive probe (type MESP from Bruker) and the conductive Nb-STO substrate and detected the BFCO film surface induced piezoelectric vibrations using a lock-in amplifier from Signal Recovery (model 7265).

Ferroelectric properties at macro-scale of BFCO films were measured using a thin-film analyser system (TFA 2000) at different frequency.

Four-point probe station: The electrical properties of the films were measured using a four-point probe station (Summit 12000).

X-ray photoelectron spectroscopy (XPS) and **ultraviolet photoelectron spectroscopy (UPS)**: The chemical composition of thin films was semi-quantified by XPS using an aluminum $K\alpha_{12}$ twin monochromatic source. The band structure and fermi level of thin films were determined by UPS equipped with XPS instrument using an ESCA Escalab 220i XL spectrometer with a monochromated Al Kα X-ray source (1486.6 eV).

Hall Effect measurements were used to determine the type of charge carrier, the mobility and the concentration of carriers using a homemade setup. The measurements were carried out with various magnetic field (0.1–1.0 Tesla) at RT.

UV-Vis spectroscopy: Optical transmittances for the films (e.g., In-STO, NiO, BFCO) were performed using a Cary 5000 UV-Vis-NIR spectrophotometer (Varian) with a scan speed of 600 nm/min.

Photoluminescence (PL) spectroscopy and **Time-Resolved Photoluminescence (TRPL)**: PL spectra were acquired using a 355 nm laser excitation source. TRPL decay transients

measured at 500 nm demonstrated the sensibility of the device by a 383 nm laser excitation source at a 30 s acquisition time.

Spectroscopic Ellipsometry: To investigate the optical properties of the obtained BFCO heterostructures, ellipsometry measurements were performed at RT in the 1.25 to 3.35 eV range at three angles of incidence (i.e., 55, 65, and 75°) using a VASE ellipsometer (J.A. Woollam Company). The absorption coefficient α of the films was obtained from k by using the following formula: $\alpha=4\pi k/\lambda$, where λ is the wavelength of the incident light. The E_g of films was calculated according to Tauc's relation using the following equation: $\alpha E=A(E-E_g)^n$, where E is the photon energy, A is a constant, and n is equal to 1/2 or 2 for direct or indirect gap materials, respectively. In our data, the lack of the characteristic shape of the $(\alpha E)^{1/2}$ vs. E plot and the linear dependence of $(\alpha E)^2$ vs. E reveals that the bandgap of the films is direct.

3.2.2**.** Characterizations of Devices

Photocurrent-Voltage *(J*-V) curves: the photocurrent-voltage characteristics of the devices were recorded using a Keithley source meter. One sun illumination was obtained by an AAA class sun simulator equipped with an AM 1.5G filter having an irradiation intensity of 100 mW/cm^2.

Electrochemical Impedance Spectroscopy (EIS): The capacitive component of the complex impedance in the depletion region of $i-n$ and $p-i-n$ devices was recorded by EIS, which was conducted in the dark using a SOLARTRON 1260 A Impedance/Gain-Phase Analyzer. The applied AC signal was 10 mV in amplitude, in the frequency range between 1 Hz and 1 MHz. All the samples were measured inside a Faraday cage.

External Quantum Efficiency (EQE) spectra for BFCO-based solar cells were measured using an EQE 200 Oriel integrated system by employing a monochromator combined with an optical chopper and a lock-in amplifier. The measurement step was 10 nm.

Current-Electric field (*I*–*E*) curves characteristics of the device were recorded using a source meter (Keithley 2400). The illumination with intensity varies from 50 to 100 *m*W/cm^2 was obtained by an AAA class sun simulator equipped with 1.5 AM filter.

Photoresponsivity: The spectral responsivity for BFCO-based photodiodes was measured using a monochromator combined with an optical chopper and a lock-in amplifier.

Photoelectrochemical Analyse: Photocurrent measurements were performed in a three-electrode configuration consisting of an Ag/AgCl reference electrode, a Pt counter electrode, and a BFCO thin-film heterojunction working electrode. The bottom electrode was connected with a Cu wire using silver paste. The entire sample, except the thin film surface, was then covered by insulating epoxy to eliminate leakage current. All PEC measurements were conducted in an electrolyte consisting of 1 M Na_2SO_4 (pH≈6.8). Photocurrent density-voltage (*J*-*V*) curves were measured under simulated sunlight (100 mW/cm^2) employing a Compact Solar Simulator Class AAA (Sciencetech SLB-300A). The following formula $V_{RHE} = V_{Ag/AgCl} + V^0_{Ag/AgCl} + pH\times0.059$, where $V^0_{Ag/AgCl} = 0.1976$ at 25°C, was used to convert the measured potentials (vs. Ag/AgCl) to the potentials vs. the reversible hydrogen electrode (RHE) in electrochemical measurements by an electrochemical workstation (CHI-760D with 20 mV/s sweep rate).

Poling Treatment: To pole the BFCO thin films, including ITO/BFCO/NSTO, BFCO/SRO, the polarization of BFCO was oriented upward (downward), denoted as P_{up} (P_{down}), by applying +15 V (−15 V) electrical voltage pulse during 1 μs.

Mott–Schottky Analyses were carried out using an electrochemical impedance method with AC amplitude of 20 mV at an applied frequency of 1 and 2 kHz.

Incident Photon-to-Current Efficiency (IPCE) for BFCO-based PEC cells was calculated by current−voltage measurements using different band-pass optical filters. To confirm the contribution of infrared photons to the photocurrent, band-pass filters (from Edmund Optics), which have wavelength center at 405, 460, 505, 694, and 785 nm, respectively. For each filter, the incident radiation intensity at the position of the sample was measured using a Newport power-meter.

It is worth mentioning that all the measurements were carried out at RT (~300 K) except the measurement of electrical conductivity with temperature.

SECTION I. *p*-Type Transparent Conducting Oxides

Chapter 4. *p*-Type Indium-doped $SrTiO_3$ Thin Films

Perovskite $SrTiO_3$ (STO) with doping is becoming an extremely attractive transparent conducting oxide (TCO) as a conductive layer in perovskite-based oxide devices [117, 118], due to its chemically stable structure, smooth surface and small lattice mismatch with other perovskite oxides (e.g., there is a ~0.5% lattice mismatch between $BiFeO_3$ thin films and Nb-doped STO substrates [119]). STO can be used in a wide range of applications for optoelectronic and microelectronic devices, such as dynamic random access memories (DRAM), micro-capacitors, optical switches, electro-optic devices and substrate material for the growth of oxide thin films [120-122].

Undoped bulk STO is an insulator at RT with a large $E_g \approx 3.2$ eV, due to its closed shell d^0 electron configuration [121]. Insulating STO can be transformed into a semiconductor or conductor by creating defect levels close to the conduction or valence bands, for example by doping either the Sr^{2+} sites with La[123] or Ho[124] ions, Ti^{4+} sites with Nb[125] or In[126] ions, or by forming oxygen vacancies. The donor-doped STO (*n*-type) has been intensively studied for a long time, while the acceptor-doped STO (*p*-type) is seldom reported. Kato *et al.*[127] investigated the electrical conductivity of a *p*-type STO thin film doped using Sc^{3+} as acceptor ions. Iwashina *et al.*[128] reported a *p*-type Rh-doped STO photocatalyst electrode for water splitting under visible-light irradiation. Guo *et al.*[129] first demonstrated

experimentally the optical properties of a *p*-type In-doped STO (ISTO), suggesting the great potential of using it as TCO film.

Epitaxial growth of the single-crystalline ISTO on top of the FE active layer is expected to result in high crystal quality and smooth interfaces with low density charged defects, which generally behave as recombination sites for electrons and holes. The behavior of electrical conduction and optical transparency of transparent conducting *p*-type ISTO films is poorly understood. A systematic investigation is required to further improve its properties for the design of high-efficiency perovskite oxides-based PV cells.

4.1. Experimental procedure

A hybrid PLD-MBE system was used to deposit ISTO thin films using different growth parameters, as shown schematically in **Figure 39**. Bulk undoped STO target and indium beads were used as PLD target and MBE source, respectively. 100 nm-thick films were deposited directly on (100)-oriented LAO substrates under oxygen pressures ranging from 10^{-7} to 10^{-3} Torr through using cross-beam configuration. The evaporated In atoms merged with laser-induced plasma of STO before reaching at the surface of substrate in oxygen background. The mixed plasma contained SrO, TiO_2 and In components. The STO target-to-substrate and the In source-to-substrate distances were 6 and 20 cm, respectively. The (100)-oriented LAO substrates were heated to 650˚C during deposition. To control the In content in the ISTO films, we adjusted the temperature of the MBE Knudsen cell from 350 to 850 ˚C. With this hybrid technique we were able to grow ISTO films with $x \leq 0.15$. PLD growth was achieved using a

KrF excimer laser with an energy density of about 1.8 J cm^{-2} at a repetition rate of 5 Hz. The average deposition rate was about 0.1 Å/pulse.

4.2. Structural characterizations

To achieve different concentrations of In in ISTO thin films during combined PLD-MBE deposition, different temperatures of the MBE Knudsen cell were used to adjust the effusion of In under oxygen pressure in the range from 10^{-7} to 10^{-3} Torr. The temperatures of the Knudsen cell corresponding to the In concentration *x* are listed in **Table 5**. Using these deposition parameters, we obtained a maximal doping level of about 15%. The compositions of ISTO films were semi-quantified by XPS using 3 times etching to eliminate the surface contamination, i.e. carbon. High resolution spectra of the Sr 3*d*, In 3*d*, Ti 2*p* and O 1*s* core levels were measured for each sample.

Table 5. Parameters of deposition: Temperature of MBE Knudsen cell: T (˚C); Oxygen pressure: P_{O2} (Torr)) for ISTO films with various In concentration *x*.

Samples	T (˚C)	*x*	P_{O2} ($\times 10^{-7}$ Torr)
S1	RT	0	1
S2	350	0.005	
S3	400	0.01	
S4	550	0.05	
S5	700	0.10	
S6	850	0.15	
S7	850	0.15	100
S8	850	0.15	10000

We present the ISTO film (*x*=0.15) in **Figure 40**(a)–(d) as a relevant example containing a maximal doping level of ~15%. The In substitutes for Ti sites, In concentration is reported as the ratio of In concentration to the total of Ti and In concentrations ((In)/(In+Ti)).

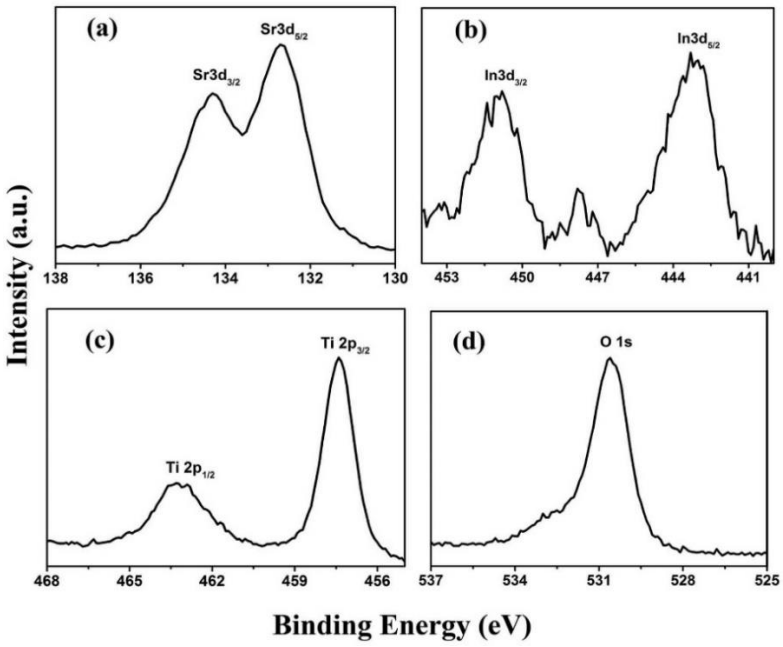

Figure 40. Representative core level spectra of (a) Sr 3*d*, (b) In 3*d*, (c) Ti 2*p* and (d) O 1*s* from ISTO film (*x*=0.15) using XPS.

Only the 00*l* (*l*=1, 2, 3) pseudocubic reflections of the ISTO films and those corresponding to the substrates are visible in the θ-2θ XRD scan curves (**Figure 41**(a)), indicating that the films are highly oriented along the *c*-axis. No secondary phase or diffraction peaks from randomly oriented grains were observed. Enlarged θ-2θ scans around the LAO (002) reflection (**Figure 41**(b)) show that the diffraction peak of ISTO (002) shifts to a lower angle when the In concentration *x* in the films increases from 0 to 0.15, indicating the influence of doping on the lattice parameters of the ISTO unit cell (discussed later in detail).

The typical Φ-scan measurements of the films (*x*=0.01, 0.10, 0.15) around the (110) reflection of LAO are illustrated in **Figure 41**(c)–(h) which evidence the four-fold symmetry of the epitaxial relationship between the films and the substrates, as well as indicate the particular orientation of single-crystalline thin films with (110) diffraction signal. The in-plane

(IP) and out-of-plane (OP) lattice parameters of ISTO thin films were determined by RSM measurements. **Figure 42**(a) depicts the typical contour diagrams (IP and OP lattice parameters) of ISTO film (x=0.1) around the (203) reflection. The ISTO film (x=0.1) has a distorted structure with IP and OP lattice constants of 3.887 and 3.985 Å respectively, as determined from the Q_x and Q_z values ($a=\lambda/Q_x$ and $c=3\lambda/2Q_z$). The large distributions of intensity for the LAO substrate which indicate a large spread of crystal plane orientations result in the large distributions of intensity for epitaxial ISTO films, shown in **Figure 42**(a).

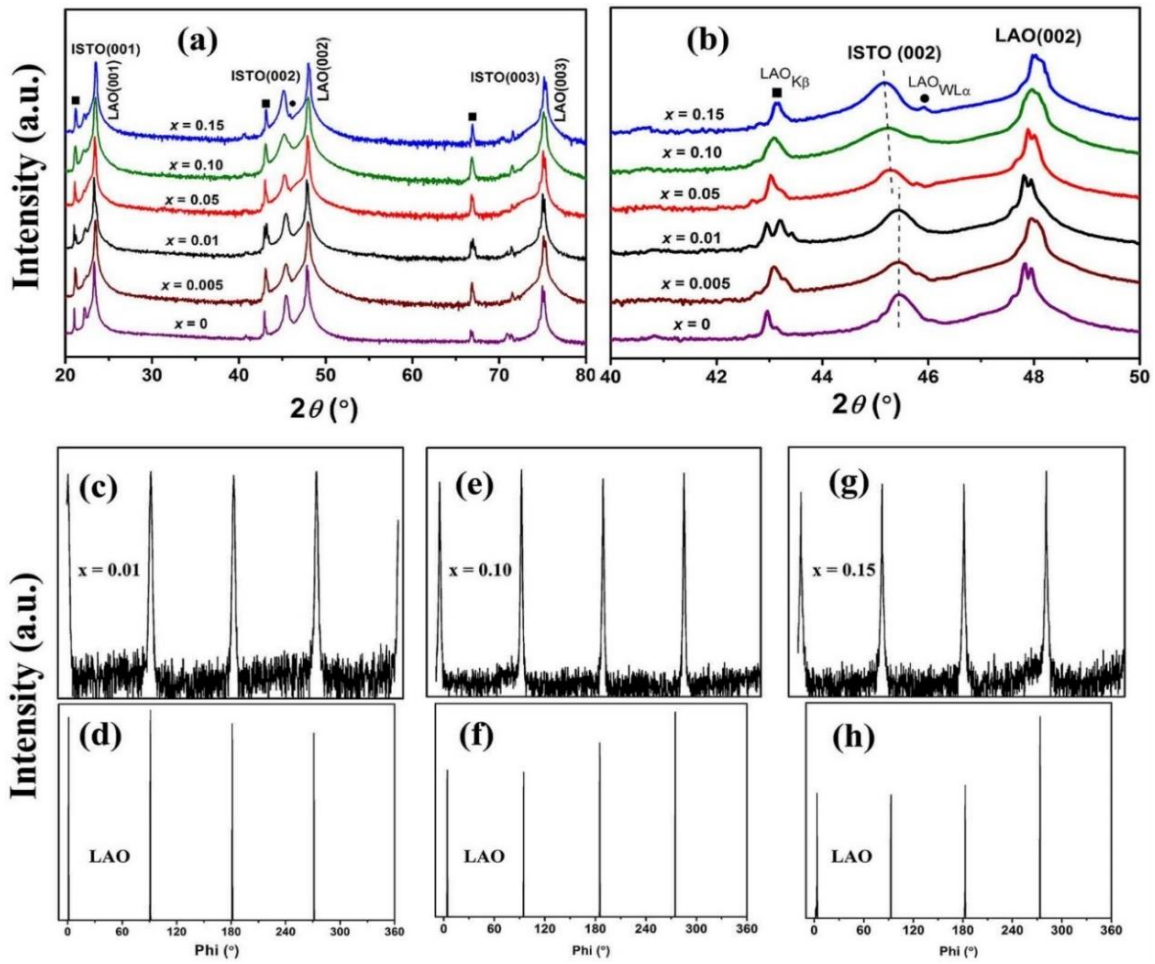

Figure 41. (a) XRD profiles of the ISTO films (x=0–0.15) grown on LAO (100) substrate; (b) XRD profiles of the ISTO films (x=0–0.15) with 2θ between 40–50˚; (c) (e) (g) Φ-scan profiles

around the (110) plane of ISTO films (x=0.01, 0.1, 0.15); (d) (f) (h) Φ-scan profiles around the (110) plane of LAO (100) substrate.

The evolution of the IP lattice parameters as a function of In concentration is shown in **Figure 42**(b). As expected, the increase of In substitution when x increases from 0 to 0.15 results in an expansion of the IP lattice parameter. The lattice constants of ISTO (x=0–0.15) thin films are slightly larger than that of the STO single crystal (3.905 Å) and depend on the In concentration. The evolution of the OP lattice parameters of ISTO as a function of x is shown in **Figure 42**(b), deduced from the θ-2θ scan of XRD (**Figure 42**(b)) according to Bragg's law and the lattice spacing in a cubic system. This evolution does not correspond to Vegard's law [130], which stipulates a linear relation between the crystal lattice constant of an alloy and the concentrations of the constituent elements at a constant temperature. The lattice parameter first decreases when x increases from 0 to 0.01, and then dramatically increases for x varying from 0.01 to 0.05. It remains stable for x between 0.05 and 0.15. The OP parameter increases with increases of x at regime of x>0.01. This trend can be explained as follows: the partial substitution of In for Ti causes a lattice dilation because of the larger effective radius of In^{3+} (~0.94 Å) regarding that of Ti^{4+} (~0.74 Å), as well as the ionic In–O bond which is weaker than the covalent Ti–O bond. The OP lattice parameters keep a stable value at ~4 Å when x increases from 0.05 to 0.15, due to the effect of residual OP strain induced by the lattice mismatch between the film and LAO substrate. The OP parameter decreases with increases of x at low In concentration regime (x≤0.01). Hypothetically, the In atoms enhance dislocations and thus

induce the relaxation of the OP lattice parameter towards its bulk value (~3.905 Å). This effect conflicts with the lattice dilatation induced by the Ti substitution.

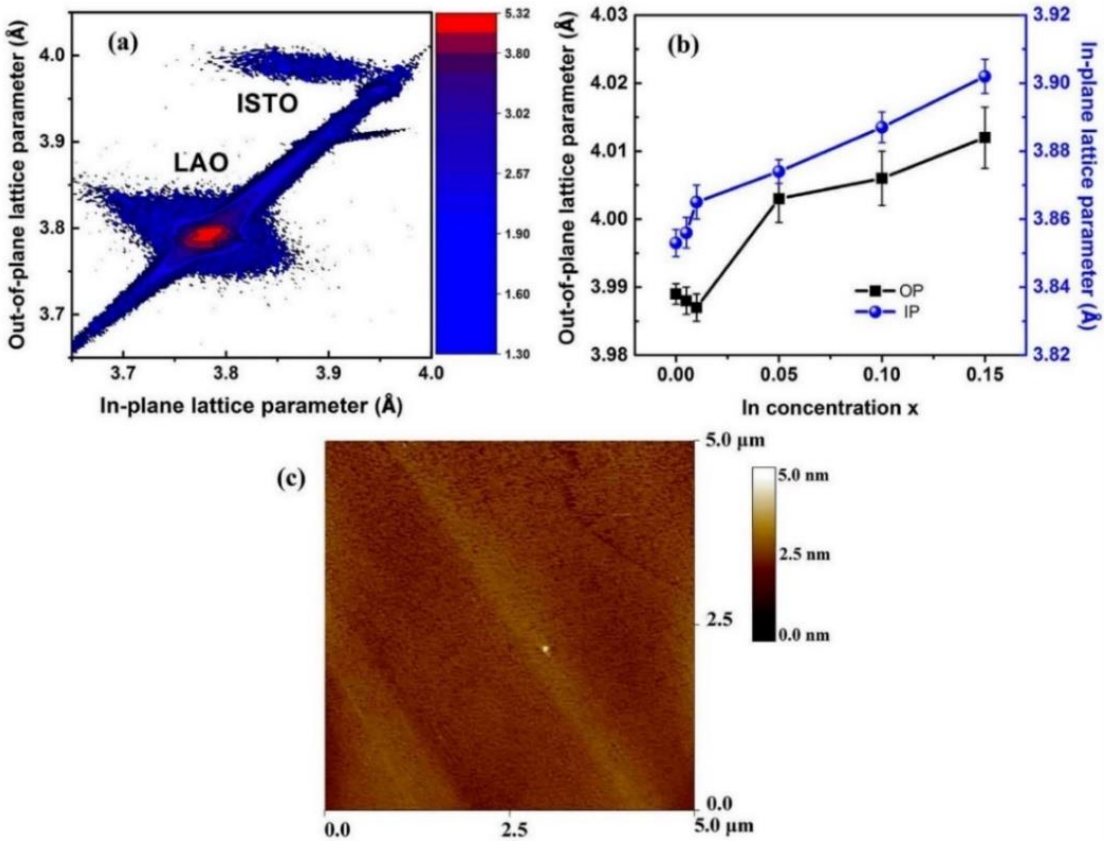

Figure 42. (a) RSM profiles around (203) reflection of the ISTO film (x=0.1) grown on LAO (100) substrate; (b) OP and IP lattice parameters vs. In concentration x for ISTO films (x=0–0.15); (c) AFM images from the ISTO film (x=0.15) and the root-mean-square roughness is measured to be ~0.57 nm over the area 5×5 μm^2.

The AFM measurements performed on the ISTO film (x=0.15) (**Figure 42**(c)) allowed us to determine the root mean square roughness over an area of 5×5 μm^2 as ~0.57 nm, indicating a relatively smooth surface throughout the film. High crystallinity and atomically smooth surfaces are both critical for the fabrication of epitaxial heterostructure.

4.3. Electrical properties

The electrical resistance of the ISTO films was measured using the four point probe method at RT. Pristine STO films (ISTO when x=0) are insulating. As illustrated in **Figure 43**(a), the resistivity of ISTO films decreases dramatically when x increases from 0.005 to 0.1, and then decreases slowly when x raises from 0.1 to 0.15. The quasi-stabilized resistivity is ~10^{-2} Ω cm when $x \geq 0.1$.

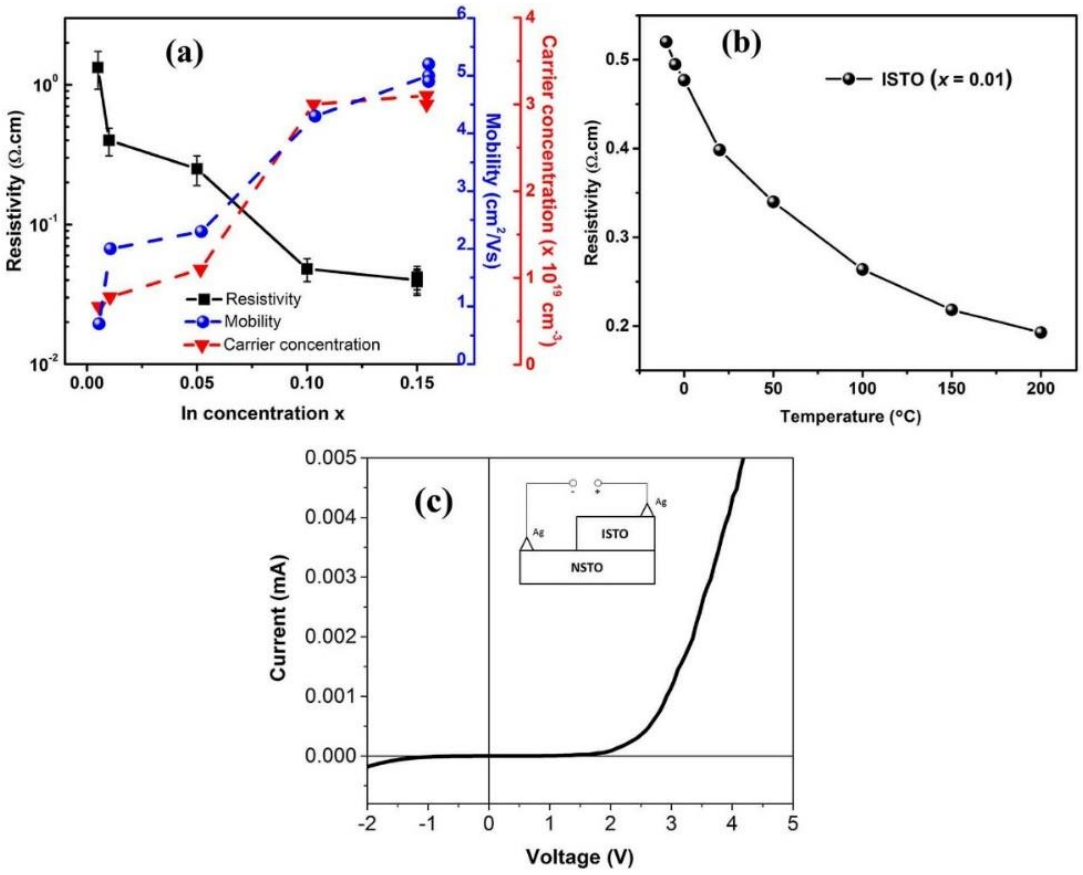

Figure 43. (a) Resistivity, carrier concentration and mobility vs. In concentration x for the ISTO films (x=0.005–0.15) at RT; (b) Resistivity vs. variant temperatures (-10 to 200˚C) for the ISTO film (x=0.01) and (c) Current vs. voltage characteristic measured at RT for a junction composed of $SrIn_{0.15}Ti_{0.85}O_3$ // $SrNb_{0.05}Ti_{0.95}O_3$.

The dependence of the resistivity on *x* is characterized by two distinct behaviours with a transition around *x*=0.1. As shown in **Figure 43**(a), the gradients of the electrical resistivity with respect to doped In concentration are as following:

$$\frac{d}{dx}\log\rho = \begin{cases} 12\ \Omega.\mathrm{cm} & (x \leq 0.05) \\ 1.6\ \Omega.\mathrm{cm} & (x \geq 0.10) \end{cases} \quad (2)$$

The large difference between these gradients indicates that the mechanisms underlying the increase in resistivity are different from the region (0.05<*x*<0.10) to the other one.

Table 6. Resistivity (ρ), carrier concentration (n) and mobility (μ) for ISTO films with various In concentration *x*=0.005, 0.01, 0.05, 0.1, 0.15 at RT.

Samples	*x*	ρ (Ω cm)	n ($\times 10^{19}$ cm^{-3})	μ (cm^2/Vs)
S2	0.005	1.330	0.67	0.7
S3	0.01	0.400	0.78	2.0
S4	0.05	0.250	1.10	2.3
S5	0.10	0.048	3.00	4.3
S6	0.15	0.040	3.10	5.0
S7	0.15	0.039	3.10	5.2
S8	0.15	0.042	3.00	4.9

Hall Effect measurements confirm that the ISTO films (*x*=0.005–0.15) are *p*-type semiconductors with the positive Hall coefficient (R_H) in the range 0.20–0.93 cm^3 C^{-1}. As shown in **Table 6**, the carrier concentration was determined to be 0.67–3.1×10^{19} cm^{-3} and the mobility in the range 0.7–5.2 cm^2/Vs, with *x* between 0.005 and 0.15, which is close to the carrier concentration of 1.4–3.9×10^{19} cm^{-3} and mobility of 0.28–9.0 cm^2/Vs as reported for ISTO grown on $NdGaO_3$ [131]. As shown in **Figure 43**(a), the increase in mobility is mainly responsible for the observed reduction in film resistivity with increasing In concentration. The temperature dependence of the electrical resistivity of the films was also investigated between

-10 and 200 ˚C. The resistivity decreases with increasing temperature, suggesting a typical semiconducting electrical behavior. We present the ISTO film (x=0.01) in **Figure 43**(b) as an example. The resistivity of ISTO films (x=0.15) grown under oxygen pressures ranging from 10^{-7} to 10^{-3} Torr was investigated (**Table 6**) for estimating the effect of oxygen vacancy on the resistivity. The results demonstrate that the resistivity remains quasi-stable (~4×10^{-2} Ω cm) with increasing oxygen pressure. Thus, it demonstrates that the presence of oxygen vacancies does not improve the electrical conduction of films. The addition of doped In^{3+} into the STO lattice creates a defect with an effective negative charge relative to the STO lattice. The charge neutralization can take place by introducing oxygen vacancies in the lattice and generally does not lead to improved electronic conductivity, since there is no transfer of charges or electrons into the lattice due to the partial or total localization of the electrons in the cavity. We found quantitatively similar resistivity measured at RT for ISTO films (x=0.15) grown under different oxygen background pressures, thus introducing quantitatively different oxygen vacancies. This is in agreement with previous computational and experimental results, i.e. the electrons from oxygen vacancies are often localized and do not contribute significantly to the electronic conductivity of the *p*-type doping semiconductor. The junction was obtained by growing the 100 nm-thick film of $SrIn_{0.15}Ti_{0.85}O_3$ on single-crystalline $SrNb_{0.05}Ti_{0.95}O_3$ substrate. **Figure 43**(c) shows the current-voltage characteristic measured at RT. It behaves as a diode at RT. The diffusion potential is about 2.67 V.

4.4. Optical properties

The optical transmission spectra of various doped ISTO thin films with thickness of ~100 nm over the whole UV-visible range are shown in **Figure 44**(a). The figure clearly displays the transparent nature of films S1–S8 with In doping concentration of 0–15% and single crystal STO as comparison. The figure clearly displays the transparent nature of films S1–S8 with In doping concentration of 0–15% which were compared to a single crystal undoped STO. The films grown at 10^{-7} Torr are highly transparent with transmittance slightly increased from 70% to 75% when In content increases from 0 to 15% in most of the visible spectrum. The films (x=0.15) grown at 10^{-7}, 10^{-5} and 10^{-3} Torr display a very close transparency of ~75%. The single crystal STO shows a higher transparency over 80% than the other films. Since the optical transition is directly related to the band gap of the material, we estimated the optical band gap through transmission measurements for all films shown in **Figure 44**(b)–(c). The optical transition of STO could be described by indirect band gap calculations. The indirect optical transitions of STO films presented by $(\alpha E)^{1/2}$ vs. photon energy plots are shown in **Figure 44**(b)–(c). The optical band gap E_g can be determined from the absorption coefficient α, calculated according to Tauc's formula [132] as following **equation (3)**:

$$\alpha E = A(E - E_g)^n \quad , \qquad (3)$$

where E is the photon energy, A is a function of the refractive index and hole/electron effective masses, n is equal to 1/2 or 2 for direct or indirect gap materials, respectively. Here, the absorption coefficient α of thin films can be obtained by **equation (4)** [133]:

$$\alpha = -\frac{\ln(T)}{d} \quad , \qquad (4)$$

where *T* and *d* are the transmittance and thickness of the films, respectively. The bandgap value was estimated by the linear extrapolation approach. **Figure 44**(b)–(c) show the calculated indirect bandgap values of ISTO films (x=0–0.15) at various values of In concentration and single crystal STO.

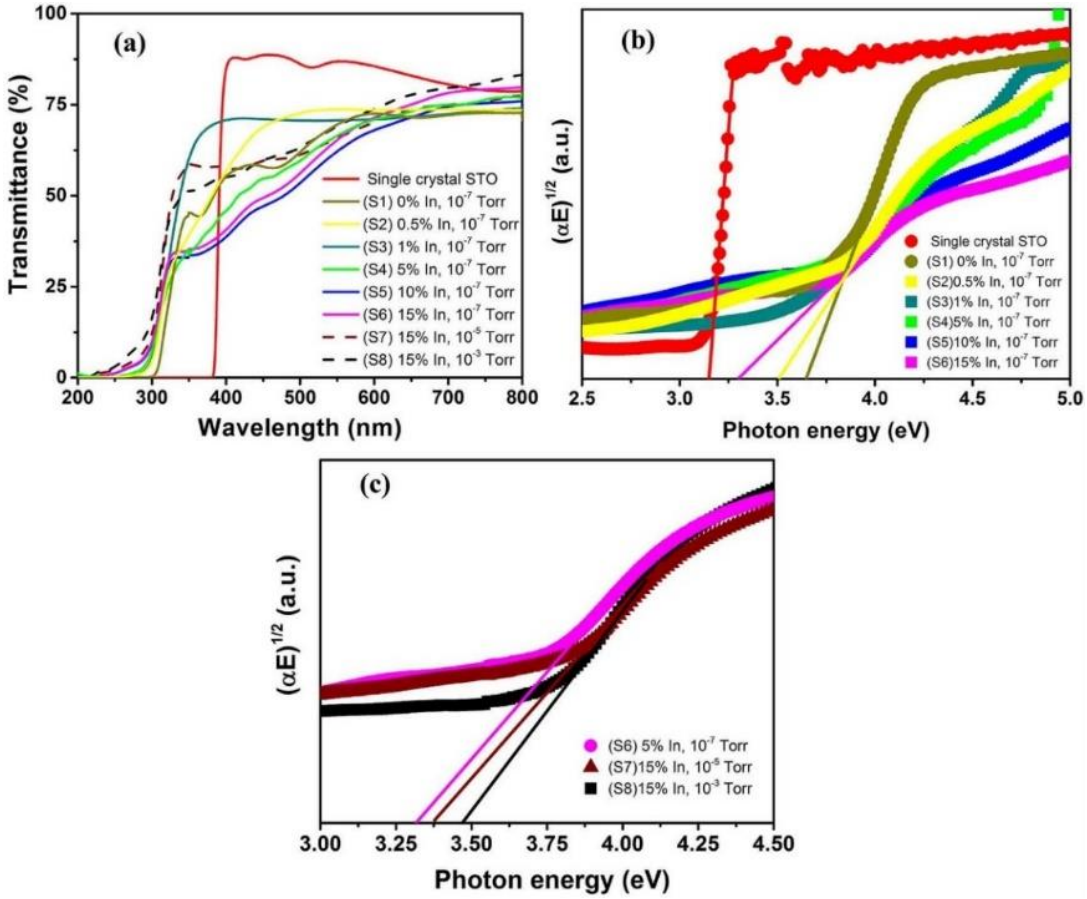

Figure 44. (a) Optical transmission spectra of ISTO films S1-S8 (x=0–0.15) and single crystal STO. (b) Indirect optical transitions of ISTO films S1-S6 (x=0–0.15) and single crystal STO. (c) Indirect optical transitions of ISTO films S6-S8 (x=0.15) grown under oxygen pressures ranging from 10^{-7} to 10^{-3} Torr.

Single crystal STO has a band gap of ~3.20 eV (λ=388 nm) (**Figure 44**(b)) which is defined as the separation of the filled oxygen 2*p* bands from the empty titanium t_{2g} bands [134].

It is quite smaller than the optical band gap of ~3.66 eV for ISTO film S1 (x=0), due to the effect of substrate-induced strain on the optical band gap in STO films grown on LAO. The indirect absorption edge of ISTO films S2–S8 around 3.53–3.32 eV is smaller than that in ISTO film S1 (x=0) (**Figure 44**(b)). This can be explained by the fact that the partial substitution of In^{3+} for Ti^{4+} might change the energy state of Ti–O bonds and inducing the strong hybridization of the Ti 3*d* and the O 2*p* orbitals, thereby resulting in modification of the width of the valence band [129]. **Figure 44**(c) shows that the absorption edge for ISTO films (x=0.15) grown under oxygen pressure of 10^{-7} (S6), 10^{-5} (S7) and 10^{-3} Torr (S8) shifts towards shorter wavelengths (blue shifts). The indirect band gap of ISTO films (x=0.15) increases by increasing the oxygen pressure. These results indicate the effect of the oxygen content on the optical properties of ISTO films. As the oxygen vacancies increase under lower oxygen pressure deposition conditions, an additional bonding-exciton-energy level will form at the bottom of the conduction band and cause a narrowing of the energy gap [135].

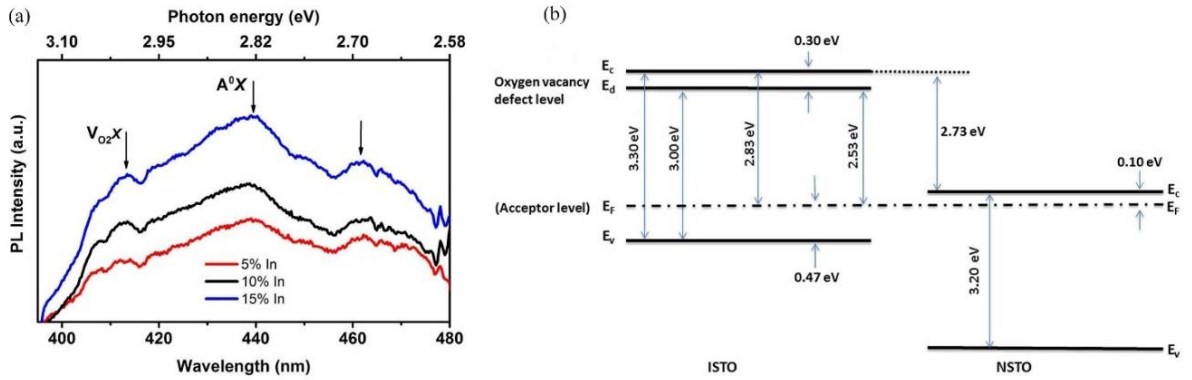

Figure 45. (a) PL spectra for ISTO films (x=0.05, 0.10, 0.15) measured at RT. (b) Energy band diagram of an ideal ISTO (x=0.15)/NSTO *p-n* junction at thermal equilibrium.

Photoluminescence (PL) measurements were performed to confirm the impurity level and the role of oxygen vacancies in forming the defect band. **Figure 45**(a) depicts the PL spectrum of ISTO films (x=0.05, 0.10 and 0.15) measured at RT. The strongest peaks at ~440 nm (2.8 eV), in order of intensity, is an acceptor-bound exciton (A^0X). This acceptor level slightly shifts toward to lower energy with decreasing doping level, agreeing with our previous explanation about the effect of In doping level on the modification of width of valence band. The acceptor level was created at the top of the valence band with the derived optical band gap (~3.3 eV for ISTO: x=0.15), and is very close to the Fermi level in *p*-type semiconductor, schematically shown in **Figure 45**(b) (left). The PL peak at ~413 nm (3.0 eV) is unambiguously an oxygen vacancy defect-bound exciton ($V_{O2}X$) which is close to 420 nm (2.9 eV) as reported for La-doped STO grown at 10^{-3} Torr, created at the bottom of the conduction band [136]. The oxygen vacancy defect level keeps constant with the increasing In doping level and the same oxygen pressure of 10^{-7} Torr. The peak at ~465 nm (2.6 eV) is thought to be a recombination of the electrons and the holes in self-trapped excited state, shown the difference between oxygen vacancy defect band and acceptor band in **Figure 45**(b) (left). **Figure 45**(b) summarizes the staggered energy band diagram of an ideal ISTO (x=0.15)/NSTO *p*-*n* heterojunction at thermal equilibrium. The NSTO is an *n*-type semiconductor with an energy band gap of 3.2 eV and a Fermi level below ~0.1 eV at the bottom of conduction band, shown in **Figure 45**(b) (right). As showed in **Figure 45**(b), the barrier height seen by electrons is ~2.73 eV. Therefore, the ideal turn-on voltage is 2.73 V, this is in good agreement with the value obtained from the I-V curve (see **Figure 43**(c)).

4.5. Summary

In summary, ISTO thin films (with In concentration in the range $0 \leq x \leq 0.15$) were grown epitaxially on LAO (100) single crystals using a PLD and MBE combination system. The films exhibit a single phase, high crystal quality and atomically smooth surface. The ISTO films with In concentration in the range of 10 to 15% grown under oxygen background pressures between 10^{-7} and 10^{-3} Torr show an optimal range of high transmittance (>70%) and low resistivity (10^{-2} Ω cm) with a high carrier concentration of 3×10^{19} cm^{-3} and carrier mobility of 5 cm^2/Vs. They also have large optical band gap energies of >3.2 eV.

SECTION II Bi_2FeCrO_6 for Solar Energy Conversion Applications

Chapter 5. Switchable photodiodes based on epitaxial Bi_2FeCrO_6 multiferroic thin films

Recently, multiferroic BFCO has been extensively studied for photovoltaic (PV) applications due to its relatively low bandgap (1.4−2.4 eV, tuned by controlling the degree of Fe/Cr cationic order in BFCO single-phase), huge visible-light absorption coefficient (~2.0×10^5 cm^{-1}) and effective carriers' separation driven by the large remnant ferroelectric polarization (~55 μC cm^{-2}) [59, 65, 113]. Nechache *et al.*[64] reported the BFCO thin-film based solar cells and achieved an efficiency of ~3.3% in single-layer devices and ~8.1% in triple-layer heterostructures devices under AM 1.5G illumination. Moreover, the multiferroic properties also offer a potential opportunity for use in optoelectronic devices, including photodetectors, such as photodiodes, photomultipliers. Among these applications, photodiodes are widely used in integrated circuitry (for control and switching, or digital signal processing); consumer electronics devices; optical communications, and light regulation,[104] due to its less complicated and low cost fabrication. It was previously demonstrated that the photodiode devices on photoconductive mode exhibit a higher sheet resistance than that of its external loads and lower photocurrent density usually under reverse bias condition [103, 105]. Moreover, the multiferroic nature of BFCO allows one to tune the photoelectric effect using magnetic fields or electric poling, endowing additional degrees of freedom for next generation optoelectronic devices.

In this chapter, we report a switchable photodiode based on multiferroic BFCO epitaxial thin films with a relatively wide bandgap of ~2.5 eV, sandwiched between a conducting perovskite bottom electrode SRO and an ITO transparent top electrode fabricated by PLD, which effectively improved carrier collection and transportation efficiency with a fast transient response of the order of 10 ms, leading to an ultrafast charge transfer (lifetime <10 ns) and a maximum responsivity of 0.38 mA/W.

5.1. Experimental section

BFCO films in 100 nm thickness were epitaxially grown on (100)-oriented single-crystalline STO substrates buffered with a 15 nm-thick SRO layer as bottom electrode by PLD. Stoichiometric BFCO and SRO targets were ablated using an energy density of about 1.8 J cm^{-2} at a repetition rate of 10 Hz. The deposition temperature and oxygen partial pressure were 580 °C and 6 mTorr, respectively.

To complete the device fabrication, 100 nm-thick ITO top electrodes were deposited on the BFCO films by PLD using the same parameters through a shadow mask with circular apertures (0.5−1 mm in diameter). To study the optical properties of BFCO thin films alone, we have investigated the optical absorbance of BFCO films, which were epitaxially directly grown on transparent (100)-oriented STO substrates by PLD using the same growth parameters as previous BFCO.

5.2. Characterization of BFCO thin films

Figure 46(a) displays the XRD pattern of the BFCO film. The (0 0 *l*) (*l*=1, 2, 3) peaks confirm the *c*-axis orientation of the film with the absence of any secondary phase. The (0 0 *l*) reflections of

the 15 nm-thick SRO layer are not visible since they are located at angles very close to those of the BFCO (0 0 *l*) reflections, and thus are buried within the (0 0 *l*) reflections of the upper layer. The Φ-scan measurements demonstrate the fourfold symmetry and the relative positions of the BFCO and STO peaks indicate a "cube-on-cube" epitaxy of BFCO on the SRO/STO (**Figure 46**(b)).

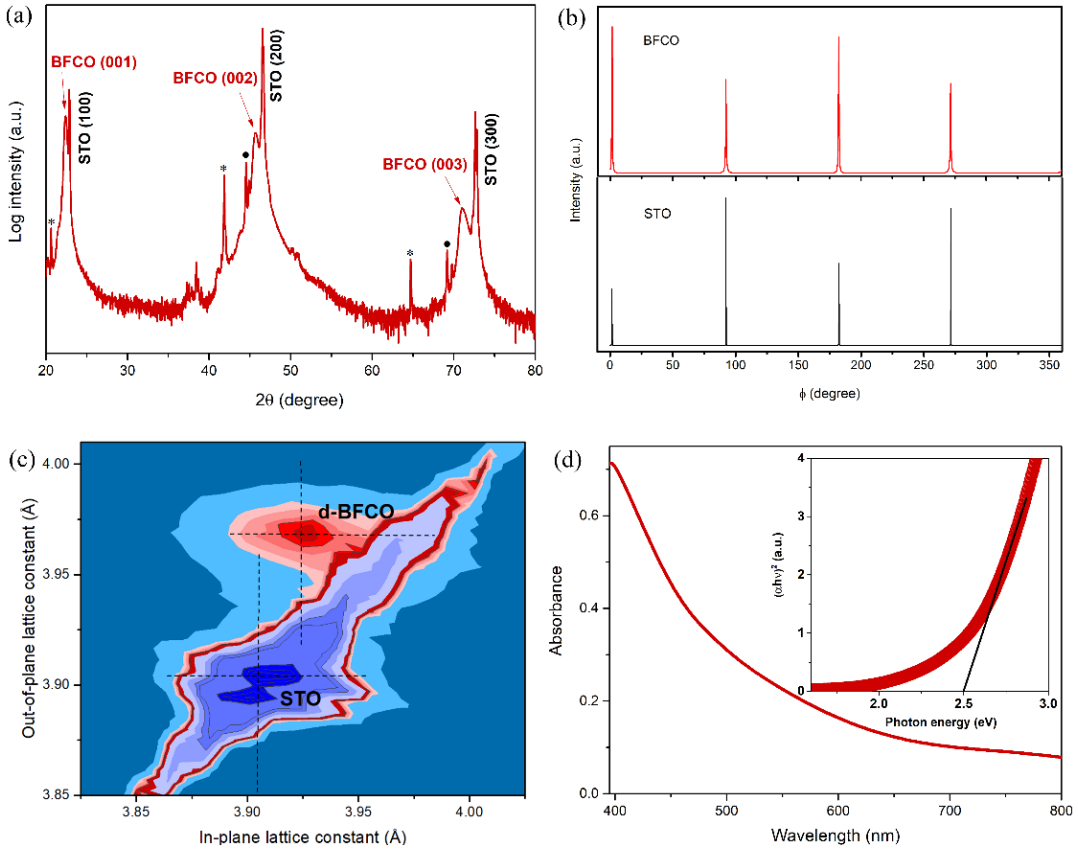

Figure 46. (a) θ-2θ scan of a BFCO thin film grown on STO (001) substrate. (b) Φ-scan profiles around the (110) plane of BFCO thin film and STO (100) substrate. (c) RSM measurement of BFCO thin film on STO, around the (204) reflection of STO showing the spot related the disordered (d-) BFCO phase in film. (d) Optical absorbance spectrum of BFCO/STO. Inset shows corresponding direct optical transitions in visible range.

XRD reciprocal space mapping (RSM) of BFCO thin films around the STO (204) reflection is illustrated in **Figure 46**(c). The small condensed reciprocal area suggests a high quality epitaxial growth of the BFCO thin film on STO substrate. The presence of extra spot indicates the existence of BFCO phase in the films, which we denote as disordered (d-BFCO) phase. The positions of the BFCO peaks are located close to that of STO along the in-plane lattice constant axis, suggesting that the film and substrate have a similar in plane lattice parameter which is ~3.925 Å, induced a smaller compressive strain (misfit=(–) 0.5%) compared to the value of out-of-plane lattice mismatch ((–) 1.6%). The optical absorbance spectrum in visible range is shown in **Figure 46**(d). The inset presents the Tauc plots of $(\alpha h\nu)^2$ vs. $h\nu$. Using the linear extrapolation of the Tauc plots to zero, the calculated direct E_g of the disordered BFCO is derived as ~2.5 eV. This value is close to the reported previously E_g (~2.4 eV for disordered BFCO single-phase) [64].

5.3. Current (*J*)-Electric field (E) analysis

The typical *J*(E) characteristics of devices were measured both in the dark and under illumination using AM 1.5G irradiation. The schematic layout of the measured devices involved in the representation of FeO_6/CrO_6 arrangements of the double perovskite BFCO crystal is illustrated in **Figure 47**(a). The light power density was varied from 50 to 100 *m*W/cm^2.

We found a substantial nonlinear dependence of the current density *J* as a function of the applied electric field E, strongly depending on the direction of E, as shown in **Figure 47**(b). The conductivity rapidly increases with light intensity when increased from 50 to 100 *m*W/cm^2, at any field applied. This can be explained by the photoexcitation since the energy above the E_g of BFCO. The electrons being excited from the valence band to conduction band are transferred to the adjacent interfaces by the electrodes.

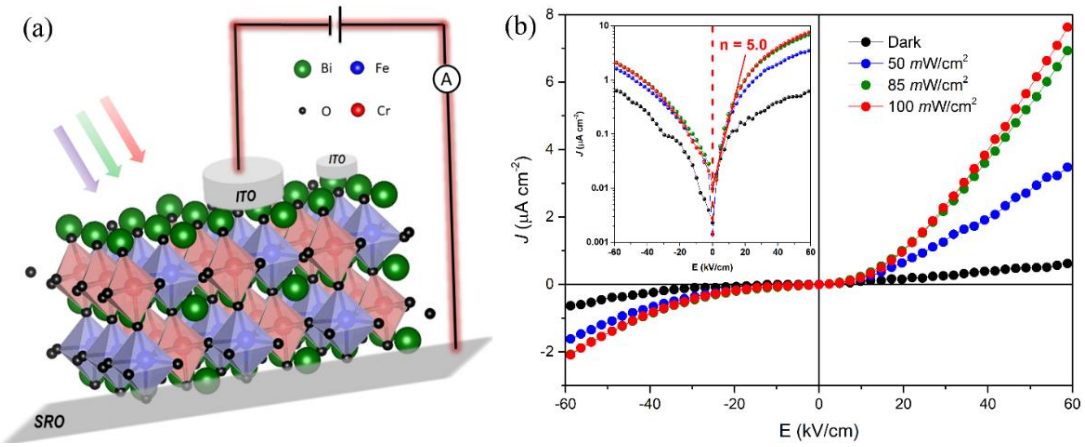

Figure 47. (a) Layout of ITO/BFCO/SRO heterostructures devices and the representation of FeO_6/CrO_6 arrangements of the double-perovskite BFCO crystal. (b) Variation in $J(E)$ device characteristics under illumination with intensity varying from 50 to 100 mW/cm^2. Inset shows the same curves as semi-log-plots.

The J(E) curves of devices at RT (~300 k) exhibit diode-like behavior. The reverse saturation current density is about 0.22 μA cm^{-2} at −22.05 kV/cm measured under one sun illumination. For the p–n ideal diode, the forward current density follows an exponential relationship with applied voltage given by following **equation (5)** [137]:

$$J = J_0 \left[\left(\exp(^{qV}/_{nk_BT})\right) - 1\right], \qquad (5)$$

where J_0 is the reverse saturation current density, q is the electron charge, V is the applied voltage, n is a constant called the ideality factor, k_B is the Boltzmann constant and T is absolute temperature. For our device, we found an ideality factor of n ~5.0 at 300 K and a forward bias field of 9.80 kV/cm, as shown in the inset of **Figure 47**(b). This ideality factor is much larger than the ideal value of 1 in semiconductor p-n junctions, where charge trapping at defects in the bulk seems important for transport properties. This value is close to the reported n (~ 4.7 at 350 K and ~ 6.3 at 300 K) for the switchable multiferroic BFO-based diode [137].

5.4. *J*(E) characteristics with FE polarization switching

FE polarization is crucially important for tuning the internal depolarization electric field and obtaining optimal surface band structures to enhance the photoconductive performance. The presence of ferroelectricity in the BFCO films on SRO/STO at the grain level is demonstrated by PFM. The sketch of the setup for PFM is illustrated in **Figure 48**(a).

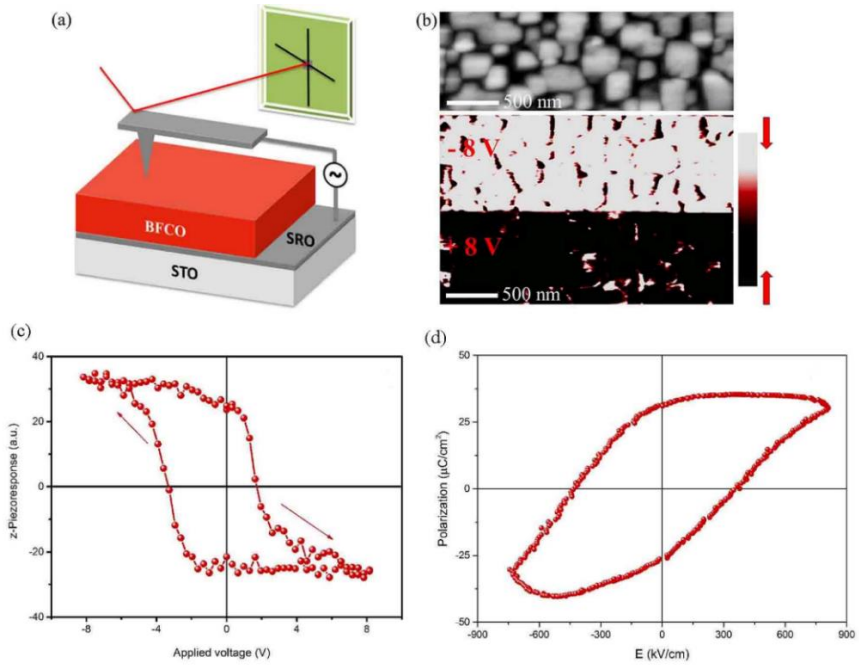

Figure 48. (a) Sketch of the setup for PFM measurement. (b) AFM Topography and PFM images after applied ±8 V pulses. (c) Local FE hysteresis loop for BFCO thin film. (d) Macro FE polarization measurement of devices at 2 kHz frequency at RT.

Figure 48(b) shows the surface topography of 100 nm-thick BFCO films performed by AFM implemented with the same PFM instrument, and we determined the root mean square (RMS) roughness of ~8 nm, indicating a relatively smooth surface throughout the film of BFCO. The FE domains of BFCO can be individually or partially switched by applying ±8 V DC voltage pulses. These images in **Figure 48**(b) show that applying +8 V bias induces a homogeneous state with

upward (pointing out of the surface) out-of-plane polarization, while –8 V bias induces a homogeneous state with downward polarization (towards the SRO bottom electrode). The resulting contrast is a clear proof that ferroelectricity in PLD deposited BFCO occurs and can be switched upon the application of an external voltage. This is an indication of the possibility to design a switchable photodiode device by controlling the electric polarization in the multiferroic BFCO. Further proof of ferroelectricity is the presence of hysteresis loops (as shown in **Figure 48**(c)). The FE behavior of our BFCO film based devices was further confirmed by macroscopic measurements (**Figure 48**(d)). The polarization of BFCO thin film with $E_g \approx 2.5$ eV is 40 μC cm^{-2}, very close to the reported value [64].

To investigate the role of polarization on the photo-electric behavior in multiferroic BFCO films, we repeated the $J(E)$ measurement after the BFCO film was polarized by different high voltage pulses under illumination (100 mW/cm^2). Henceforth, we define the positively polarized state as the state when spontaneous polarization in the sample is downward (state achieved by positive voltage pulses on the top electrode), and the negatively polarized state that achieved by negative pulses. The magnitude of the voltage pulses applied was 15 V. The effect of polarization on the J(E) curves of the device is shown in **Figure 49**(a).

Firstly, we find a short-circuit photocurrent density (J_{sc}) enhancement by two orders of magnitude compared with that of the virgin state (without poling) in **Figure 49**(a). In the positive state $J_{sc} \approx +2$ μA cm^{-2} while $J_{sc} \approx -4$ μA cm^{-2} after the film is poled with a –15 V pulse, which is enhanced by hundreds-fold at virgin state under illumination. This indicates the devices undergoing electric poling under illumination showing the PV behavior. Secondly, we find that the shape of the $J(E)$ curves are drastically changed, becoming almost symmetrical with respect to

the origin: $J(E)|_{P_{up}} \approx -J(-E)|_{P_{down}}$, which suggests that the band alignments in the device are reversed at the two interfaces with polarization switching.

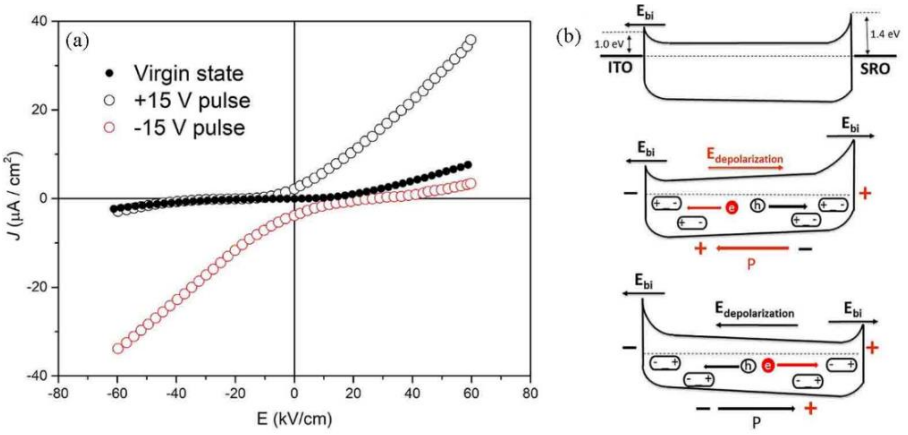

Figure 49. (a) *J*(E) curves for BFCO at virgin state and underwent ±15 V electric poling under illumination (100 *m*W/cm^2). (b) Schematic of simplified energy band alignments for heteroepitaxial structures for an ideal metal–semiconductor interface without polarization (top of panel: virgin state), and positively/negatively poled at ±15 V (middle and bottom of panel, respectively).

To understand the mechanism of FE polarization-dependent charge separation and transfer behavior in our ITO/BFCO/SRO heterostructures, we investigated the energy band structure for each component material and constructed the estimated energy band alignment in accordance to previously reported values [64, 113]. The work functions (ϕ) of ITO and SRO are 4.8 and 5.2 eV, respectively,[64] while the electron affinity (χ) and ϕ for BFCO, determined from the UPS measurements, are about −3.8 and −5.0 eV. In **Figure 49**(b), these values are used to construct the energy band structure of BFCO with a conduction band of ~3.8 eV and a valence band of ~6.3 eV below the vacuum level. For our ITO/BFCO/SRO heteroepitaxial structure without external voltages applied, at the SRO/BFCO interface under thermal equilibrium, electrons pass from the

conduction band of BFCO to SRO (since $\phi_{SRO}>\phi_{BFCO}$) until the Fermi levels equalize, thus forming a depletion region in BFCO with an upward band bending (top panel of **Figure 49**(b)). This contact is a Schottky-type and is highly resistive. In contrast, the contact region formed at the interface between BFCO and ITO is Ohmic and has a low resistance, inducing a downward band bending since $\phi_{BFCO}>\phi_{ITO}$ (top panel of **Figure 49**(b)). The region of this contact does not affect the conduction behavior under an applied voltage. The middle and bottom panel of **Figure 49**(b) show the modification of energy band alignments in the presence of the FE polarization (P) for the two possible orientations. A positive voltage applied to the SRO bottom electrode results in an electric field with opposite direction to the bottom barrier field and in the same direction as the top one. When the BFCO films are poled, the energy band diagram is modified as shown in the middle panel of **Figure 49**(b) for "upward" polarization, while the modified energy band alignment for "downward" polarization is illustrated in the bottom panel of **Figure 49**(b). The origin of this modification is thought to be the modulation of the energy band induced by polarization [138]: The positively charged holes and the negatively charged electrons will move under the electric depolarization field, thus accumulate near the ITO and the SRO interfaces, respectively, when polarization is "downward" (and in opposite directions for "upward" polarization). These charge accumulations near interfaces further contribute to the shift of the energy levels, resulting in a reduction or an increase of the barrier heights. This demonstrates the possibility to design a photodiode that can be controlled/switched by electric poling.

5.5. Photoresponse and charge carrier dynamics

Figure 50(a) shows the reliable and reversible switching of the photocurrent through the device biased at 0.3 V under 1 sun illumination switched On/Off periodically. The rise (as measured from

10% to 90%) and decay (as measured from 90% to 10%) times of the current for a single pulse were estimated to be ~90 and 68 ms, as shown in top and bottom panel in **Figure 50**(b), respectively. These values are close to the reported typical fast-transient responsive ZnO NWs/*p*−Si heterojunction photodiode [105]. As mentioned before, when illuminated by energetic photons ≥2.5 eV, excitons (pairs of electron-hole) are generated. Under the internal depolarization electric field in BFCO, at the interfacial region of BFCO/SRO, the excitons split into electrons and holes, the electrons at the conduction band of the BFCO is then transferred. Due to the excellent electrical conductivity of SRO, the total series resistance of the heterojunction structure (BFCO/SRO) is reduced. This effectively enhances the electron–hole separation and improves carrier transport in the heterojunction, leading to a faster response of the device. When the light is turned off, the excess electrons from the SRO transfer into the BFCO where they recombine with the holes, which is an inherently fast process. The On/Off ratio in our devices is relatively low (~7), more than 2 orders of magnitude below the ratio reported in the typical ZnO epitaxial film-based UV detection device (over 1000) [105], a fact which we attribute to the high dark current of the device.

The transient times extracted from the electric measurements, however, do not represent the charge dynamics in the device, since the current transient depends on the measuring circuit (particularly on the bandwidth of the current preamplifier). Therefore, to gain insight and further understand the mechanism of charge transfer and carrier recombination in our BFCO/SRO heteroepitaxial structure, we performed PL measurements. They were carried out with an excitation at 383 nm, and they reveal that the films exhibit a PL emission at ~500 nm (**Figure 50**(c)). Thus the charge separation and transfer process (Inset of **Figure 50**(c)) in the BFCO/SRO junction were quantitatively determined using time resolved PL (TRPL) measurements at ~500

nm wavelength, as shown in **Figure 50**(d). It can be seen that the charge transfer process from BFCO to SRO is ultrafast, with a lifetime of ~6.4 ns, implying an effective charge separation and efficient charge transfer with a low carrier recombination rate. In fact, a value within ~10 ns indicates that the charge carrier dynamics in our heteroepitaxial structure is faster than the typical values reported for FE oxides based photodetector [80].

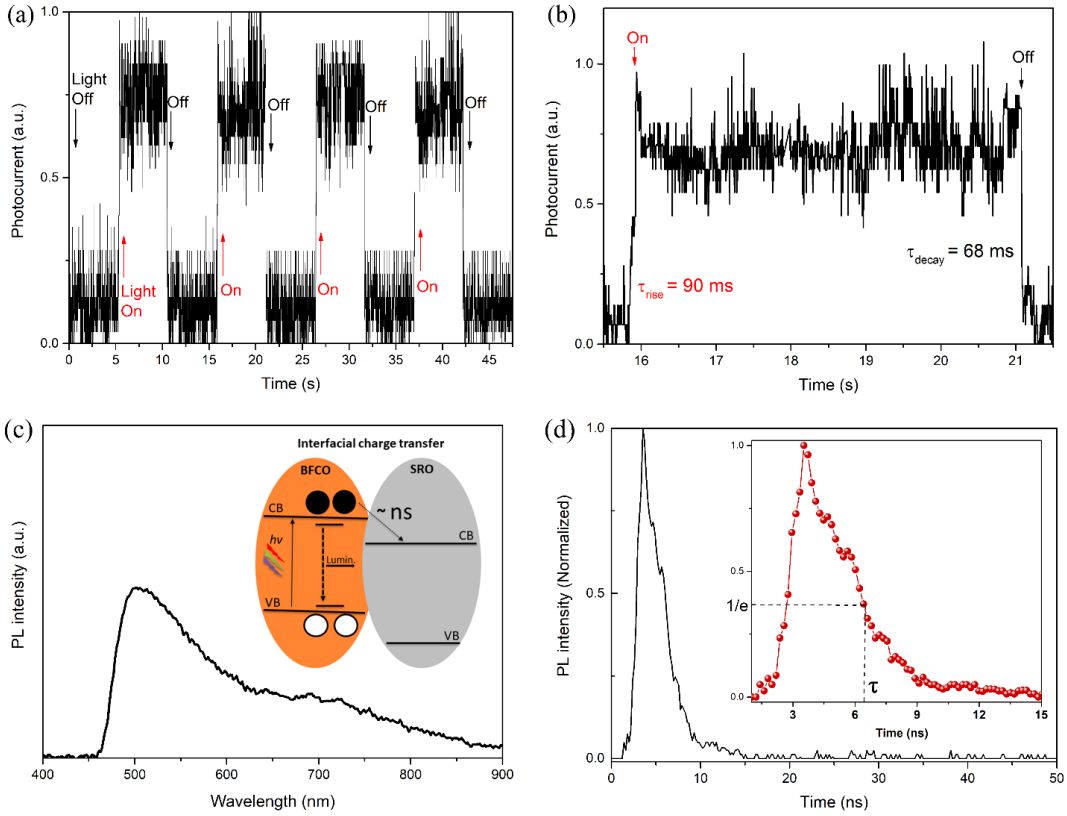

Figure 50. (a) Reversible switching of electrical current at 0.3 V under illumination for photodiodes. (b) The rise (top of panel) and decay (bottom of panel) of the current in time for a single pulse in (a). (c) PL spectra of the heteroepitaxial structures under an excitation of 383 nm; Inset shows the schematic illustration of charge transfer at interfacial region of BFCO/SRO. (d) TRPL decay measured at 500 nm for the heteroepitaxial structures. Inset shows a magnified region of the TRPL spectra between 2–15 ns.

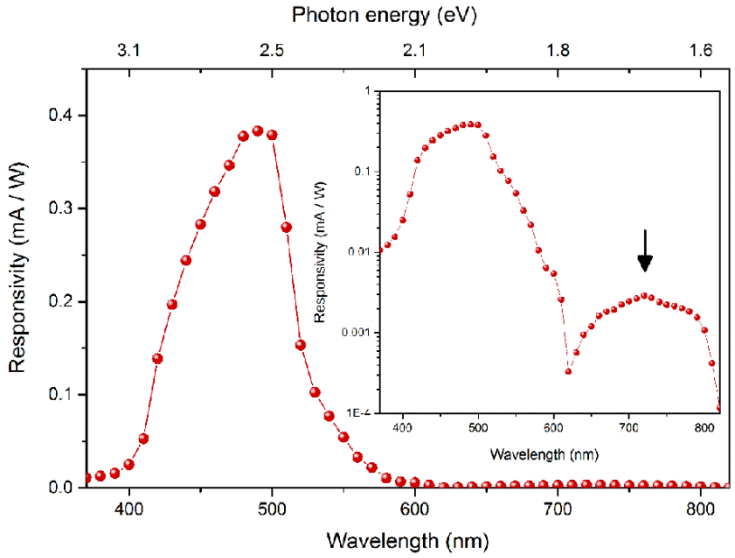

Figure 51. Photoresponsivity spectra of the device at 500 nm at zero bias. Inset shows a semi-log curve of measured spectrum.

Finally, we characterized the spectral response of our photodiode devices, by measuring the responsivity from 350 nm to 850 nm. As shown in **Figure 51** clear response is achieved for wavelengths between 400 nm and 560 nm, with a drop at 500 nm. The maximum responsivity of 0.38 mA/W is located around 500 nm. The inset of **Figure 51** shows a region of the same plot in a semi-log scale, which shows that the sample has also a weak response of ~10^{-2} mA/W within a wide window of the spectrum (wavelength from 600 to 800 nm). The response in this region demonstrates a sub-band-gap features, similar to that found in multiferroic BFO film-based photodetectors [80]. As possible origin for this weak response, we suggest that it is related to oxygen vacancies. Known to be always present in perovskites films, particularly in PLD deposited one, thus in BFCO oxygen vacancies are presumed to act as donor impurities [64]. This is also confirmed by the presence of peak around ~700 nm was found in PL spectra of **Figure 50**(c), which is attributed to the defect level of oxygen vacancies.

5.6. Summary

A switchable heterojunction photodiode based on multiferroic BFCO epitaxial thin films has been demonstrated. The relatively wide bandgap (~2.5 eV) with low degree of Fe/Cr cationic ordering and switchable FE polarization properties of BFCO films were investigated in this study. The device exhibits a substantial photocurrent at +0.3 V and a fast transient response (in the order of 10 ms), attributed to the effective charge carrier separation and collection at the interfacial region between BFCO and SRO electrode. The time-resolved photoluminescence decay measured at 500 nm wavelength demonstrated an ultrafast charge transfer (lifetime <10 ns) in BFCO/SRO heteroepitaxial junction. The responsivity spectrum shows a peak sensitivity of 0.38 mA/W at 500 nm.

Chapter 6. Multiferroic Bi_2FeCrO_6 based *p-i-n* Heterojunction Photovoltaic devices

Over the past decade, many studies on multiferroic materials, particularly BFCO suggested that the optimal combination of structural, electronic, optical and FE properties is a promising strategy to obtain highly efficient solar cells. Based on our previous study on multiferroics, a low bandgap and a large FE polarization promote effective charge carrier generation and separation. BFCO epitaxial thin films with a high degree of Fe/Cr cation ordering showed a low bandgap (1.4-1.6 eV) accompanied by a weak FE polarization (~5-15 μC cm^{-2}), exhibiting therefore an intrinsic semiconducting behavior. Despite a large absorption of visible light by these films, their weak FE polarization induces an internal electric field resulting in a low separation power of photogenerated carriers and high recombination losses, thus being detrimental for device performance. These results suggest a relationship between the optical properties, ferroelectricity and crystal structure in BFCO films.

On the other hand, it is known that the photo-generated voltages in FEs can exceed their bandgaps, due to the summation of series voltages across each nanometer-scale FE domain separated by domain walls [93]. However, in photodiodes and PV devices, the open-circuit voltage (V_{oc}) is typically 0.3–0.5 V less than their bandgaps [59, 103]. The hypothesized reason for the loss in V_{oc} in these devices, aside from the driven-force nature of separation of hole-electron pair, is the presence of a dark current and Schottky barriers formed at interfaces [139].

A potential approach to improve PV performance would then be to reduce these photovoltage losses. An effective electron-blocking layer (EBL)/hole-transporting layer (HTL) could achieve this goal by hindering current leakage and the consequent counter diode formation

[140]. This involves the design of a new type of structure, specifically a *p*-*i*-*n* heterojunction, together with a proper device architecture. In this *p*-*i*-*n* junction, the multiferroic BFCO film acting as an intrinsic absorber layer is sandwiched between two *p*- and *n*-type semiconductor oxides acting as EBL/HTL and electron-transporting layer (ETL) respectively. The device is designed such that the *p*-*i* and *i*-*n* depletion regions are connected, resulting in the formation of an internal electric field across the entire BFCO layer. When this *p*-*i*-*n* structure is illuminated, a V_{oc} and a short-circuit current (I_{sc}) are generated due to the separation of photogenerated charge carriers by the internal electric field.

6.1. Experimental section

BFCO films in 120 nm thickness were epitaxially grown on (100)-oriented single-crystalline 0.5 *wt*% Nb-doped $SrTiO_3$ substrates by PLD technique. A stoichiometric BFCO target was ablated using an energy density of about 2.0 J cm^{-2} at a repetition rate in the range of 4−8 Hz. The average deposition rate was between 0.04−0.06 Å/pulse. The deposition temperature and oxygen partial pressure were 610−680 °C and 8 mTorr, respectively. All the deposition parameters of BFCO films are listed in **Table 7**.

Table 7 PLD deposition parameters of BFCO thin films.

Devices	BFCO	Temperature	Repetition rate
#1 (*i*−*n*) ITO/BFCO/NSTO	BFCO #1	610 ºC	8 Hz
#2 (*i*−*n*) ITO/BFCO/NSTO	BFCO #2	680 ºC	4 Hz
#3 (*p*−*i*−*n*) ITO/NiO/BFCO/NSTO	BFCO #3	610 ºC	8 Hz
#4 (*p*−*i*−*n*) ITO/NiO/BFCO/NSTO	BFCO #4	680 ºC	4 Hz

NiO films of about 10 nm in thickness were grown on top of the BFCO/NSTO junction by PLD. The stoichiometric NiO target was ablated afterwards, without breaking the vacuum, using the same laser set at the same energy density, at a repetition rate of 5 Hz. The deposition temperature and oxygen partial pressure were 200 °C and 10 mTorr, respectively, resulting in an average deposition rate of about 0.02 Å/pulse.

Two-dimensional arrays of transparent 100 nm-thick ITO top electrodes were deposited through a shadow mask with circular apertures (100−200 μm in diameter). Four tested samples labelled devices #1–#4 involved in the intrinsic absorbers BFCO #1−#4, respectively. Devices #1 and #2 were fabricated as *i*-*n* heterojunctions compared with devices #3 and #4 as *p*-*i*-*n* heterojunctions (see **Table 7**).

6.2. Characterizations of BFCO thin films

6.2.1. Structural characterizations

The epitaxial growth of BFCO films on perovskite NSTO substrates is expected to result in high crystalline quality with smooth interfaces. We characterized and compared the crystallographic structure and phase of BFCO films grown on NSTO under different growth conditions. As shown in **Figure 52**(a), only the (0 0 *l*) (*l*=1, 2, 3) pseudocubic reflections of BFCO film and (001)-oriented NSTO substrate are visible, confirming the *c*-axis orientation of the oxide heterostructures and a good crystallization of BFCO phases, yielding a BFCO *c*-axis lattice parameter of 3.976 Å for BFCO #1 and 3.970 Å for BFCO #2. The Fe/Cr cationic ordering in the BFCO films was evidenced by performing asymmetrical θ–2θ scans around the (111) NSTO reflections, as depicted in **Figure 52**(b). In addition to the main single perovskite (111) reflection (39.7°), periodic peaks

at 2θ = 19.5 and 61.2° were observed indicating the doubling of the BFCO unit cell due to Fe/Cr cationic ordering along this crystal direction, as predicted by theoretical calculations [141].

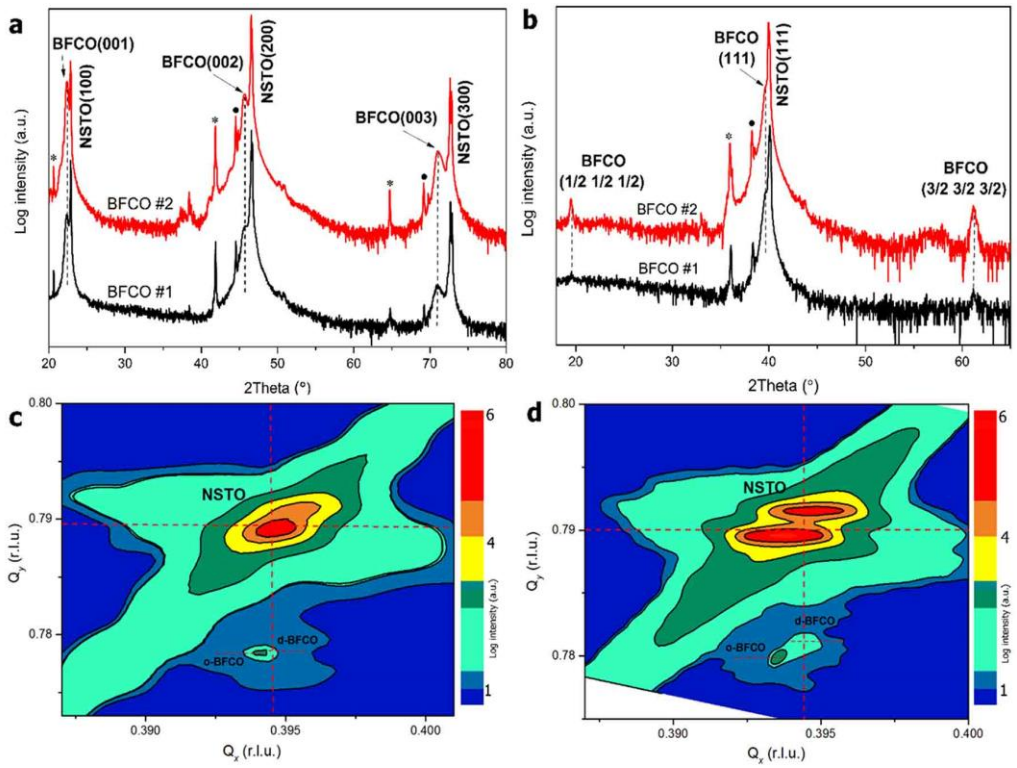

Figure 52. (a) θ-2θ scan of BFCO films grown on NSTO (001) substrate; (b) (111) asymmetrical scan for BFCO #1 and #2. The BFCO (1/2 1/2 1/2) reflection demonstrating Fe/Cr cationic ordering in the films; (c)(d) RSM measurements of BFCO #1 and #2 films on NSTO, respectively, around the (204) reflection of NSTO showing the two spots related the coexistence of ordered (o-) and disordered (d-) BFCO phases in films.

To quantify the degree of Fe/Cr cationic ordering (R), we carried out a detailed analysis of the normalized intensity of the superstructure peaks. R was estimated from the normalized ratio of the superlattice peak intensity to the main (111) reflection intensity of BFCO in the pseudocubic indexing (**Table 8**). XRD-RSM of BFCO thin films around the NSTO (204) reflection are illustrated in **Figures 52**(c)(d). The small condensed reciprocal area observed in all figures

suggests high quality epitaxial growth of the BFCO thin films on NSTO substrates (i.e., very small mosaicity in crystal plane orientations). The presence of extra spots indicates the presence of two BFCO phases in the films, which we denote as ordered (o-BFCO) and disordered (d-BFCO) phases (**Figure 53**(a)). The positions of the BFCO peaks are located close to that of NSTO along the in-plane reciprocal Q_x axis, suggesting that the film and substrate have a similar in-plane lattice parameter. The calculated in-plane lattice parameters of the BFCO films are listed in **Table 9**, indicating that the films are under a compressive strain, with a lattice mismatch of 0.2–0.3%. However, since we expect that the BFCO films are fully or at least partially relaxed, the possible presence of multi-state valences for Fe and Cr, in particular the 2+ and 4+ states in the films, suggests that the strain is relieved by the Jahn–Teller distortion of oxygen octahedra surrounding these atoms [64].

Table 8 Summary of structural, optical characteristics of BFCO thin films.

BFCO absorber	R (%)	Bandgap (eV)	
		Ordered domain	Disordered domain
BFCO #1	0.31	2.3	2.8
BFCO #2	0.65	1.8	2.8
BFCO #3	0.29	2.4	2.7
BFCO #4	0.68	1.7	2.2

Table 9 Main structural parameters obtained for the different BFCO films.

Sample of BFCO	Ordered domain	Disordered domain
	a (Å) / c (Å) / V (Å^3)	a (Å) / c (Å) / V (Å^3)
BFCO #1	3.911 / 3.976 / 60.82	3.906 / 3.958 / 60.66
BFCO #2	3.919 / 3.970 / 60.97	3.911 / 3.949 / 60.73

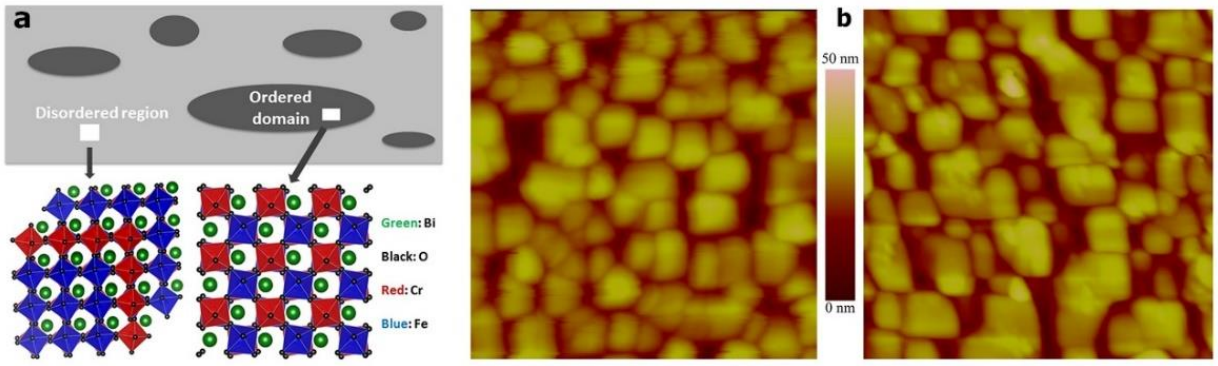

Figure 53. (a) Schematics of the ordered domain in the disordered region of BFCO, and corresponding representation of FeO_6/CrO_6 arrangements in disordered and ordered domain of the double perovskite BFCO. (b) 2×2 μm^2 AFM image for 120 nm-thick BFCO #1 and (b) BFCO #2, the RMS roughness is ~6 nm.

AFM measurements performed on 120 nm-thick BFCO films show that they exhibit a RMS roughness of ~6 nm over an area of 2×2 μm^2, indicating a relatively smooth surface throughout the film (**Figure 53**(b)). Hence, the high crystallinity and atomically smooth surfaces are both critical for the fabrication of heteroepitaxial structure with low-density charged defects, which generally behave as recombination sites for electrons and holes resulting in a decline of performance in PV devices.

6.2.2. Ferroelectric properties

In contrast to conventional *p-n* junction devices, the driving force for the separation of photo-generated carriers in multiferroic-based devices depends on the magnitude of the FE polarization. The FE properties of BFCO films were investigated both at nano- and macro-scale. PFM experiments showed that the FE domains of both BFCO #1 and #2 samples can be individually or partially switched by applying ±8 V voltage pulses, as shown in **Figures 54**(a)(b), respectively. The resulting contrast is a clear proof that ferroelectricity in BFCO exists and can be switched

upon application of an external voltage. Further evidence of FE behavior is the presence of hysteresis loops (**Figures 54**(c)(d)). BFCO film #1 exhibits a stronger PFM response compared to that of BFCO #2 film. The FE behavior of our BFCO films was further confirmed by macroscopic measurements (**Figures 54**(e)). The polarization of film #1 (44 μC cm^{-2}) is observed to be much higher than that of film #2 (14 μC cm^{-2}). The BFCO #2 film with high R (0.65%, **Table 8**) shows a weaker FE polarization than the film BFCO #1 with low R (0.31%, shown in **Table 8**). Consequently, the FE polarization driven force for charge carrier separation in film BFCO #1 is considered to be more significant than that in film BFCO #2, resulting in an enhancement of PCE.

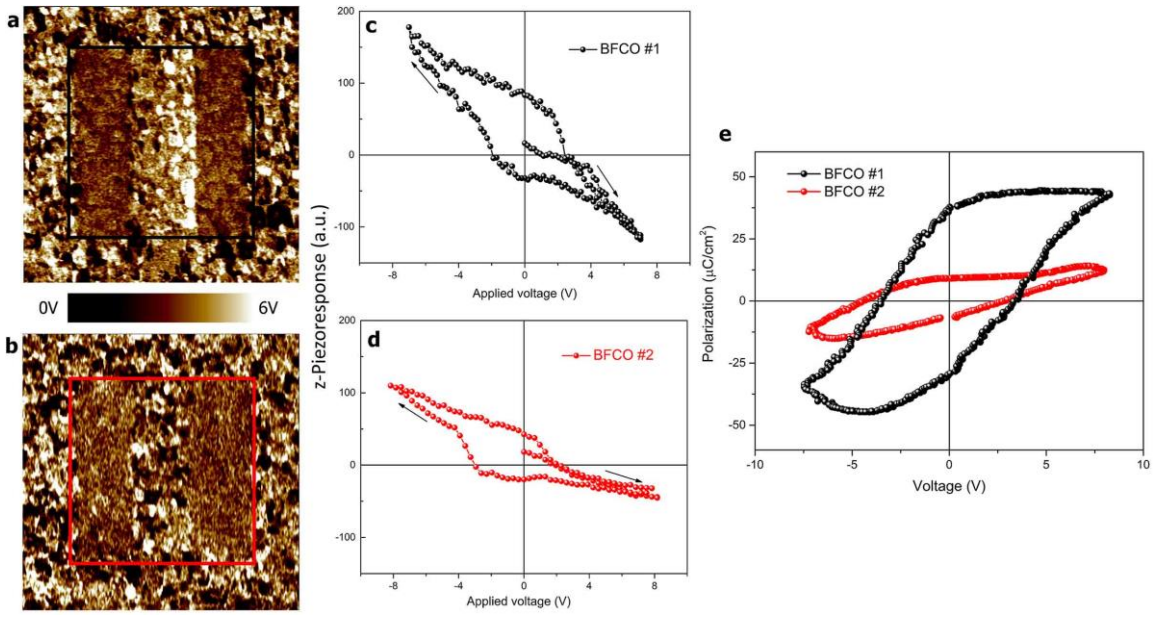

Figure 54. 5 × 5 μm^2 PFM images after switching FE domains for: (a) BFCO #1 and (b) BFCO #2. Corresponding local FE hysteresis loops for (c) BFCO #1 and (d) BFCO #2; (e) FE properties of BFCO #1and BFCO #2 were measured at 2 kHz at RT.

6.2.3. Optical Properties

To understand the optical transition mechanism in double-perovskite BFCO films, the optical absorption properties were characterized by spectroscopic ellipsometry measurements using a

VASE ellipsometer. A multilayer model consisting of air, the BFCO film and the NSTO bottom electrode substrate was used to describe the optical response, including the extinction coefficient *k*. **Figure 55**(a) displays the absorption coefficient α of different BFCO films. The oscillation of the absorption spectra, which implies two absorption areas from the ordered and disordered domains, is observed in all BFCO samples. The oscillation is more pronounced in BFCO #2 due to the combined effect of a relative high value of R (~0.65%) and the large ordered domain size of ~24 nm. A similar finding was reported in our previous work. The optical transition peaks appear mainly between 500 and 700 nm in the absorption spectra for all BFCO films. The coefficient α varies between 0.5×10^5 and 2.0×10^5 cm^{-1} at 520 nm. In addition, we observed a strong dependence (a factor of 4) of the absorption peak area on the ratio R (**Figure 55**(c)), confirming that Fe/Cr cationic ordering is a crucial parameter that can be used to tune the amount of absorbed light in double perovskite BFCO films. This result is in agreement with previous work [64].

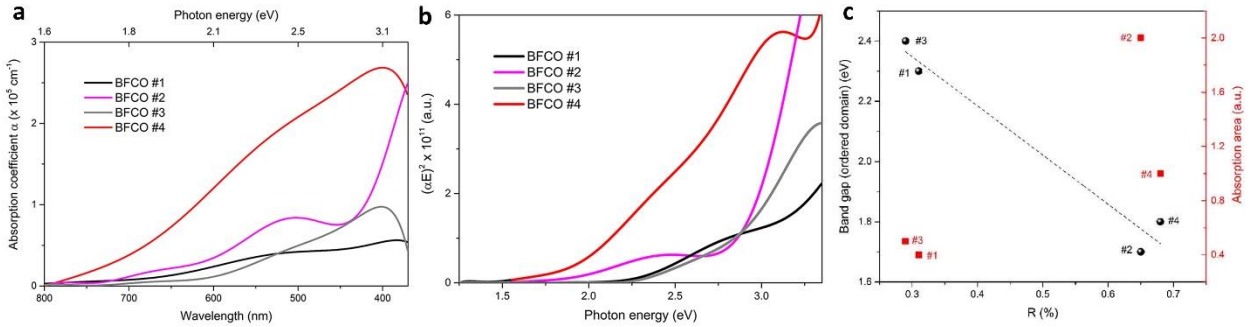

Figure 55. (a) UV-visible absorption spectra of BFCO films; (b) Corresponding direct optical transitions; (c) Bandgap threshold (o-BFCO) and corresponding absorption area vs. R in BFCO films grown using different growth parameters.

Following electronic structure calculations and the experimental absorption spectrum of similar materials with Fe/Cr in B-sites, we designate the peaks at 1.8 and 2.3 eV to charge transfer

excitations between Cr and/or O to Fe mixed *d* orbital Hubbard transitions that occur in locally ordered regions of the sample. In **Figure 55**(b), the first threshold gap observed in the range of 2.2–2.8 eV is attributed to the disordered BFCO phase (d-BFCO). As for the second optical transition region, a linear extrapolation of $(\alpha E)^2$ vs. energy to zero yields bandgaps of 2.3, 1.8, 2.4 and 1.7 eV for films of BFCO #1, #2, #3 and #4, respectively (**Table 8**). These bandgaps are thought to originate from the o-BFCO phase. The bandgap of BFCO is theoretically defined by the difference between the Cr 3*d*–O 2*p* hybrids in the valence band and the empty Fe 3*d* conduction band. Tuning the bandgap requires the modification of the transition metal–oxygen (TM-O) bond lengths and their interaction energies including the hybridization energy and the Coulomb repulsion [142, 143]. Considering the inverse dependence of bandgap with respect to the lattice parameter (i.e. a smaller lattice parameter implies a larger bandgap), we conclude that tuning the bandgap involves altering the lattice parameters, as confirmed in epitaxial BFO films [144, 145]. In our case, the shift in bandgap due to the compressive misfit strain (as calculated in **Table 9**) is 0.5 eV, close to both theoretical and experimental values reported for BFO (0.5 eV) [144, 145]. On another hand, the bandgap tunability is also related to the oxidation states in perovskite structures [146, 147]. The XPS analysis shows that 3+ states are dominant for both Fe and Cr elements (**Figure 56**). According to previous studies, the oxygen octahedra surrounding the TM cations in the (Fe^{3+}) *d*5–(Cr^{3+}) *d*3 system are rigid and will be less sensitive to strain due to the homogeneous distribution of the spins in Fe and Cr degenerate *d*-orbitals [146, 147].

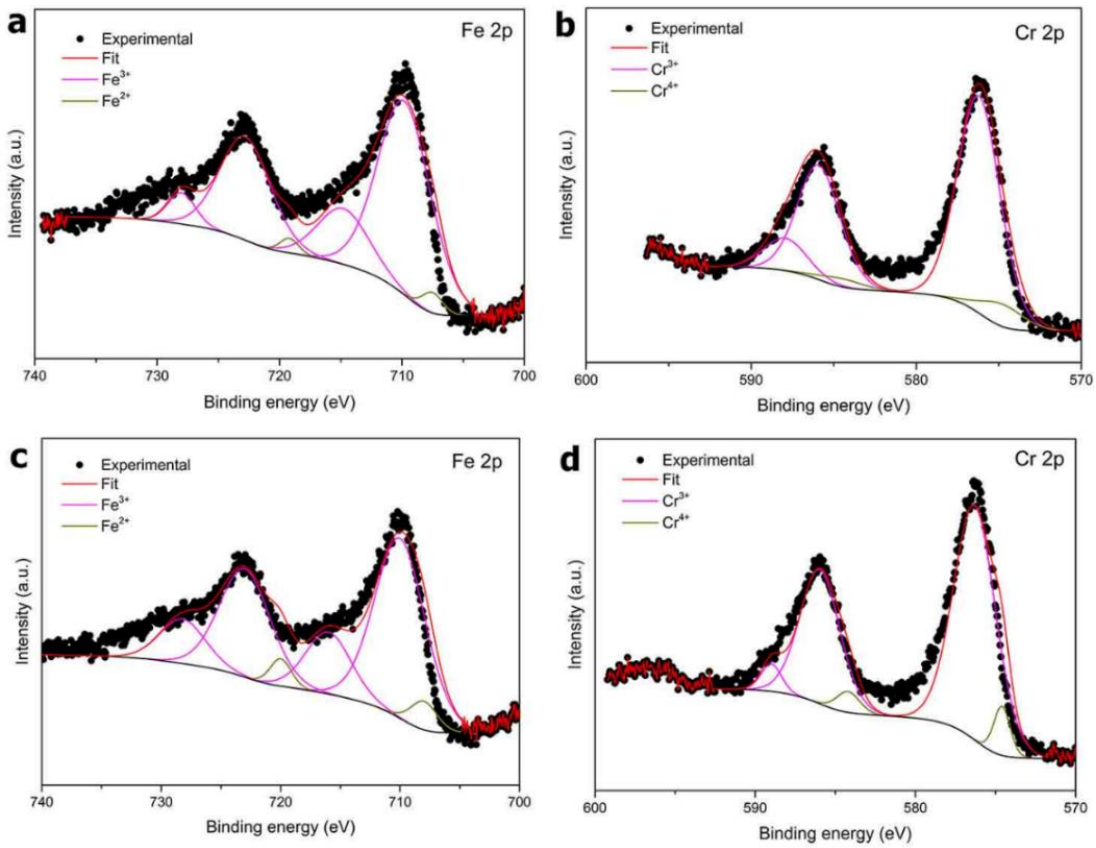

Figure 56. High resolution XPS spectra of (a) Fe 2*p* (b) Cr 2*p* in BFCO #1; (c) Fe 2*p* and (d) Cr 2*p* in BFCO #2.

6.3. Characterizations of NiO thin films

To further confirm the optical energy gap status (e.g., the difference of exciton energy between two different energy levels and/or defects levels) in the obtained BFCO films, the difference of exciton energy was demonstrated in photoluminescence (PL) spectra. The PL peaks at 520 and 720 nm (**Figure 57**(a)) in the PL spectra of the *i*-*n* (BFCO/NSTO) and *p*-*i*-*n* (NiO/BFCO/NSTO) heterojunctions qualitatively confirmed the two band gap thresholds of BFCO at 2.4 eV (517 nm) and 1.7 eV (729 nm) calculated previously in **Figure 55**(b). The PL intensity signal of the *p*-*i*-*n* heterojunction is much weaker than that of *i*-*n* device configuration. The pronounced PL quenching observed in our *p*-*i*-*n* device highlights the crucial role played by the *p*-type NiO layer

as charge-carrier separator and extractor, which induces a reduction of charge carrier recombination and thus improves device performance.

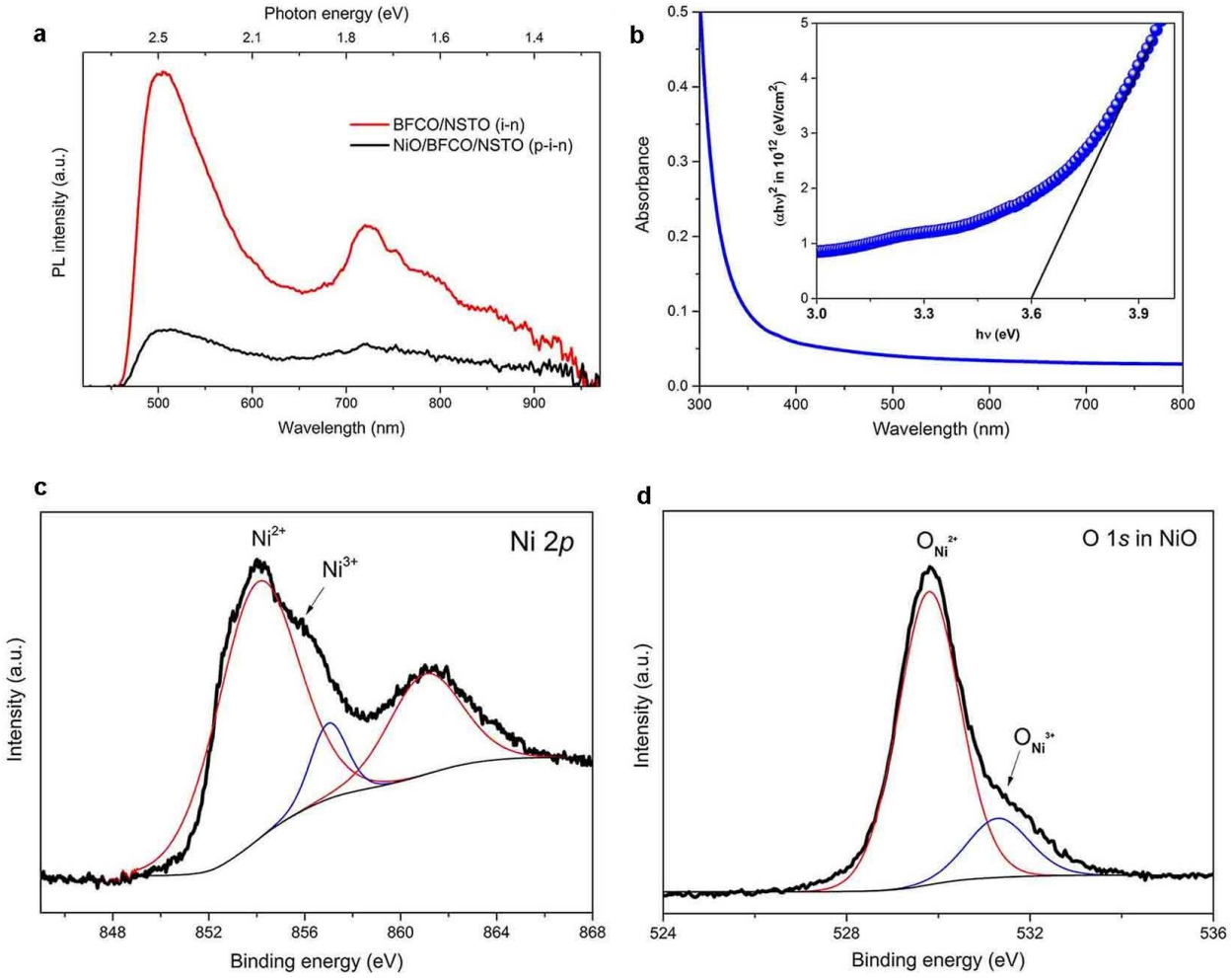

Figure 57. (a) PL spectra of *i-n* and *p-i-n* devices measured at RT; (b) Optical absorbance of NiO film; Inset: corresponding direct optical transition. High resolution XPS spectra of (c) Ni 2*p* and (d) O 1*s* in NiO.

To understand the role of NiO in the devices, we also assessed the optical properties and chemical composition status of *p*-type NiO films. The optical absorbance spectrum is shown in **Figure 57**(b), together with the Tauc plots of $(\alpha h\nu)^2$ vs $h\nu$ (shown as inset). The calculated direct band gap of NiO is derived as 3.6 eV, a value close to that previously reported for PLD-deposited

NiO thin films [13]. The XPS analysis (**Figures 57**(c)(d)) reveals peaks at 854 and 861 eV representing Ni^{2+} in the NiO octahedral bonding configuration in rock-salt NiO structure and a peak at 857 eV associated with the Ni^{3+} state, which implies the occurrence of Ni^{2+} vacancies (metal deficiency) or excess oxygen. These results are in agreement with the previously reported study on PLD-deposited *p*-type NiO thin films employed in *p*-*i*-*n* heterojunction devices [148].

6.4. Photovoltaic performance

A series of PV devices with BFCO #1, #2, #3 and #4 as absorbers (labelled device #1, #2, #3 and #4, respectively) were fabricated by PLD, implementing *n*-type NSTO conducting perovskite substrates as EBL/ETL and bottom electrode; *p*−type NiO conducting films as HTL and two-dimensional arrays of ITO transparent conducting electrodes on top. In **Figure 58**, the PV performance of the two device architectures, the *i*-*n* (BFCO/NSTO) and *p*-*i*-*n* (NiO/BFCO/NSTO) devices are characterized and compared. As shown in **Figure 58**(a), the dark *J*-*V* curve measured from the *i*-*n* junction (device #1) shows a rectifier characteristic, while under the simulated AM1.5 irradiation, the short-circuit current density (J_{sc}), open-circuit voltage (V_{oc}) and fill factor (FF) extracted are 2.77 mA cm^{-2}, 0.44 V and 42%, respectively. This results in a PCE of only 0.5%. This device is based on a BFCO absorber layer with a bandgap (ordered) of 2.3 eV and a FE polarization of 44 μC cm^{-2}. For device #2, based on a BFCO film with a narrower bandgap of 1.8 eV and a FE polarization of 14 μC cm^{-2} the PV performance is improved: J_{sc} and FF are enhanced by 20% and 33%, respectively, yielding a PCE of 0.8%, which represents a 60% enhancement compared to device #1. We attribute the increased J_{sc} and FF to enhanced light absorption and to the excited state of photo-generated carriers promoted by the lower bandgap of the BFCO layer

(e.g., E_g (BFCO #2) = 1.8 eV). The related schematic for *i-n* devices illustrates the mechanism of FE polarization controlled charge carrier separation, as shown in **Figure 58**(b).

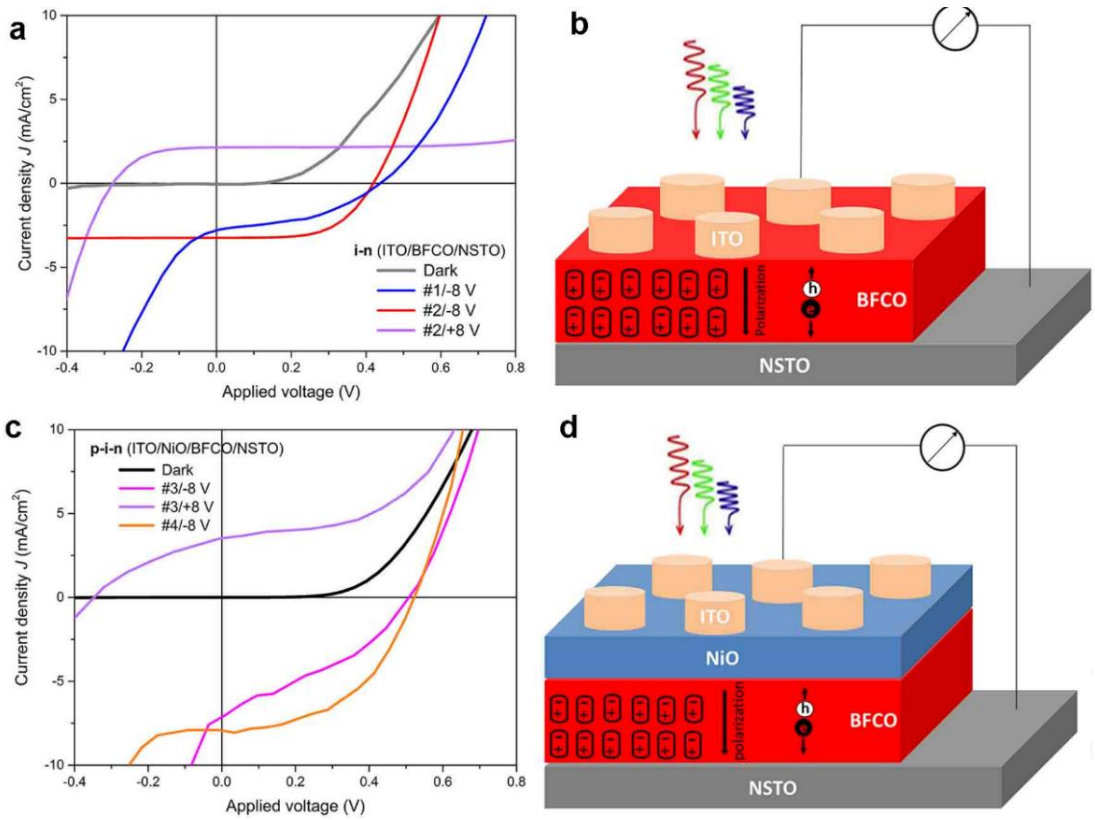

Figure 58. *J-V* characteristics under AM 1.5G illumination for: (a) *i-n* devices and (c) *p-i-n* devices; Layout of the devices for: (b) *i-n* and (d) *p-i-n*, and the schema of FE polarization controlled charge carrier separation.

FE polarization is crucially important for the tunability of the internal depolarization electric field and the optimal surface band structures which could enhance the PV performance. Thus we aim to apply electric poling on electrodes to understand the FE polarization controlled PV performance and charge transfer behavior in BFCO films. During *J*-V measurements, the samples have undergone poling pre-treatments in two different directions (±8 V). The positive voltage was applied to the NSTO electrode, resulting in an electric field with opposite direction to

the bottom barrier field and in the same direction as the top one. All the PV parameters of the tested devices are summarized in **Table 10**.

Table 10 PV performance of BFCO-based heterojunctions with NSTO or/and NiO.

Device (type)	BFCO Absorber	J_{sc} (mA/cm^2)	V_{oc} (V)	FF	PCE (%)
#1 (*i*−*n*)	BFCO #1	2.77	0.44	0.42	0.5
#2 (*i*−*n*)	BFCO #2	3.30	0.42	0.56	0.8
#3 (*p*−*i*−*n*)	BFCO #3	7.17	0.51	0.33	1.2
#4 (*p*−*i*−*n*)	BFCO #4	7.97	0.53	0.48	2.0

Figure 58(c) shows the *J*-*V* curve measured on *p*-*i*-*n* heterojunction devices (i.e. NiO/BFCO/NSTO, as shown in **Figure 58**(d)). For device #3 The dark *J*-*V* curve behaves like a diode with good current rectification with the dark current density of about 0.15 mA/cm^2 at +0.3 V, while under illumination the device shows a J_{sc} of 7.17 mA cm^{-2}, a V_{oc} of 0.51 V, and a FF of 33% yielding a PCE of 1.2%; device #4 shows improved PV parameters compared to device #3, with a J_{sc} of 7.97 mA cm^{-2}, a V_{oc} of 0.53 V, a FF of 48% and a PCE of 2.0%. However, when comparing with the *i*−*n* configuration device (e.g., device #1), the V_{oc}, J_{sc} and PCE of the *p*–*i*–*n* device (e.g., device #4) increased by a factor of 1.2, 3.0 and 4.0, respectively. The photocurrent is significantly increased, confirming that the main contribution to the PV output in the device originates from excited photocarriers generated inside the BFCO layer and possibly the increase of driving force provided by the electric field, both promoted by the depletion regions formed at the *p*-*i* and *i*-*n* interfaces in the *p*-*i*-*n* heterojunction. The main factors which affect the fill factor are the series resistance, the parallel (shunt) resistance of the recombination current in the space charge region of the PV device. The increased V_{oc} and J_{sc} are thought to originate from the increased shunt resistance (from 269 to 323 Ω cm^2) and decreased series resistance (from 57 to 25

Ω cm^2) of the device under illumination. The FF reduction is attributed to the charge carrier recombination due to the presence charged defects (such as Ni^{2+} vacancies or excess oxygen) in the NiO thin film and related interfaces, which was partly confirmed by XPS in the previous paragraph (**Figures 57**(c)(d)).

These results hence imply that two depletion regions in *p-i-n* heterostructures (operative at the *p-i* and *i-n* interfaces) together have contributed favorable PV properties. Although photo-generated carriers can also be excited in the NSTO and NiO layers by the UV component of solar light, their contribution was proven to be negligible [149]. Switching the FE polarization by applying a pulse of -8 V to the bottom electrode reverses the sign of both V_{oc} and J_{sc} of the device (**Figure 58(c)**).

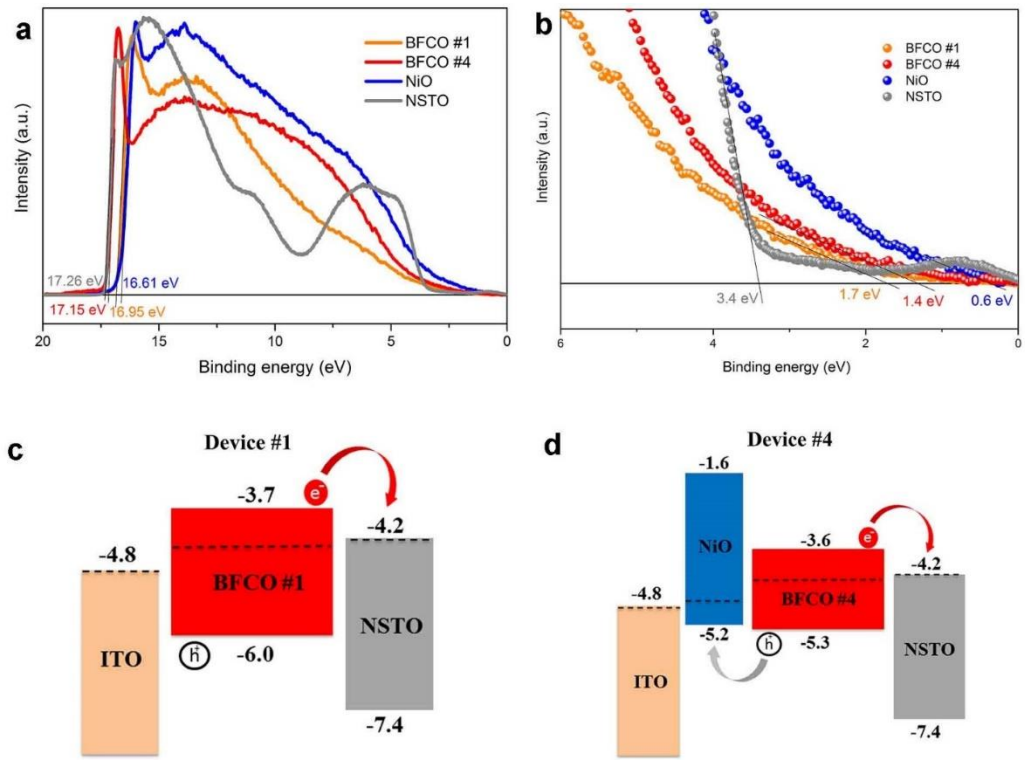

Figure 59. (a) Representative UPS measurements of NiO, BFCO #1, #4 and NSTO; (b) The detailed UPS valence band structure of films between 0 to 6 eV. Energy-level diagram based on

UPS results showing the valence, Fermi and conduction energy of each component material included in: (c) device #1 (*i*-*n*), and (d) device #4 (*p*-*i*-*n*).

To understand the PV performance of BFCO-based devices and the effective transport of photo-generated carriers, we analyzed their electronic structure using UPS. The energy-level diagrams of each component material used in the BFCO devices are illustrated in **Figures 59**(c)(d). The determination method of the electron affinity E_c, work function E_f and ionization potential E_v is described in **Figures 59**(a)(b). Qualitative analyses were performed only for ordered domain BFCO based on the UPS results because of the complex nature of the ordered/disordered phases coexisting in the BFCO films, making the construction of the energy band diagrams extremely challenging. As illustrated in **Figures 59**(c)(d), the band edge positions of the BFCO, NSTO and NiO are well aligned, favoring the effective transport of photo-generated carriers.

6.5. External quantum efficiency (EQE)

EQE measurements (**Figures 60**) of device #1 (*i*-*n*) and device #4 (*p*-*i*-*n*) were carried out after orienting the spontaneous polarization towards the surface (by applying +8 V bias to the NSTO) at RT. Device #1 exhibits a continuous photoresponse from 400 to 850 nm, with a maximum EQE of 12% at 560 nm (2.2 eV), which is close to the value of the absorption edge (2.3 eV in the ordered domain) of the intrinsic absorber BFCO #1. When decreasing the wavelength of incident light, the EQE of device #4 starts to increase at 850 nm, then shows a shoulder at 760 nm, a peak at 650 nm (1.9 eV), reaching the maximum EQE value of 32%, which is comparable to the quantum efficiency achieved within a single FE domain or domain walls [150]. The maximum EQE of *p*-*i*-*n* heterojunction is much higher than that of the *i*-*n* junction. These results clearly demonstrate that

the PV response is mainly given by the photocarriers excited inside the BFCO and that the NiO layer in the *p-i-n* device induces a more efficient photocarrier extraction.

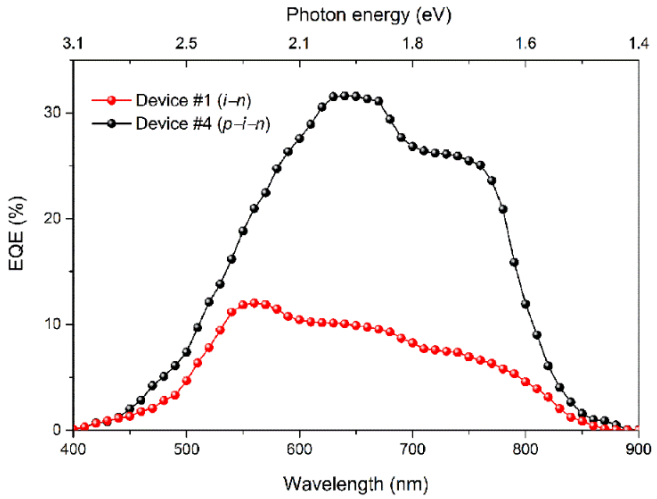

Figure 60. EQE measurements of device #1 (*i-n*) and device #4 (*p-i-n*).

6.6. Electrochemical Impedance Spectroscopy (EIS)

We applied EIS to better understand the role of the NiO layer in the *p-i-n* device. The analysis was carried out in dark and with no dc bias applied during the measurement. In **Figure 61**(a) is reported the complex impedance for a representative *p-i-n* (device #4) and *i-n* (device #1) sample. It is possible to distinguish two semicircles, one at high frequency (left-most) and one bigger semicircle at medium-low frequency. The latter can be related to the bulk material. For dark condition, the *p-i-n* sample exhibits the highest bulk resistance and capacitance, similarly to previous work [151]. Another feature that can be extracted from the EIS is the general behavior of the overall capacitance processes. **Figure 61**(b) shows the trend of the real part of the capacitance and the phase as a function of the frequency obtained at short-circuit condition in dark. Clearly the two samples have different complex impedance behavior. At high frequency, the *p-i-n* device presents a plateau (indicated as a peak around 100 kHz in the phase plot) that usually is related to

the bulk capacitance and which we associate, in this case, to the capacitance of the *p-i* junction. The *i-n* device shows a plateau at medium frequency (around 1 kHz) while the *p-i-n* junction shows a similar feature one order of magnitude below, around 100 Hz, confirming the presence of the *i-n* junction in both the devices. A static dielectric capacitance at low frequency can be identified for both cells. Therefore, from the EIS it is inferred that two depletion regions (interfacial regions at *p-i* and *i-n*) were formed in the *p-i-n* heterostructures. This behaviour indicates that the two depletion regions formed at the *p-i* and *i-n* and an internal field adds across the entire layer of BFCO, providing the necessary force to drive the photo-generated carrier's separation, yielding an efficient PV performance.

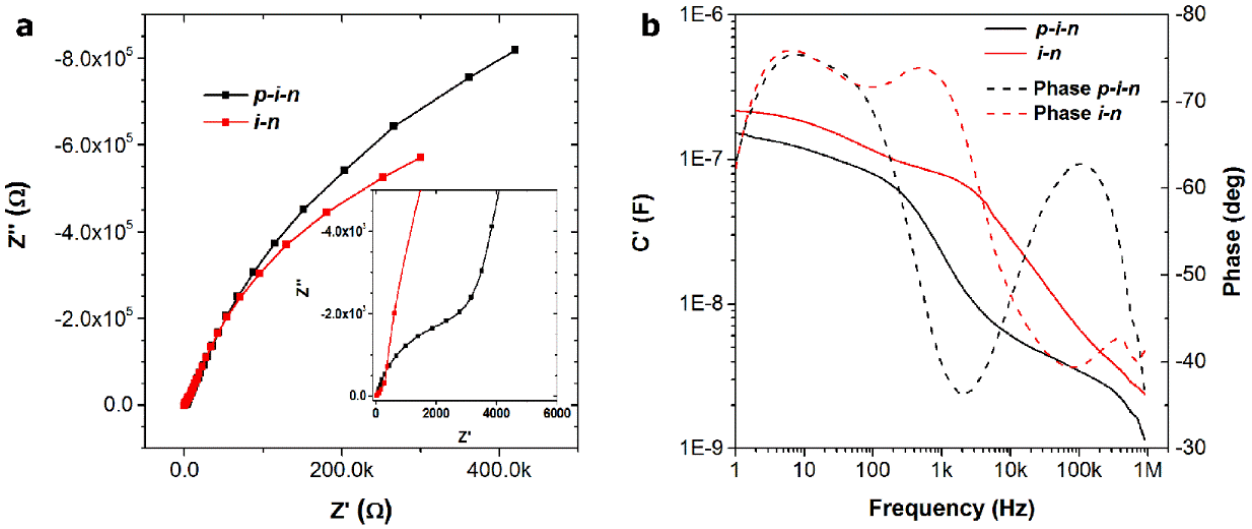

Figure 61. (a) Plots of the real and imaginary components of the complex impedance of device #4 (*p-i-n*) and device #1 (*i-n*) heterojunction under a dark condition. The inset shows the details between 0 and 6000 Ω; (b) The trend of the real part of the capacitance (left axes) and the phase (right axes) as a function of the frequency obtained at short-circuit condition in dark.

6.7. Summary

In summary, we report the fabrication of multiferroic BFCO-based *p*-*i*-*n* heterojunction devices using PLD technique. A *p*-type NiO semiconductor thin film acting as an EBL/HTL and a typical *n*-type NSTO acting as ETL were used to form the double-interfaced heterojunction based on all-inorganic oxide, multiferroic and perovskite materials. Current−voltage characteristics recorded under dark and white light illuminated conditions showed that the PV properties improved due to two depletion regions formed at the *p*-*i* and *i*-*n* interfaces in the *p*-*i*-*n* heterojunctions. These results are also confirmed by EIS measurements. We systematically investigated the mechanism of charge carrier separation, transport and collection in multiferroic oxide based single-layered devices with *p*-*i*-*n* heterojunction, and demonstrated the complex relationships between the structural, optical, electrical and FE properties of BFCO films sandwiched between *p*- and *n*-type oxides, and how they affect the PV performance of devices.

Chapter 7. Enhanced Photoelectrochemical Performance in *p*-Type Transparent Conducting Oxides coated Multiferroic Oxide Thin Films

So far, we have studied the functional properties of multiferroic BFCO thin films including photoconductive and photovoltaics, and their applications in solar energy conversion, such as photodetectors and solar cells. Li *et al*. [65] first reported the fabrication of a photocathode consisting of a *p*-type BFCO epitaxial thin film for visible-light-driven water reduction and achieved a highest photocurrent density, up to −1.02 mA cm^{-2} at −0.97 V vs. RHE in 1 M Na_2SO_4 under AM 1.5G simulated sunlight. Nechache *et al*. [64] indicated that the *n*-type BFCO epitaxial thin film (with small E_g, <2.0 eV) is a promising candidate for the design of efficient PV devices. Hence it is greatly interesting to design the *n*-type BFCO based photoelectrode for solar-driven water splitting, and further investigate the tailoring of PEC activity by manipulating the FE polarization.

Furthermore, the semiconductors with small E_g (<2.0 eV) typically corrode or passivate when used as photoanodes in contact with aqueous electrolytes [152], and thus such materials must be stabilized by the surface treatment and modification or using a protection layer before they can be used as photoelectrodes in a PEC device [153-155]. Moreover, the PEC performance of the intrinsic *n*-type semiconductors based photoanodes could be improved by coating with an effective electron-blocking layer (EBL), due to the reduction of photogenerated charges recombination, and consequently resulting in the efficient OER [156]. Therefore, it requires to design a protection and electron-blocking functional layer having the chemically stable, oxidation resistant and transparent conducting properties [152]. The more potential materials are *p*-type transparent conducting oxides

(TCOs), also called *p*-type window layer, and generally metal oxide. Nickel oxide (NiO) is a cubic *p*-type semiconductor with wide bandgap (~3.6 eV) [13], larger than that of the commonly used *p*-type TCOs like Cu_2O (~2.1 eV) [156] and Co_3O_4 (~2.6 eV) [157]. Additionally, in the form of very thin layers, NiO exhibits a high optical transparency (e.g., ~80% at 5 nm [13]), low electrical resistivity (~120 Ω cm [158]) and *p*-type hole conduction with high conduction band minimum (CBM) to function as an EBL [113].

7.1. Experimental method

BFCO films in 90 nm thickness were epitaxially grown on (100)-oriented STO substrates buffered with a 15 nm-thick SRO layer as bottom electrode by PLD using an energy density of ~1.7 J cm^{-2} at a repetition rate of 8 Hz. The deposition temperature and oxygen partial pressure were 680 °C and 6 mTorr for BFCO, 20 mTorr for SRO films growth, respectively. After deposition, the samples were cooled to RT under the same oxygen pressure used for deposition. ~10 and 20 nm-thick NiO films were grown on top of the BFCO, without breaking the vacuum, using the same laser set at the same energy density, at a repetition rate of 5 Hz. The deposition temperature and oxygen partial pressure were 200 °C and 10 mTorr, respectively.

7.2. Characterizations of BFCO thin films

The epitaxial growth of 90 nm-thick double-perovskite BFCO films on perovskite (100) STO substrates, buffered with 15 nm-thick perovskite SRO layer is expected to result in high crystalline quality with smooth interfaces. **Figure 62**(a) shows the B-site double-perovskite structure ($A_2BB'O_6$) of ordered-BFCO crystals using ball-and-stick style. **Figure 62**(b) displays the XRD θ−2θ scans pattern of the BFCO films. The (0 0 *l*) (*l*=1, 2, 3) peaks confirm the *c*-axis orientation

of the films with the absence of any secondary phase. The (0 0 *l*) reflections of the SRO layer are located at angles very close to those of the BFCO (0 0 *l*) reflections, thus buried within the (0 0 *l*) reflections of BFCO. The Fe/Cr cationic ordering in BFCO was characterized by performing asymmetrical θ–2θ scans around (111) STO reflections (**Figure 62**(c)). The ratio (R) of degree of Fe/Cr cationic ordering is given a value of ~0.5% implying a relatively narrow E_g for our BFCO film (discussed in the following part) based on previous works.

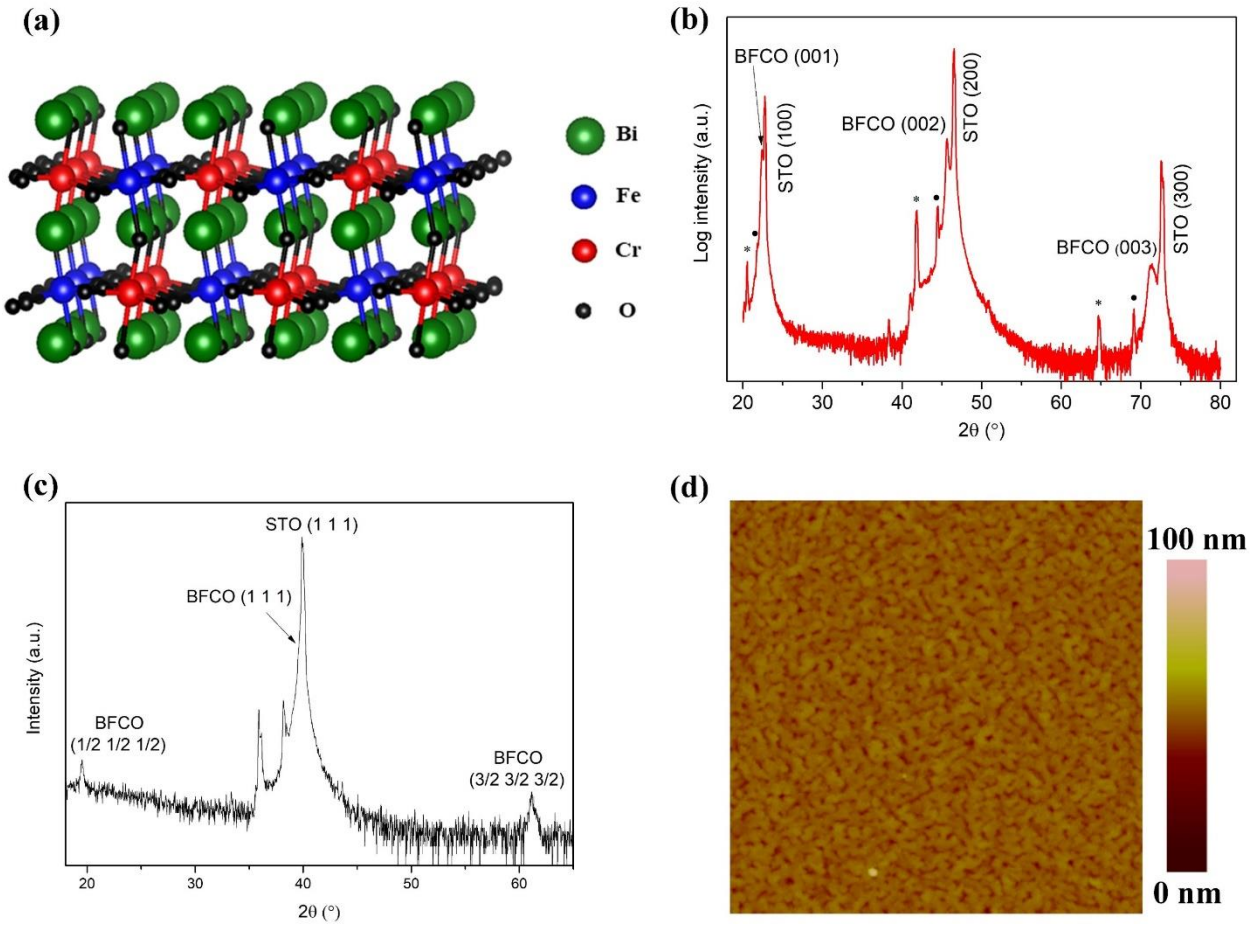

Figure 62. (a) Double-perovskite structure of ordered BFCO crystals using ball-and-stick style. (b) θ-2θ scan for BFCO thin film epitaxially grown on (100) STO, buffered with SRO layer. (c) Asymmetric scan around (111) plane of (100) STO for BFCO. (d) 5×5 μm^2 AFM topography image for 90 nm-thick BFCO film grown on SRO/STO substrate.

The nano-level topography of surface for 90 nm thick BFCO film was recorded by AFM measurements (**Figure 62**(d)) exhibiting a roughness of ~3.2 nm over an area of 5×5 μm^2, indicating a highly smooth surface throughout the films. Hence, the high crystallinity and atomically smooth surfaces are both critical for the fabrication of heteroepitaxial structure with low-density charged defects, which generally behave as recombination sites for electrons and holes resulting in a decline of performance in devices (e.g., PV, PEC).

Unlike conventional *p-n* junction, the driving force for the separation of photo-generated carriers in FE materials depends strongly on the magnitude of the FE polarization. The FE properties of BFCO films were investigated both at nano- and macro-scale. PFM experiments showed that the FE domains of BFCO films can be switched by applying ±8 V voltage pulses, as shown in **Figure 63**(a). The resulting contrast is a clear proof that ferroelectricity in BFCO exists and can be switched upon application of an external voltage. Further evidence of FE behavior is the presence of hysteresis loops (**Figure 63**(b)). The setup of PFM is shown in the inset of **Figure 63**(b). The FE behavior of our BFCO films was further evaluated by macroscopic FE measurements (**Figure 63(c)**). The magnitude of polarization of BFCO films is observed to be 20 $\mu C\ cm^{-2}$. So far, we have comprehensively investigated the structural and FE properties of our BFCO epitaxial thin films.

To understand the optical transition properties in single-crystalline BFCO epitaxial thin films, the optical absorption properties were characterized by spectroscopic ellipsometry measurements using a VASE ellipsometer. The optical response data including extinction coefficient *k* and refractive index *n* were fitted by ellipsometric analysis program WVASE, and the spectra of absorption coefficient α of BFCO films extracting from *k* is displayed in **Figure 63(**d). The optical transition peak appears mainly between 420 and 700 nm in the absorption

spectra. The maximum coefficient α is 2.5×10^5 cm^{-1} at 520 nm. The two threshold gaps were observed in the right *y*-axis of **Figure 63**(d). The first threshold gap located at 2.8 eV is attributed to the disordered phase of BFCO. As for the second optical transition region, a linear extrapolation of $(\alpha E)^2$ vs. energy to zero yields E_g of 1.8 eV which is thought to originate from the ordered BFCO domain [64, 113].

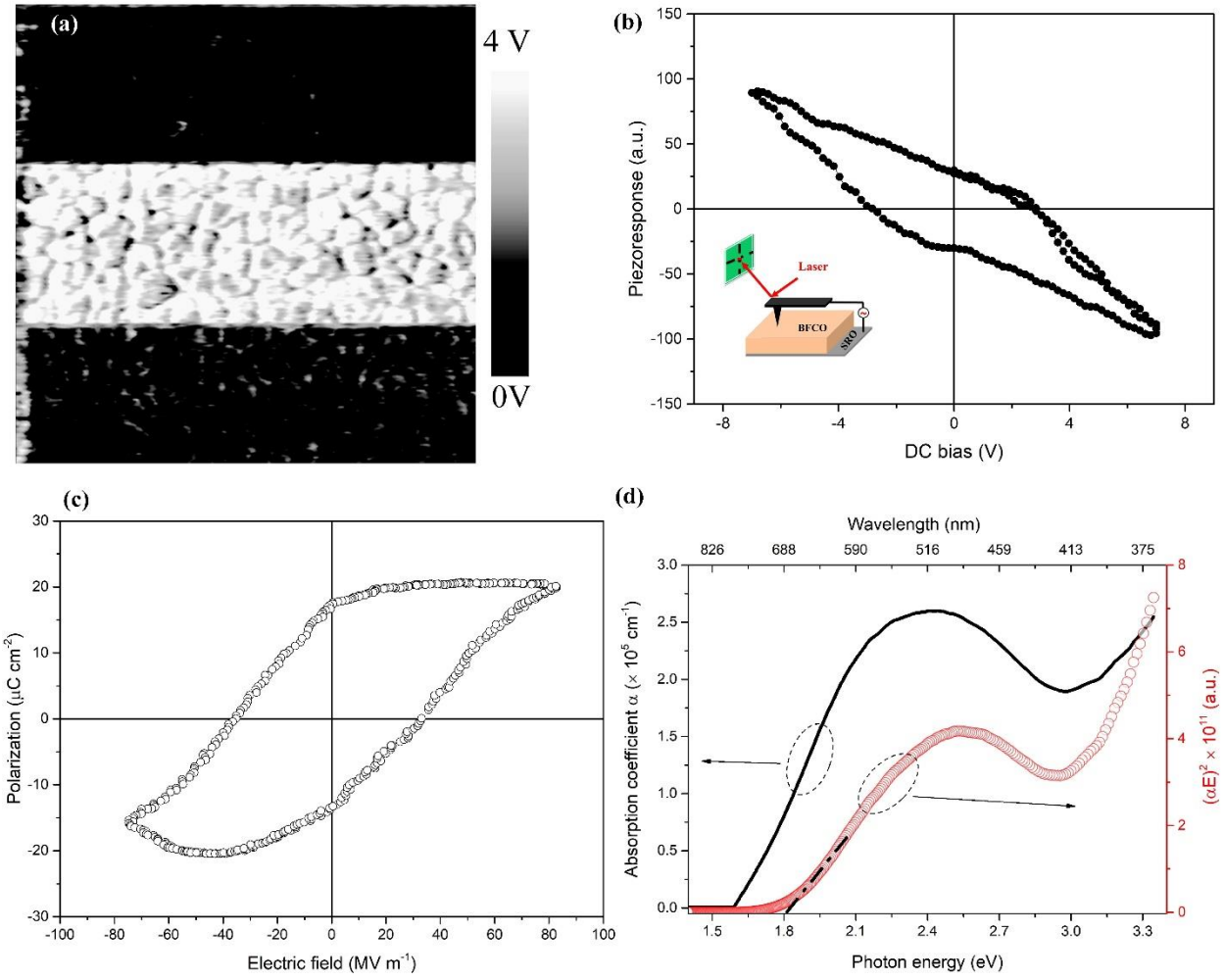

Figure 63. (a) 3×3 μm^2 PFM image of BFCO on SRO/STO underwent ±8 V pulse switching FE domains, and (b) Corresponding FE hysteresis loop. Inset shows the setup of PFM. (c) FE polarization−electric field hysteresis loop measured on BFCO thin films at 2 kHz at RT; (d) Visible-light absorption spectra of BFCO thin films and corresponding direct optical transitions.

7.3. Characterizations of NiO thin films

Before discussion on the *p*-NiO/*n*-BFCO heterojunction, it is necessary to gain insight into the transparent conducting *p*-type NiO thin films alone. The PLD-deposited NiO films in 10 and 20 nm thickness were directly grown on double-polished transparent (100) STO substrates, respectively. The optical transmission and absorbance spectra at UV-visible range are shown in **Figure 64**(a). The optical transmission at visible range for 10 nm NiO film is ~70%, higher than that of 20 nm NiO film (~60%), suggesting that the thicker film absorbed more photons than the thinner film of NiO. This is also confirmed by the optical absorbance measurements (shown as the right y-axis in **Figure 64**(a). Together with the Tauc plots of $(\alpha E)^2$ vs. E (shown as inset). The calculated direct E_g of NiO thin films acting as window layer is derived as ~3.6 eV.

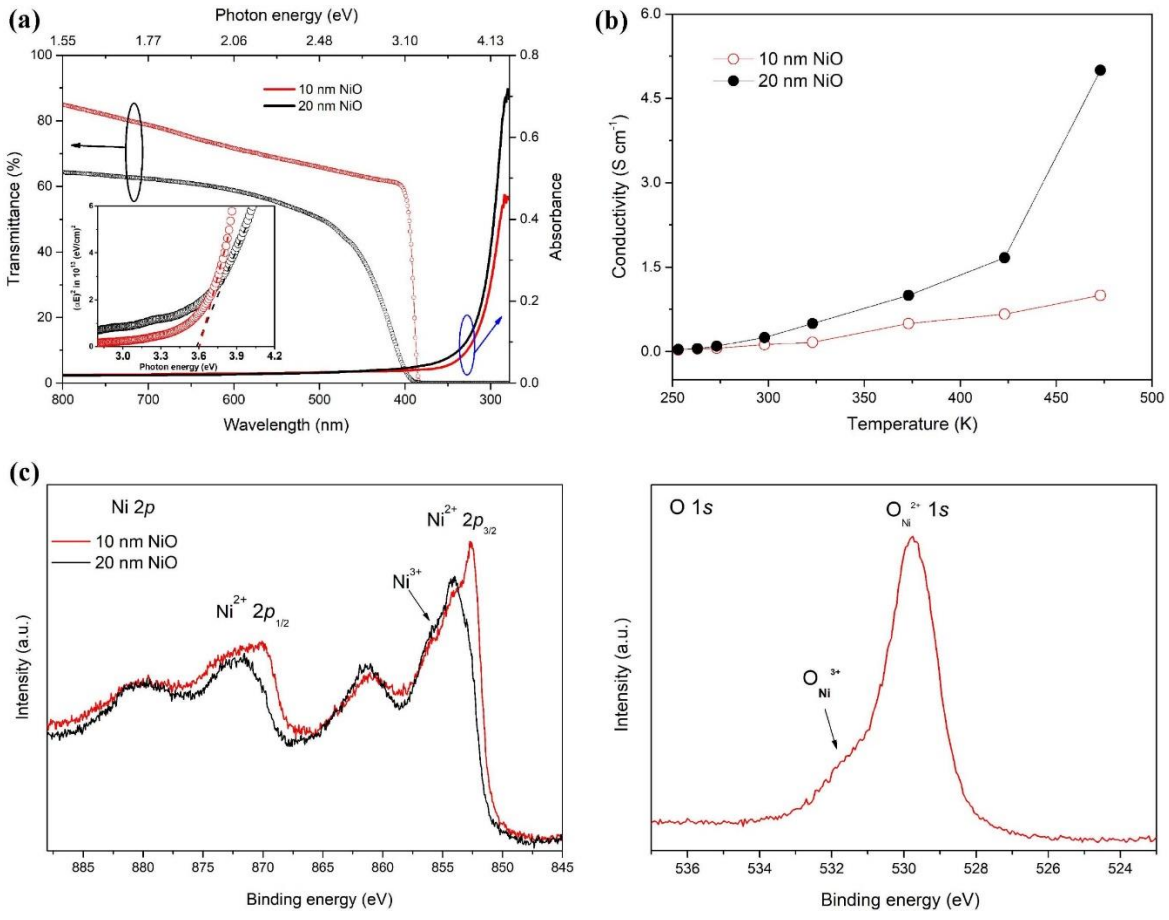

Figure 64. (a) Optical transmission and absorbance of NiO films grown on transparent STO substrate; Inset shows corresponding direct optical transition. (b) Conductivity−temperature measurements of NiO thin films. (c) XPS spectra of NiO thin films for: Ni 2*p* and O1*s*.

Moreover, we have also investigated the electrical properties of NiO thin films in different thickness. The enhancement of electrical conduction with temperature increases from 253 to 473 K demonstrates a typical semiconducting behaviour with a good conductivity of ~0.13 S cm^{-1} for 10 nm NiO and ~0.25 S cm^{-1} for 20 nm NiO at 300 K (**Figure 64**(b)). These values indicate a 15−30 fold enhancement compared with previous reported one [158]. The conductivity increase is thought to be the presence of Ni^{2+} vacancies or O_2 interstitials in PLD-deposited NiO films [113, 148], which was partially confirmed by X-ray photoelectron spectroscopy (XPS) measurements (**Figure 64**(c)). The hole concentration and mobility were respectively given to be 1.2×10^{18} cm^{-3}, 0.7 cm^2/Vs for 10 nm NiO and 1.5×10^{18} cm^{-3}, 1.1 cm^2/Vs for 20 nm NiO determined by Hall-effect measurements. These values suggest that the high carrier densities and mobility were achieved in our PLD-deposited *p*-type NiO thin films. Heretofore, we have understood the optical and electrical properties of our transparent conducting *p*-type NiO thin films.

7.4. Photoelectrochemical (PEC) performance

7.4.1. Tailoring PEC performance of the bare BFCO photoelectrodes

To appraise the PEC performance of bare BFCO thin films based photoelectrodes for water decomposition, linear sweep voltammetry (*J*-*V*) curves were measured under chopped AM 1.5G simulated sunlight illumination with intensity of 100 mW cm^{-2}, so as to monitor simultaneously the dark and light current. The device schematic of the BFCO thin films used as photoanode in a PEC cell designed for possible water splitting is shown in **Figure 65**(a).

As shown in **Figure 65**(b), the bare BFCO photoelectrode achieved an anodic photocurrent density of +0.1 mA cm^{-2} at a +1.23 V (vs. RHE) applied bias after subtraction of the dark current in the electrolyte consisting of 1 M Na_2SO_4 at pH 6.8. The onset potential is as low as 70 mV (vs. RHE). The open-circuit potential (V_{oc}) decreased on exposing the electrode to illumination (**Figure 65**(b), inset), suggesting a typical *n*-type semiconductor behavior which is similar to our previous study on an *n*-type BFCO film with numerous oxygen vacancies, acting as intrinsic absorber involved in a PV device. However this is contrary to the previously reported *p*-type BFCO thin films buffered with a $CrRuO_3$ layer grown at relatively high oxygen pressure (~10 mTorr) and laser fluence (~2.1 J cm^{-2}) conditions which supressed the formation of oxygen vacancies and lattice defects in BFCO crystals, demonstrating a photocathodic water splitting with a maximum photocurrent density of −1.02 mA cm^{-2} at −0.97 V (vs. RHE) for solar-driven water reduction to hydrogen evolution. Therefore, the *n*-type BFCO based photoanode for water oxidation is complementary to the previous study on *p*-type BFCO based photocathode used in PEC cells.

To gain an insight into the effect of FE polarization on PEC properties, *J-V* measurements were carried out for bare BFCO photoanode with two opposite FE polarization directions. The silver electrodes were deposited on top of the BFCO films for achieving the electrical poling. An upward/downward polarization (labelled P_{up} and $P_{down,}$ respectively) was carried out by +/−15 V pulse electric poling during 1 μs, respectively. The positively poled (P_{up}) BFCO films based photoanodes exhibited a photocurrent density of +0.06 mA cm^{-2} at +1.23 V (vs. RHE) (**Figure 65**(b)), slightly smaller than that of the sample at virgin state (as-grown). The onset potential reduced to 30 mV (vs. RHE). By contrast, for the negatively poled (P_{down}) BFCO films, the photocurrent density increased to +0.15 mA cm^{-2} (**Figure 65**(b)) at the same bias, which shows a 50% and 2.5-fold enhancement compared with the sample at virgin state and P_{up}, respectively. The

onset potential remains to be the same 30 mV (vs. RHE) as before. Thus, BFCO films with a negative polar surface (P_{down}) are advantageous for enhancing their PEC performance for water oxidation, whereas BFCO films with a positive polar surface (P_{up}) are unfavorable.

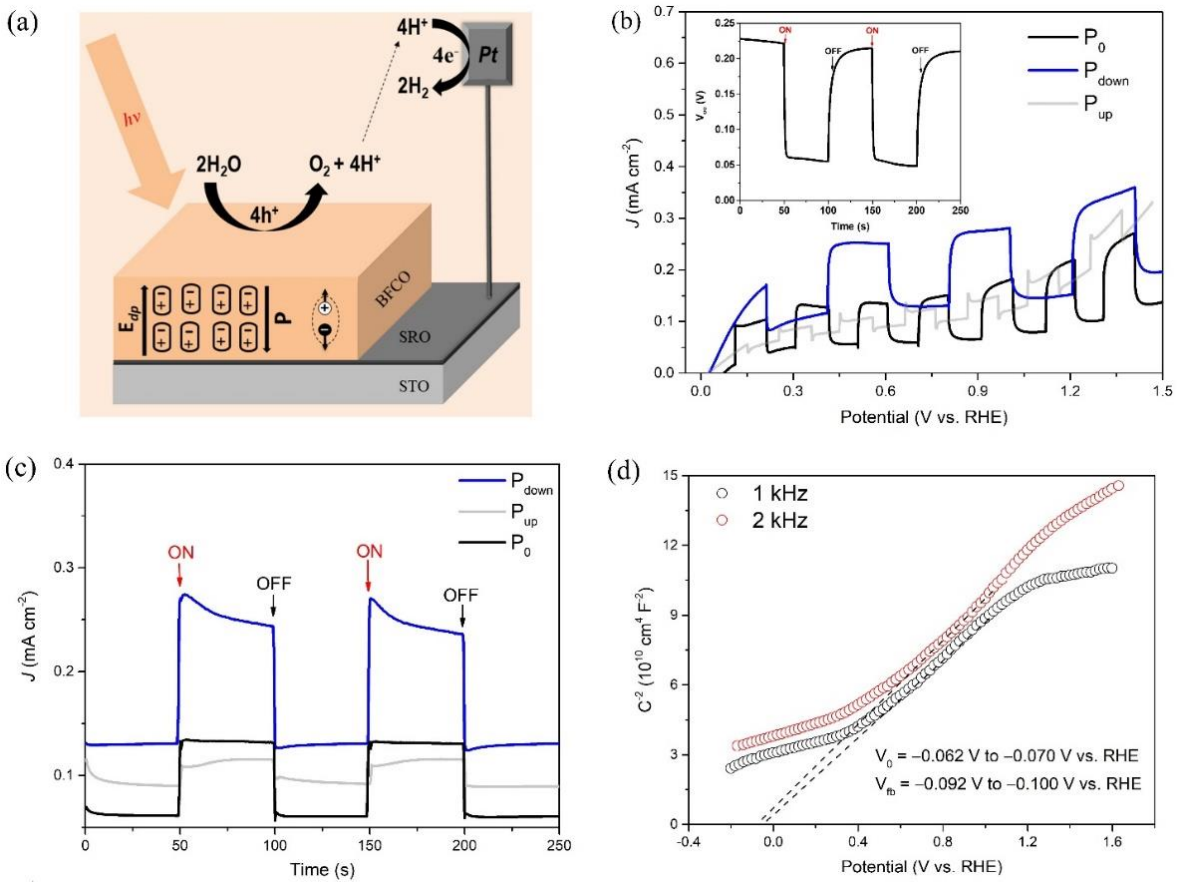

Figure 65. (a) Diagram of a BFCO based photoanode, showing one possible FE polarization direction. (b) Variations of the *J*-*V* curves of samples at virgin state, P_{up} and P_{down} in Na_2SO_4 under chopped light. Inset shows the open-circuit potential (V_{oc}) vs. time, and (c) Corresponding photoresponse before and after poling with two opposite directions under chopped light at +0.6 V (vs. RHE). (d) Mott–Schottky (M-S) measurements of samples at 0 V with frequency of 1 and 2 kHz.

Figure 65(c) shows the transient photoresponses of the bare BFCO photoanodes with different polarization states, determined by photocurrent density–time (*J*-*t*) curves measurements at +0.6 V (vs. RHE) under chopped illumination. Under illumination, all three showed a marked increase in photocurrent at the beginning and end of each chop, indicating that the carrier transport of the layered photoelectrodes is quite fast. The photocurrent densities of the bare BFCO photoanodes at virgin state, P_{up} and P_{down} are 0.07 mA cm^{-2}, 0.02 mA cm^{-2}, and 0.12 mA cm^{-2} at 0.6 V (vs. RHE), respectively, which are in accordance with the *J*-*V* curves as shown in **Figure 65**(b). Furthermore, after poling with −15 V (P_{down}), the photocurrent enhanced 1.7 and 6-fold compared with the same sample at virgin state and P_{up}. These values show that the performance of the bare BFCO photoelectrodes can be effectively tuned by FE polarization switching.

The flat band potential (V_{fb}) of the BFCO thin film was determined via a Mott–Schottky analysis using capacitance impedance measurements on the electrode/electrolyte at 1 and 2 kHz frequencies in the dark condition (**Figure 65**(d)). The positive slope of the C^{-2} curve indicate that the majority carrier of BFCO thin films is electron. Thus, the *x*-axis intercept (V_0 = −0.062 to −0.070 V vs. reversible hydrogen electrode (RHE)) can be used to determine V_{fb}, which yields a V_{fb} from −0.092 to −0.10 V vs. RHE for both frequencies (1 and 2 kHz). The conduction band (CB) edge were located at −0.490 to −0.498 V (vs. RHE), the valence band (VB) edge would then occur at +1.30 to +1.31 V vs. RHE (shown as **Figure 66**(a)). The calculation details are demonstrated in following, and these values are also confirmed by UPS measurements.

Calculation of the flat-band potential (V_{fb}) and the donor density (N_D) was carried out by Mott-Schottky measurements: the flat-band potential (V_{fb}) of unpoled photoelectrodes can be inferred from Mott-Schottky relation as following **equation (6)** [159]:

$$C^{-2} = \frac{2}{(e\varepsilon_0 \varepsilon_r N_D A^2)(V - V_{fb} - {}^{kT}/_{e})} , \qquad (6)$$

where C is the capacitance of space charge layer, e is the electron charge (~1.6×10^{-19} C), ε_r is the dielectric constant (~80 was used according to our C–V measurements [65]), ε_0 is the vacuum permittivity (~8.85×10^{-12} F m^{-1}), N_D is the carrier density in BFCO (cm^{-3}), V is the applied voltage (V), k is Boltzmann's constant (~8.62×10^{-5} eV K^{-1}), T is the Kelvin temperature (300 K) and A is the surface area in contact with the electrolyte (cm^2).

Therefore, plotting C^{-2} vs. V allows the estimation of the V_{fb} and N_D, with the flat-band being the x-intercept using the following **equation (7)**:

$$V_0 = V_{fb} + {}^{kT}/_{e} \ , \qquad (7)$$

The carrier concentration (N_D) can be calculated from the slope of the line $2/e\varepsilon_r\varepsilon_0 N_D A^2$.

The conduction band edge (E_{CB}) is calculated using the following **equation (8)** which is valid for n-type semiconductor [160]:

$$E_{CB} = V_{fb} + kTln({}^{N_D}/_{N_{CB}}) \ , \qquad (8)$$

where N_{CB} is the effective density of states in the conduction band. N_{CB} is calculated from the following **equation (9)** [161]:

$$N_{CB} = 2\sqrt{(\frac{2\pi m_e^* kT}{h^2})^3} \ , \qquad (9)$$

where $m_e^* = 1.1\ m_0$ (m_0 = ~9.1×10^{-31} Kg), and h is Planck's constant. The calculated value of N_{CB} is 3.0×10^{19} cm^{-3}. Therefore the calculated values, E_{CB} = -0.49 − -0.498 eV vs RHE.

Therefore, we infer that photoexcited electrons in the VB of BFCO can thermodynamically oxidate water to O_2. In addition, the donor density (N_D) estimated from the Mott–Schottky plot is 2.4×10^{21} cm^{-3} (from the slope of the line at 1 kHz).

On the basis of the aforementioned analysis, it is desirable to regulate the polarization state (depolarization electric field, E_{dp}) and migration of photogenerated holes, so as to obtain high-

efficiency oxygen-evolving multiferroic thin films based photoanodes. The tentative simplified energy band schematic illustrations are depicted in **Figures 66**(b)(c). After poling the BFCO thin film, the surface polarization charge causes band bending within the space charge region (SCR) associated with an electric field gradient. As the thickness of the films (~90 nm) is of the same order of magnitude as the width of SCR (≈ 20–50 nm, detailed calculations are provided in following), the influence of band bending at the interface can no longer be neglected.

Calculation of width (W) of the space charge region:

The width of the space charge can be estimated from the following **equation (10)** [162]:

$$W = \sqrt{\frac{2\varepsilon_0\,\varepsilon_r}{(eN_D)(\emptyset_{SC} - {}^{kT}/_{e})}} \quad , \qquad (10)$$

where Φ_{sc} (i.e. $V - V_{fb}$) is the potential drop across the space charge region. The calculated value of W is in the range of 20 to 50 nm with Φ_{sc} from 0.2 to 0.9 V (vs. RHE).

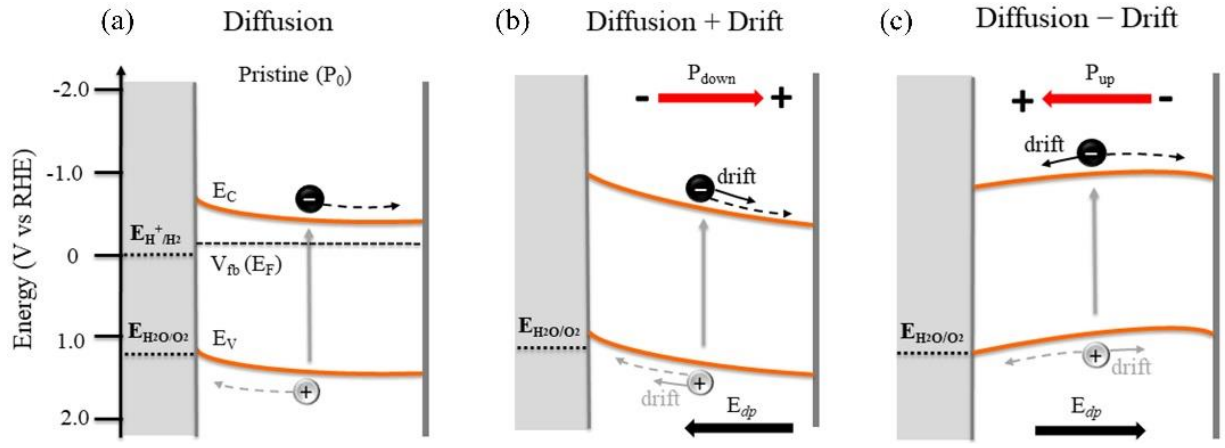

Figure 66. Simplified energy band diagrams of a PEC cell based on *n*-type BFCO in electrolyte at pristine state (a), and either polarization down (b) or polarization up (c).

For the negatively poled BFCO film, the energy band diagram is modified as illustrated in **Figure 66**(b). Under illumination, the photogenerated e^-/h^+ pairs will be separated by the driving

force arising from a E_{dp}, and the electrons in BFCO thin films will then be driven toward the BFCO/SRO interface, while the holes will migrate to the BFCO/electrolyte interface. Consequently, the recombination of photogenerated electrons and holes is effectively hindered, thereby leading to enhanced PEC performance. On the other hand, when the film is positively poled, the oppositely slanted band causes electrons to drift into the BFCO/electrolyte interface while the holes accumulate at the BFCO/SRO interface (**Figure 66**(c)). In this case, it is unfavorable for electron flow and reduces the PEC efficiency. So far, we have discussed the PEC properties of bare BFCO photoanodes and the tailoring of PEC performance by switching FE polarization.

7.4.2. Enhanced PEC performance of photoanodes coated with *p*-NiO layer

As mentioned the novel device architecture as before, the bare BFCO photoanodes coated with a transparent conducting *p*-type NiO thin films were employed to evaluate a PEC activity with assumed high efficiency. Thus, ~10 and 20 nm NiO films used as electron-blocking and protection layer were deposited on top of the bare BFCO photoanodes by PLD. **Figure 67**(a) shows a schematic diagram of the experimental setup used for the PEC measurements, and the proposed layout of NiO/BFCO/SRO heterojunction photoanode for water splitting shows that light is absorbed by BFCO thin films and the photogenerated holes transfer to the NiO, at which O_2 is produced. In the *J*-*V* curves, as shown in **Figure 67**(b), the 10 nm NiO/BFCO photoanodes achieved an anodic photocurrent density of +0.4 mA cm^{-2} at +1.23 V (vs. RHE) which is enhanced by 2-fold than that of 20 nm NiO/BFCO photoanode (+0.2 mA cm^{-2}), due to the large portion of incident photons entry to BFCO absorber (~70% optical transmission) compared with that of 20 nm NiO (~60%). The photocurrent density of 10 nm NiO/BFCO photoanodes is enhanced by 4-fold than that of the photoanode without NiO layer, and 5-fold than that of the typical perovskite

multiferroic oxide −$BiFeO_3$ thin films based photoanodes measured in 0.5 M Na_2SO_4 under one-sun illumination [110]. The onset potential for 20 nm and 10 nm NiO/BFCO photoanodes is −140 mV (vs. RHE). The onset-potential shift for photoanodes with and without NiO layer may be explainable as a consequence of a NiO/BFCO interfacial region formation with the presence of NiO/BFCO heterojunction, which would increase the voltage drop across the oxide layer. On exposing the electrode to illumination, the V_{oc} increased in thin NiO layer involved devices compared with the thick NiO layer involved devices (**Figure 67**(b), inset) due to the increase of electrical resistance at NiO/BFCO interfacial region, thus induced the reduction of photocurrent. All the obtained parameters of PEC performance for BFCO-based photoanodes without and with NiO layer are summarised in **Table 11**.

Table 11. PEC performance of photoanodes with/without the NiO layer under 1 sun.

Photoanodes		J (mA cm^{-2})	$\|P_{onset}\|$ (mV vs. RHE)	V_{fb} (V vs. RHE)
bare BFCO	P_0	0.10	70	-0.092 to -0.10
	P_{up}	0.06	30	−
	P_{down}	0.15	30	−
20 nm NiO/BFCO		0.20	140	−
10 nm NiO/BFCO		0.40	140	-0.06 to -0.04

The *J-t* analyses under chopped illumination for corresponding photoelectrodes at +0.6 V (vs. RHE) biasing potential are measured using the same method as before (not shown here). The *p*-NiO/*n*-BFCO heterojunction exhibits switching behavior under chopped illumination at forward biasing potential, while there is no switching behavior under the reversed biasing potential as there is no photocathodic behavior even a *p*-type NiO semiconductor introduced. The same calculation method of V_{fb} for NiO/BFCO heterojunction as our previous part doesn't show here. As shown in **Figure 67**(c), the value of V_{fb} was obtained to be −0.06 to −0.04 V (vs. RHE) for both frequencies

(1 and 2 kHz) extracting from *x*-axis intercept (V_0 = −0.03 to −0.01 V vs. RHE). The electron affinity and ionization potential for NiO thin films were determined by UPS measurements (not shown here) and the energy band alignment is depicted in **Figure 67**(d). Under illumination, the photon-generated electrons at the surface conduction band of BFCO will be driven toward the interfacial region of BFCO/SRO due to the internal electric fields induced driven force and the high conduction band minimum (CBM) of NiO which could block the electrons, while the holes will migrate to the NiO/electrolyte interface. Consequently, the recombination of photogenerated electrons and holes is effectively hindered, thereby leading to enhanced PEC performance than that of the bare BFCO photoanode.

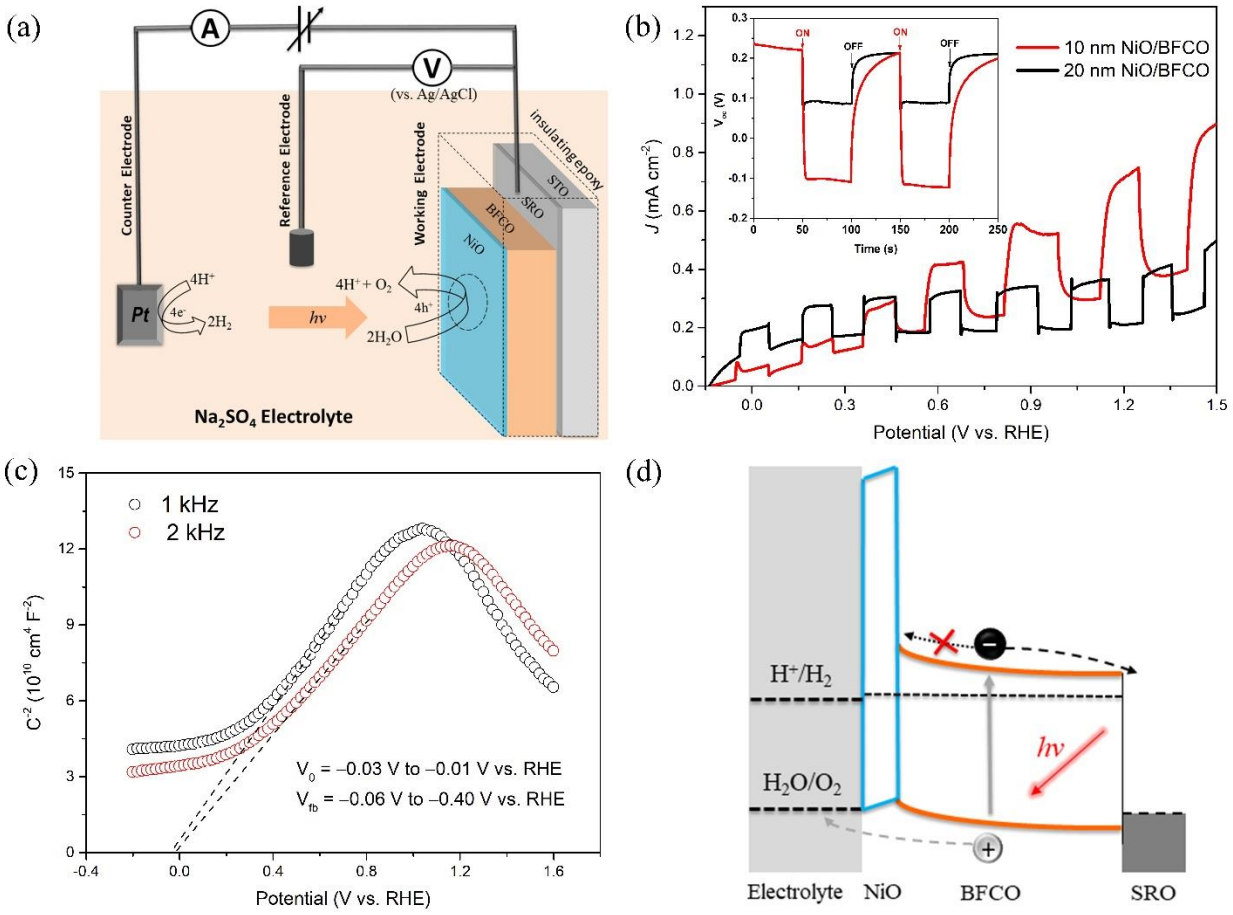

Figure 67. (a) A schematic diagram of the experimental setup used for the PEC measurements; and the proposed layout of NiO/BFCO/SRO heterojunction photoanode for water splitting shows that light is absorbed by BFCO thin films and the photogenerated holes transfer to the NiO, at which O_2 is produced; (b) *J-V* curves for the samples coated with 10 and 20 nm NiO layer under chopped light, respectively; Inset shows corresponding V_{oc} vs. time. (c) M-S measurements of NiO/BFCO at 0 V with 1 and 2 kHz. (d) Band alignment and charge transfer at the interfacial regions of electrolyte/NiO/BFCO.

7.5. Stability and Photon-to-current conversion efficiency

We analyzed the stability and efficiency of *p*−NiO/*n*−BFCO heterojunctions when they were employed as photoanodes. The stability test of the fabricated photoanodes were conducted using chronoamperometry at a potential of +0.9 V (vs. RHE) in Na_2SO_4 electrolyte under one sun illumination. As shown in **Figure 68**(a), the 10 nm NiO/BFCO heterojunction photoanode showed a slight initial decrease in photocurrent, then stabilized at a current density of ∼0.27 mA cm^{-2} for four hours of continuous operation. An insignificant change in morphology of the NiO/BFCO photoanode surface after four hours of continuous operation (cf. SEM image in inset of **Figure 68**(a)) evidences a reasonable mechanical stability of photoanodes. On the other hand, the photocurrent density of BFCO photoanodes without NiO protective layer under long-time irradiation in aqueous electrolyte declines by 34% within the first 5 minutes, followed by a further 20% decrease during the next 1 hour. The results could be explained by the presence of defects at the BFCO surface, among which oxygen vacancies (V_{O2}) or deficiency of metallic cations (i.e., V_{Fe}^{3+}, V_{Cr}^{3+}). These are associated with the growth of PLD-deposited BFCO crystals, behaving as charge carrier recombination sites that dramatically affect photocurrent generation.

Finally, we evaluated the photon-to-current conversion efficiency by two types of diagnostic figures of merit for PEC devices. The incident photon-to-current efficiency (IPCE) is

one of the most important means which describes the photocurrent collected per incident photon flux as a function of illumination wavelength. To measure the IPCE, we recorded the current−voltage measurements under specific radiation wavelengths (**Figure 68**(b)).

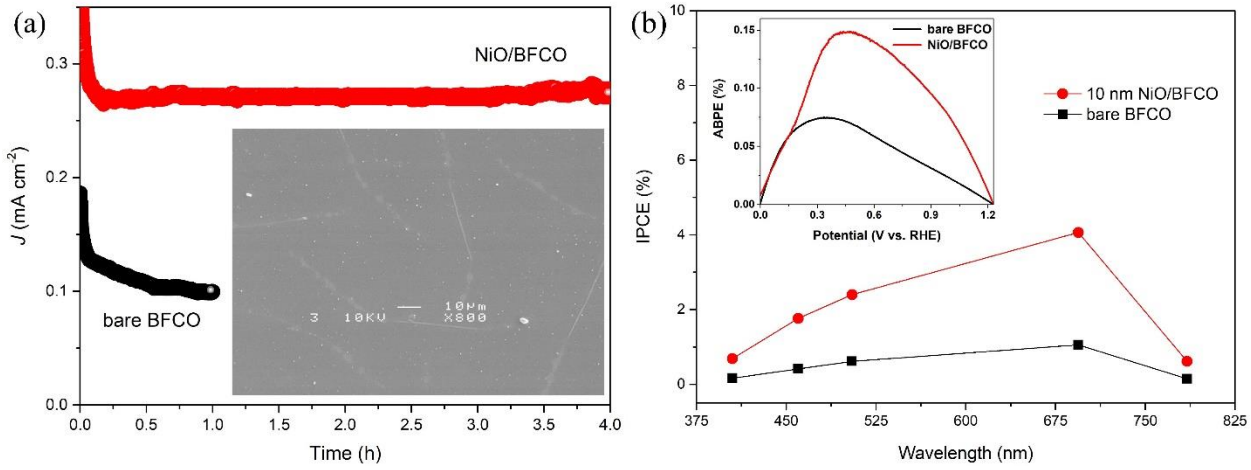

Figure 68. (a) Stability test of photoanodes with/without 10 nm thick-NiO layer at +0.9 V bias (vs. RHE) in 1 M Na_2SO_4 electrolyte under 1 sun illumination. The inset shows the SEM image to surface of NiO/BFCO photoanodes after stability tests of several hours. (b) IPCE spectra for BFCO-based photoanodes with/without 10 nm thick-NiO layer at 1.23 V (vs. RHE). The inset shows the corresponding ABPE as a function of applied potential.

To avoid band-to-band absorption in the SRO coated STO substrate (~387 nm) and promote the contribution from BFCO, the measurements were carried out by varying the incident wavelength from 405 to 785 nm. The calculation details of IPCE for both architectures of photoelectrodes were demonstrated by **equation (11)** [163]:

$$\mathrm{IPCE} = \frac{1239.8 \times |j_{ph}|}{P_{mono} \times \lambda} \times 100\%\,, \qquad (11)$$

where 1239.8 represents a multiplication of *h* (Planck's constant) and c (the speed of light) in V × nm; j_{ph} is the photocurrent density (mA cm^{-2}); P_{mono} is the calibrated and monochromated illumination power intensity (mW cm^{-2}) and λ is the wavelength (nm) at which this illumination

power is measured. The results indicate that the absorbed photons of different energies are successfully converted into photocurrents. In particular, the IPCE values are more pronounced in the wavelength range of 460 nm and 750 nm which is in agreement with the ellipsometric spectra (i.e., absorption coefficient α vs. wavelength), confirming the high photon to current conversion rate in the visible region of the solar spectrum at an external applied bias of 1.23 V vs. RHE. The high IPCE values are recorded in NiO/BFCO heterojunctions compared with bare BFCO, thus indicating a high photon-to-current conversion efficiency in NiO/BFCO due to the efficient charge separation and collection with low recombination rate of h^+/e^-. These IPCE values are also good agreement with the external quantum efficiency (EQE) for the NiO/BFCO heterojunction solar cells (see **Figure 60**). As a result, NiO/BFCO heterojunctions yield a higher photocurrent density than the bare BFCO photoanodes.

Furthermore, the application of a bias generally increases the current drawn from the device, however applying a bias that exceeds the thermodynamic water splitting potential (1.23 V vs. RHE) brings into question whether or not PEC under these conditions is more advantageous than standard electrolysis in the dark. We calculated the applied-bias photon-to-current efficiency (ABPE) from the current−voltage curves recorded under 1 sun illumination by applying external bias, as shown in the inset of **Figure 68**(b). For this assessment, an external bias (V_b) must be applied between the photoelectrode and counter electrode for small bandgap materials, such as our ordered BFCO (E_g≈1.8 eV). The calculation of ABPE extracted from photocurrent vs. potential curves was given by following **equation (12)** which is correct from thermodynamic perspective [163]:

$$ABPE = \left(\frac{|J_{ph}|\times(1.23-|V_b|)}{P_{light}}\right)\times 100\% \quad , \qquad (12)$$

where V_b is the applied voltage (V vs. RHE), J_{ph} is the photocurrent density (mA cm^{-2}) calculated by the difference of current density under light and dark conditions, and P_{light} is the power density of the illumination (100 mW cm^{-2} in this work). The observed maximum ABPE is ~0.15% for 10 nm NiO/BFCO photoanodes, 2-fold larger than that of 20 nm NiO/BFCO photoanodes. In the inset of **Figure 68**(b), the observed maximal ABPE is ~0.15% at 0.45 V (vs. RHE) for NiO/BFCO heterojunctions photoanodes, 2−fold larger than the bare BFCO-based devices at 0.35 V (vs. RHE). The shift of V_b at maximal ABPE is thought to originate from the increase of electrical resistance in NiO/BFCO heterostructures compared with the bare BFCO-based devices, which remains the same shifting as the onset-potential of BFCO photoanodes with/without NiO layer.

7.6. Summary

We have demonstrated that the *p*-NiO/*n*-BFCO heterojunction is an efficient and stable photoanode for water splitting. For comparison, the bare BFCO photoanodes with a small bandgap and large visible-light absorption coefficient exhibit a tailoring PEC properties by switching the FE polarization state of BFCO. This is particularly meaningful for smart applications of photoelectric power conversion or detection. More interestingly, the enhanced PEC performance and multihour stability were achieved by coating the bare BFCO photoanodes with a *p*-type, transparent, conductive, catalytically active metal oxide NiO layer. The 10 nm NiO/BFCO heterojunction photoanodes, compared with bare BFCO photoanodes, show a higher photocurrent density (0.40 mA cm^{-2} at 1.23 V vs. RHE), a low onset potential (−140 mV vs. RHE) and multihour stability with a higher photon-to-current efficiency.

Chapter 8. Conclusion and Perspectives

8.1. Conclusion

Firstly, we have successfully synthesised the *p*-type indium-doped strontium titanate (In-$SrTiO_3$, ISTO) epitaxial thin films with various indium concentration ($SrIn_xTi_{1-x}O_3$, $0 \leq x \leq 0.15$) in thickness of ~100 nm by using a hybrid system which combines PLD and MBE, and systematically investigated their structural, electrical and optical properties for future use as top electrode or/and window layer in solar energy conversion, especially photovoltaics.

The ISTO films epitaxially grown on single-crystalline (100)-oriented $LaAlO_3$ substrate exhibit a single phase, high crystal quality and atomically smooth surface. The ISTO films with In concentration in the range of 10 to 15% ($SrIn_xTi_{1-x}O_3$, $0.10 \leq x \leq 0.15$) grown under oxygen pressures between 10^{-4} and 1.0 mTorr show an optimal range of high optical transmission (>70%), large optical band gap (>3.2 eV), low electrical resistivity (10^{-2} Ω cm), high hole concentration of 3×10^{19} cm^{-3} and mobility of 5 cm^2/Vs. The hole conduction of *p*-type ISTO thin films was further confirmed by fabricating In-STO/Nb-STO (ISTO/NSTO) junctions. The homoepitaxial structure exhibits a turn-on voltage of ~2.67 V, in good agreement with the value (2.73 eV) determined from energy band alignment.

Secondly, we have fabricated a photodetector based on multiferroic BFCO epitaxial thin films, buffered with SRO layer by PLD, and evaluated its photodiode properties like *J-E*, transient photoresponse and responsivity.

PLD-deposited BFCO epitaxial thin films demonstrated a relative wide bandgap (≈2.5 eV, compared with highly-ordered BFCO, having a bandgap of 1.4−1.8 eV) with low Fe/Cr cationic ordering (R≈0.1%, compared with large R≈0.5−5.1%), and a large FE polarization (40 μC cm^{-2}).

The photodiodes exhibit a substantial photocurrent (in order of μA) at +0.3 V and a fast transient response (in the order of 10^{-2} s), attributed to the effective charge carrier separation and collection at the interfacial region of BFCO/SRO electrode. The tailoring of photoconductive performance (*J-E* curves) was achieved by tuning FE polarization state using negative/positive electric poling. Time-resolved photoluminescence (TRPL) decay measured at 500 nm wavelength demonstrated an ultrafast charge transfer (lifetime <10 ns) in BFCO/SRO heteroepitaxial junction which showed a maximum responsivity of 0.38 mA/W at 500 nm.

Thirdly, we reported the design and fabrication of a *p-i-n* heterojunction PV devices based on multiferroic BFCO epitaxial thin films by PLD. A *p*-type NiO thin film acting as electron-blocking/hole-transporting layer (EBL/HTL) and a typical *n*-type Nb-STO (NSTO) acting as electron-transporting layer (ETL) were used to form the double-interfaced heterojunction based on all-inorganic oxide, FE and perovskite materials.

BFCO epitaxial thin films grown at various parameters of PLD exhibited the E_g varied between 2.4−1.7 eV (corresponding R≈0.29−0.68%) and corresponding remnant FE polarization in range of 44−14 μC cm^{-2}. *J-V* characteristics for *p-i-n* heterojunction devices showed a 4−fold enhancement in power conversion efficiency, compared with *i-n* heterojunction devices, due to the enhanced driven force of separation of photogenerated carriers at two depletion regions formed at the *p-i* and *i-n* interfaces in *p-i-n* heterojunction, which are also confirmed by EIS measurements. A maximum photon-to-current efficiency of 32% at visible range for *p-i-n* heterojunction devices was observed in EQE spectra.

We have systematically investigated the mechanism of charge carrier separation, transport and collection in double-perovskite multiferroics based solar cells in *p-i-n* structure configuration,

and understood the complex relationships between structural, optical, electrical and FE properties of BFCO films, and how they affect PV performance of device.

Finally, we have fabricated a photoelectrode based on a *p*-NiO/*n*-BFCO heterojunction and evaluated its PEC performance for solar water oxidation, compared with a bared BFCO-based photoelectrode.

The *J*-*V* curves measurement of bared BFCO photoelectrode demonstrates a photoanodic behaviour, and enhanced photocurrent due to the effective charge transfer at BFCO/electrode interfacial region by switching the FE polarization state of BFCO. More important, a four-fold enhancement in photocurrent and multihour stability were achieved by coating the bare BFCO photoanodes with a *p*-type, transparent, conductive, catalytically active metal oxide−NiO. ~10 nm NiO/BFCO heterojunction photoanode showed a maximum photocurrent density of ~0.40 mA cm^{-2} at 1.23 V vs. RHE, low onset potential of −140 mV vs. RHE, a stability of performance over 4 hours, and a higher photon-to-current efficiency.

8.2. Perspectives

The versatility of double-perovskite multiferroic BFCO relating to the tunability of E_g, visible-light absorption coefficient (α), spontaneous FE polarization (*P*) and magnetization (*M*), and the chemically stable, environmental friendly nature, provides opportunities for multifunctional applications such as spintronics, optoelectrics, data storage, and solar energy conversion (i.e., photovoltaics, photodetectors, photocatalysis).

Further study perspectives are pointing out as following:

(1) Design and fabrication of highly-efficient BFCO-based multijunction cells.

We have fabricated the *p*-*i*-*n* heterojunction solar cells based on one-single BFCO intrinsic absorber layer sandwiched between *n*- and *p*-type semiconductor layers and investigated their PV

performance achieving a maximum efficiency of 2%. Based on our work, the three-junction or four-junction solar cells (e.g., triple layers of BFCO with different bandgaps for light absorption at various wavelengths) could be designed and fabricated in future study, such as NiO (MoO_3, etc.)/BFCO#1(large E_g)/BFCO#2(medium E_g)/BFCO#3(narrow E_g)/NSTO, etc.

(2) Synthesis and investigation on functional properties of nanostructured BFCO.

Numbers of attempts have been devoted to synthesize a double-perovskite, highly-ordered, single-crystalline BFCO by using PLD technique in form of thin film, whereas synthesis of BFCO crystals in nanostructures form by PLD (e.g., nanoplate, nanowire, nanoparticle, nanorod, nanoisland, etc.) has been seldom reported. These nanostructures typically demonstrate significant surface effect compared with PLD-deposited condensed BFCO continuous thin films, and thus permit to be promising in solar cells and solar water splitting.

(3) Further investigation on a novel 10-H hexagonal perovskite nanosheet in a Bi-Fe-Cr-O system.

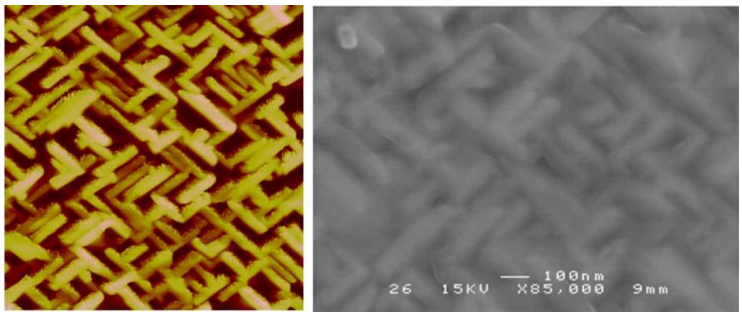

A novel 10-H hexagonal BFCO (P63/mmc space group) perovskite nanosheet is synthesized by PLD with a $SrTiO_3$ substrate pre-treatment: (1) etched by hydrogen fluoride (BHF) solution; (2) argon plasma treatment; (3) annealed at 900°C (1 hour) in flowing N_2 gas. The physical properties, such as optical, electrical, magnetic and ferroelectric properties, and the structure stability are expected to be further studied. This may open the feasibility to explore the multifunctionalities of this system. Figures show the AFM and SEM images of obtained novel hexagonal BFCO nanosheet.

Bibliography

1. J. Ravichandran, W. Siemons, H. Heijmerikx, M. Huijben, A. Majumdar, and R. Ramesh, *An Epitaxial Transparent Conducting Perovskite Oxide: Double-Doped $SrTiO_3$.* Chemistry of Materials, 2010, **22**(13), 3983.
2. H.L. Hartnagel, A.L. Dawar, A.K. Jain, and C. Jagadish, *Semiconducting Transparent Thin Films*. 1995, Bristol, UK: Institute Of Physics Publishing.
3. K. Bädeker, *Transparent Conducting CdO Films.* Annual Physics (Leipzig), 1907, **22**.
4. O. Tuna, Y. Selamet, G. Aygun, L. Ozyuzer, *High quality ITO thin films grown by dc and RF sputtering without oxygen.* Journal of Physics D: Applied Physics, 2010, **43**, 055402.
5. E. Elangovan and K. Ramamurthi, *A study on low cost-high conducting fluorine and antimony-doped tin oxide thin films.* Applied Surface Science, 2005, **249**(1), 183.
6. S.-M. Park, T. Ikegami, and K. Ebihara, *Effects of substrate temperature on the properties of Ga-doped ZnO by pulsed laser deposition.* Thin Solid Films, 2006, **513**(1), 90.
7. B.Z. Dong, H. Hu, G.J. Fang, X.Z. Zhao, D.Y. Zheng, and Y.P. Sun, *Comprehensive investigation of structural, electrical, and optical properties for ZnO:Al films deposited at different substrate temperature and oxygen ambient.* Journal of Applied Physics, 2008, **103**(7), 073711.
8. A. Biswas, N. Li, M.H. Jung, Y.W. Lee, J.S. Kim, and Y.H. Jeong, *La doped $SrTiO_3$ thin films on $SrLaAlO_4$ (001) as transparent conductor.* Journal of Applied Physics, 2013, **113**(18), 183711.
9. B.W. Huang, C.Y. Wen, G.W. Lin, P.Y. Chen, Y.H. Jiang, P.K. Kao, C.T. Chi, H. Chang, and J.Z. Chen, *Influence of Ca/Al Ratio on Properties of Amorphous/Nanocrystalline Cu–Al–Ca–O Thin Films.* Journal of the American Ceramic Society, 2015, **98**(1), 125.
10. F. Werfel and E. Minni, *Photoemission study of the electronic structure of Mo and Mo oxides.* Journal of Physics C: Solid State Physics, 1983, **16**(31), 6091.
11. H. Sato, T. Minami, S. Takata, and T. Yamada, *Transparent conducting p-type NiO thin films prepared by magnetron sputtering.* Thin Solid Films, 1993, **236**(1), 27.
12. K. Ueda, T. Hase, H. Yanagi, H. Kawazoe, H. Hosono, H. Ohta, M. Orita, and M. Hirano, *Epitaxial growth of transparent p-type conducting $CuGaO_2$ thin films on sapphire (001)*

substrates by pulsed laser deposition. Journal of Applied Physics, 2001, **89**(3), 1790.

13. M.D. Irwin, D.B. Buchholz, A.W. Hains, R.P.H. Chang, and T.J. Marks, *p-Type semiconducting nickel oxide as an efficiency-enhancing anode interfacial layer in polymer bulk-heterojunction solar cells.* Proceedings of the National Academy of Sciences, 2008, **105**(8), 2783.
14. H. Brune, *Surface and Interface Science: Solid-Solid Interfaces and Thin Films*. 2014, Weinheim, Germany: Wiley-VCH Verlag GmbH & Co. KGaA.
15. A. Jilani, M.S. Abdel-Wahab, and A.H. Hammad, *Modern Technologies for Creating the Thin-film Systems and Coatings*. Advance Deposition Techniques for Thin Film and Coating. 2017, Rijeka, Croatia: InTech.
16. J.R. Arthur, *Physical and Chemical Methods for Thin-Film Deposition and Epitaxial Growth*, in *Specimen Handling, Preparation, and Treatments in Surface Characterization*, 1998, Boston, MA, USA: Springer.
17. S.J. Bauer, *An apparent ionospheric response to the passage of hurricanes.* Journal of Geophysical Research, 1958, **63**(1), 265.
18. P.H. Le and C.W. Luo, *Thermoelectric and Topological Insulator Bismuth Chalcogenide Thin Films Grown Using Pulsed Laser Deposition*, in *Applications of Laser Ablation - Thin Film Deposition, Nanomaterial Synthesis and Surface Modification*, 2016, Rijeka, Croatia: InTech.
19. C.N.R. Rao, *Transition metal oxides.* Annual Review of Physical Chemistry, 1989, **40.1**, 291.
20. H.A. Jahn and E. Teller, *Stability of polyatomic molecules in degenerate electronic states.* Proceedings of the Royal Society of London A, 1937, **161**, 220.
21. C. Moure and O. Peña, *Recent advances in perovskites: Processing and properties.* Progress in Solid State Chemistry, 2015. **43**(4), 123.
22. Y.-H. Lee, J.-M. Wu, and C.-H. Lai, *Influence of La doping in multiferroic properties of $BiFeO_3$ thin films.* Applied Physics Letters, 2006, **88**(4), 042903.
23. V.A. Khomchenko, D.A. Kiselev, J.M. Vieira, A.L. Kholkin, M.A. Sá, and Y.G. Pogorelov, *Synthesis and multiferroic properties of $Bi_{0.8}A_{0.2}FeO_3$ (A=Ca,Sr,Pb) ceramics.* Applied Physics Letters, 2007, **90**(24), 242901.
24. H. Li, S. Liu, L. Chen, C. Li, and Z. Wang, *First-principles investigation of electronic and*

magnetic properties of double perovskite $CaFeTi_2O_6$. Physica E: Low-dimensional Systems and Nanostructures, 2015, **69**,133.

25. M.N. Iliev, M.M. Gospodinov, M.P. Singh, J. Meen, K.D. Truong, P. Fournier, and S. Jandl, *Growth, magnetic properties, and Raman scattering of La_2NiMnO_6 single crystals.* Journal of Applied Physics, 2009, **106**(2), 023515.
26. Y. Mao, J. Parsons, and J.S. McCloy, *Magnetic properties of double perovskite La_2BMnO_6 (B = Ni or Co) nanoparticles.* Nanoscale, 2013, **5**(11), 4720.
27. Y. Qian, H. Wu, E. Kan, J. Lu, R. Lu, Y. Liu, W. Tan, C. Xiao, and K. Deng, *Biaxial strain effect on the electronic and magnetic phase transitions in double perovskite La_2FeMnO_6: A first-principles study.* Journal of Applied Physics, 2013, **114**(6), 063713.
28. Z.-W. Song and B.-G. Liu, *Electronic structure and magnetic and optical properties of double perovskite Bi_2FeCrO_6 from first-principles investigation.* Chinese Physics B, 2013, **22**(4), 047506.
29. M.C. Knapp and P.M. Woodward, *A-site cation ordering in $AA'BB'O_6$ perovskites.* Journal of Solid State Chemistry, 2006, **179**(4), 1076.
30. R. Schmidt, E. Langenberg, J. Ventura, and M. Varela, *Bi containing multiferroic perovskite oxide thin films*, in *Perovskite: Crystallography, Chemistry and Catalytic Performance*, 2014, New York, USA: Nova Science Publishers, Inc.
31. D. Serrate, J.M. De Teresa, and M.R. Ibarra, *Double perovskites with ferromagnetism above room temperature.* Journal of Physics: Condensed Matter, 2007, **19**(2), 023201.
32. J. Valasek, *The early history of ferroelectricity.* Ferroelectrics, 1971, **2**, 239. R.E. Cohen, *Origin of ferroelectricity in perovskite oxides*. Nature, 1992, **358**, 136.
33. C.H. Ahn, K.M. Rabe, and J.-M. Triscone, *Ferroelectricity at the Nanoscale: Local Polarization in Oxide Thin Films and Heterostructures.* Science, 2004, **303**(5657), 488.
34. H. Han, Y. Kim, M. Alexe, D. Hesse, and W. Lee, *Nanostructured Ferroelectrics: Fabrication and Structure–Property Relations.* Advanced Materials, 2011, **23**(40), 4599.
35. J.F. Scott, *Applications of Modern Ferroelectrics.* Science, 2007, **315**(5814), 954.
36. Y.-M. Chiang, D.P. Birnie, and W.D. Kingery, *Physical Ceramics: Principles for Ceramic Science and Engineering*. 1997, New York, USA: John Wiley & Sons.
37. G.L. Miessler, D.A. Tarr, *Inorganic Chemistry, 2nd Edn*. 1999, New Jersey, USA: Prentice-Hall, Pearson.

38. J.D. FAN and Y.M. Malozovsky, Pauli Exclusion Principle. International Journal of Modern Physics B, 2013, **27**(15), 1362024.
39. T. Pruschke and N. Grewe, *The Anderson model with finite Coulomb repulsion.* Zeitschrift für Physik B: Condensed Matter, 1989, **74**(4), 439.
40. L. Berger, *Exchange interaction between ferromagnetic domain wall and electric current in very thin metallic films.* Journal of Applied Physics, 1984, **55**(6), 1954.
41. C. Blouzon, *Photoelectric and magnetic properties of multiferroic domain walls in $BiFeO_3$*, in *Physique en ile-de-France*. 2016, Université Pierre et Marie Curie: Ile de France, France.
42. B.D. Cullity and C.D. Graham, *Introduction to magnetic materials*. 2011, New Jersey, USA: John Wiley & Sons.
43. J.S. Miller, *Magnetically ordered molecule-based materials.* Chemical Society Reviews, 2011, **40**(6), 3266.
44. I. Žutić, J. Fabian, and S. Das Sarma, *Spintronics:Fundamentals and applications.* Reviews of Modern Physics, 2004, **76**(2), 323.
45. H. Schmid, *Multi-ferroic magnetoelectrics.* Ferroelectrics, 1994, **162**(1), 317.
46. J.F. Scott, *Data storage: Multiferroic memories.* Nature Materials, 2007, **6**(4), 256.
47. C.W. Nan, M.I. Bichurin, S. Dong, D. Viehland, and G. Srinivasan *Multiferroic magnetoelectric composites: Historical perspective, status, and future directions.* Journal of Applied Physics, 2008, **103**(3), 031101.
48. W. Eerenstein, N.D. Mathur, and J.F. Scott, *Multiferroic and magnetoelectric materials.* Nature, 2006, **442**(7104), 759.
49. F. Manfred, *Revival of the magnetoelectric effect.* Journal of Physics D: Applied Physics, 2005, **38**(8), R123.
50. M. Shariq, D. Kaur, V.S. Chandel, and M.A. Siddiqui, *Investigation on multiferroic properties of $BiFeO_3$ ceramics.* Materials Science-Poland, 2013, **31**(3), 471.
51. C.J. Howard, B.J. Campbell, H.T. Stokes, M. A. Carpenter, and R.I. Thomson, *Crystal and magnetic structures of hexagonal $YMnO_3$.* Acta Crystallographica, 2013, **B69**, 534.
52. M. Staruch, D. Violette, and M. Jain, *Structural and magnetic properties of multiferroic bulk $TbMnO_3$.* Materials Chemistry and Physics, 2013, **139**(2), 897.
53. S. Dong, J.M. Liu, S.W. Cheong, and Z. Ren, *Multiferroic materials and magnetoelectric physics: symmetry, entanglement, excitation, and topology.* Advances in Physics, 2015,

64(5-6), 519.

54. H. Béa, M. Gajek, M. Bibes, and A. Barthélémy, *Spintronics with multiferroics.* Journal of Physics: Condensed Matter, 2008, **20**(43), 434221.
55. R. Nechache, C. Harnagea, A. Pignolet, F. Normandin, T. Veres, L.P. Cargnan, and D. Ménard, *Growth, structure, and properties of epitaxial thin films of first-principles predicted multiferroic Bi_2FeCrO_6.* Applied Physics Letters, 2006, **89**(10), 102902.
56. R. Nechache, C. Harnagea, L.P. Carignan, O. Gautreau, L. Pintilie, M.P. Singh, D. Ménard, P. Fournier, M. Alexe, and A. Pignolet, *Epitaxial thin films of the multiferroic double perovskite Bi_2FeCrO_6 grown on (100)-oriented $SrTiO_3$ substrates: Growth, characterization, and optimization.* Journal of Applied Physics, 2009, **105**(6), 061621.
57. F. Bai, L. Shi, H. Zhang, Z. Zhong, W. Wang, and D. He, *Multiferroic properties of La-doped Bi_2FeCrO_6 prepared by high-pressure synthesis.* Journal of Applied Physics, 2012, **111**(7), 07C702.
58. S. Lv, M. Saito, Z. Wang, C. Chen, S. Chakraverty, M. Kawasaki, and Y. Ikuhara, *Atomic-scale structure and electronic property of the $La_2FeCrO_6/SrTiO_3$ interface.* Journal of Applied Physics, 2013, **114**(11), 113705.
59. R. Nechache, W. Huang, S. Li, and F. Rosei, *Photovoltaic properties of Bi_2FeCrO_6 films epitaxially grown on (100)-oriented silicon substrates.* Nanoscale, 2016, **8**(6), 3237.
60. D.H. Kim, H.N. Lee, M.D. Biegalski, and H.M. Christen, *Large ferroelectric polarization in antiferromagnetic $BiFe_{0.5}Cr_{0.5}O_3$ epitaxial films.* Applied Physics Letters, 2007, **91**(4), 042906.
61. M.R. Suchomel, C.I. Thomas, M. Allix, M.J. Rosseinsky, A.M. Fogg, and M.F. Thomas, *High pressure bulk synthesis and characterization of the predicted multiferroic $Bi(Fe_{1/2}Cr_{1/2})O_3$.* Applied Physics Letters, 2007, **90**(11), 112909.
62. S. Kamba, D. Nuzhnyy, R. Nechache, K. Závěta, D. Nižňanský, E. Šantavá, C. Harnagea, and A. Pignolet, *Infrared and magnetic characterization of multiferroic Bi_2FeCrO_6 thin films over a broad temperature range.* Physical Review B, 2008, **77**(10), 104111.
63. R. Nechache and F. Rosei, *Recent progress in nanostructured multiferroic Bi_2FeCrO_6 thin films.* Journal of Solid State Chemistry, 2012, **189**, 13.
64. R. Nechache, C. Harnagea, S. Li, L. Cardenas, W. Huang, J. Chakrabartty, and F. Rosei, *Bandgap tuning of multiferroic oxide solar cells.* Nature Photonics, 2015, **9**(1), 61.

65. S. Li, B. AlOtaibi, W. Huang, Z. Mi, N. Serpone, R. Nechache, and F. Rosei, *Epitaxial Bi_2FeCrO_6 Multiferroic Thin Film as a New Visible Light Absorbing Photocathode Material.* Small, 2015, **11**(32), 4018.
66. J.B. Goodenough, *Theory of the Role of Covalence in the Perovskite-Type Manganites [La,M(II)]MnO_3.* Physical Review, 1955, **100**(2), 564.
67. J. Kanamori, *Superexchange interaction and symmetry properties of electron orbitals.* Journal of Physics and Chemistry of Solids, 1959, **10**(2), 87.
68. B.W. Lee, P.S. Yoo, V.B. Nam, K.R.N. Toreh, and C.U. Jung, *Magnetic and electric properties of stoichiometric $BiMnO_3$ thin films.* Nanoscale Research Letters, 2015, **10**(1), 47.
69. Y. Yoneda and W. Sakamoto, *Electronic and local structures of $BiFeO_3$ films.* Journal of Physics: Condensed Matter, 2011, **23**(1), 015902.
70. P. Baettig, C. Ederer, and N.A. Spaldin, *First principles study of the multiferroics $BiFeO_3$, Bi_2FeCrO_6 and $BiCrO_3$: Structure, polarization, and magnetic ordering temperature.* Physical Review B, 2005, **72**(21), 214105.
71. R. Nechache, C. Harnagea, S. Licoccia, E. Traversa, A. Ruediger, A. Pignolet, and F. Rosei, *Photovoltaic properties of Bi_2FeCrO_6 epitaxial thin films.* Applied Physics Letters, 2011, **98**(20), 202902.
72. K. Sayama and R. Saitou, *Achievement of the World's Highest Efficiency in Hydrogen Production by Water Electrolysis using an Oxide Photoelectrode*. 2012, Available from: http://www.aist.go.jp/aist_e/list/latest_research/2012/20120511/20120511.html.
73. G.W. Crabtree and N.S. Lewis, *Solar energy conversion.* Physics Today, 2007, **60**(3), 37.
74. *Kennlinie Photodiode: Gregor Hess*. 2011: Wikipedia.
75. *Physics and Radio Electronics-Semiconductor diodes-Photodiode*. Available from: http://www.physics-and-radio-electronics.com/electronic-devices-and-circuits/semiconductor-diodes/photodiodesymboltypes.html.
76. W.K. Cheah, W.J. Fan, S.F. Yoon, D.H. Zhang, B.K. Ng, W.K. Loke, R. Liu, and A.T.S. Wee, *GaAs-based heterojunction p-i-n photodetectors using pentanary InGaAsNSb as the intrinsic layer.* IEEE Photonics Technology Letters, 2005, **17**(9), 1932.
77. H. Deok Yang, Y.H. Kil. J.H. Yang, S. Kang, T. Soo Teong, C.J. Choi, T. Sung Kim, and K.H. Shim, *Characterization of n-Ge/i-Ge/p-Si PIN photo-diode.* Materials Science in

Semiconductor Processing, 2014, **22**, 37.

78. C. Soci, A. Zhang, B. Xiang, S.A. Dayeh, D.P.R. Aplin, J. Park, X.Y. Bao, Y.H. Lo, and D. Wang, *ZnO Nanowire UV Photodetectors with High Internal Gain.* Nano Letters, 2007, **7**(4), 1003.
79. J. Zou, Q. Zhang, K. Huang, and N. Marzari, *Ultraviolet Photodetectors Based on Anodic TiO_2 Nanotube Arrays.* The Journal of Physical Chemistry C, 2010, **114**(24), 10725.
80. J. Xing, E. Guo, J. Dong, H. Hao, Z. Zheng, and C. Zhao, *High-sensitive switchable photodetector based on $BiFeO_3$ film with in-plane polarization.* Applied Physics Letters, 2015, **106**(3), 033504.
81. *Principle of Electricity Generation by Photovoltaic Cells*. Available from: http://www.apec-vc.or.jp/e/modules/tinyd00/?id=74.
82. C. Joyprokash, R. Nechache, C. Harnagea, S. Li, and F. Rosei, *Enhanced photovoltaic properties in bilayer $BiFeO_3$/Bi-Mn-O thin films.* Nanotechnology, 2016, **27**(21), 215402.
83. H. Heriche, I. Bouchama, N. Bouarissa, Z. Rouabah, and A. Dilmi, *Enhanced efficiency of $Cu(In,Ga)Se_2$ solar cells by adding $Cu_2ZnSn(S,Se)_4$ absorber layer.* Optik - International Journal for Light and Electron Optics, 2017, **144**, 378.
84. R. Zia, F. Saleemi, S. Naseem, and Z. Kayani, *Study the efficiency of single crystal CdTe/ZnCdS solar cell at various temperatures and illumination levels.* Energy Reports, 2015, **1**, 58.
85. S. Moon, K. Kim, Y. Kim, J. Heo, and J. Lee, *Highly efficient single-junction GaAs thin-film solar cell on flexible substrate.* Scientific Reports, 2016, **6**, 30107.
86. E. Wesoff, *First Solar Hits Record 22.1% Conversion Efficiency for CdTe Solar Cell*. 2016, Available from: https://www.greentechmedia.com/articles/read/first-solar-hits-record-22-1-conversion-efficiency-for-cdte-solar-cell.
87. Photovoltaics−NREL, *Best Research Cell Efficiencies*. Available from: https://www.nrel.gov/pv/.
88. F.-J. Haug, *Efficiency limits of photovoltaic energy conversion*. Available from: http://www.superstrate.net/pv/limit/.
89. W. Shockley and H.J. Queisser, *Detailed Balance Limit of Efficiency of p-n Junction Solar Cells.* Journal of Applied Physics, 1961, **32**(3), 510.
90. A. McEvoy, T. Markvart and L. Castaner, *Practical handbook of photovoltaics:*

fundamentals and applications. 2003, Waltham, MA, USA: Elsevier.

91. W. Ji, K. Yao, and Y.C. Liang, *Bulk Photovoltaic Effect at Visible Wavelength in Epitaxial Ferroelectric $BiFeO_3$ Thin Films.* Advanced Materials, 2010, **22**(15), 1763.
92. K. Yao, *Nanoscale ferroelectric thin films show promise for solar cells*. 2010, Available from:http://spie.org/newsroom/2927-nanoscale-ferroelectric-thin-films-show-promise-for-solar-cells.
93. S.Y. Yang, J. Seidel, S.J. Byrnes, P. Shafer, C.H. Yang, M.D. Rossell, P. Yu, Y.H. Chu, J.F. Scott, J.W. Ager, L.W. Martin, and R. Ramesh, *Above-bandgap voltages from ferroelectric photovoltaic devices.* Nature Nanotechnology, 2010, **5**(2), 143.
94. M.G. Kibria, F.A. Chowdhury, S. Zhao, B. AlOtaibi, M.L. Trudeau, H. Guo, and Z. Mi, *Visible light-driven efficient overall water splitting using p-type metal-nitride nanowire arrays.* Nature Communications, 2015, **6**, 6797.
95. L. Jin, B. AlOtaibi, D. Benetti, S. Li, H. Zhao, Z. Mi, A. Vomiero, and F. Rosei, *Near-Infrared Colloidal Quantum Dots for Efficient and Durable Photoelectrochemical Solar-Driven Hydrogen Production.* Advanced Science, 2016, **3**(3), 1500345.
96. W. Yang, Y. Yu, M.B. Starr, X. Yin, Z. Li, A. Kvit, S. Wang, P. Zhao, and X. Wang, *Ferroelectric Polarization-Enhanced Photoelectrochemical Water Splitting in TiO_2–$BaTiO_3$ Core–Shell Nanowire Photoanodes.* Nano Letters, 2015, **15**(11), 7574.
97. R. Abe, *Recent progress on photocatalytic and photoelectrochemical water splitting under visible light irradiation.* Journal of Photochemistry and Photobiology C: Photochemistry Reviews, 2010, **11**(4), 179.
98. S.W. Boettcher, E.L. Warreen, M.C. Putnam, E.A. Santori, D. Turner-Evans, M.D. Kelzenberg, M.G. Walter, J.R. Mckone, B.S. Brunschwig, H.A. Atwater, and N.S. Lewis, *Photoelectrochemical Hydrogen Evolution Using Si Microwire Arrays.* Journal of the American Chemical Society, 2011, **133**(5), 1216.
99. M.H. Lee, K. Takei, J. Zhang, R. Kapadia, M. Zheng, Y.Z. Chen, J. Nah, T.S. Mattews, Y.L. Chueh, J.W. Ager, and A. Javey, *p-Type InP Nanopillar Photocathodes for Efficient Solar-Driven Hydrogen Production.* Angewandte Chemie International Edition, 2012, **51**(43), 10760.
100. C. Liu, N.P. Dasgupta, and P. Yang, *Semiconductor Nanowires for Artificial Photosynthesis.* Chemistry of Materials, 2014, **26**(1), 415.

101. Z. Zhang and J.T. Yates, *Band Bending in Semiconductors: Chemical and Physical Consequences at Surfaces and Interfaces.* Chemical Reviews, 2012, **112**(10), 5520.

102. S. Li, *Synthesis and Functional Properties of $BiFeO_3$ and Bi_2FeCrO_6 based Nanostructures and Thin Films*. 2014, EMT-Institut National de la Recherche Scientifique(INRS).

103. S.R. Basu, L.W. Martin, Y.H. Chu, M. Gajek, R. Ramesh, R.C. Rai, X. Xu, and J.L. Musfeldt, *Photoconductivity in $BiFeO_3$ thin films.* Applied Physics Letters, 2008, **92**(9), 091905.

104. I. Yun, *Photodiodes - From Fundamentals to Applications*. 2012, Rijeka, Croatia: InTech.

105. D. Shao, M. Yu, J. Lian, and S. Sawyer, *Heterojunction photodiode fabricated from multiwalled carbon nanotube/ZnO nanowire/p-silicon composite structure.* Applied Physics Letters, 2013, **102**(2), 021107.

106. A. Anshul, H. Borkar, P. Singh, P. Pal, S.S. Kushvaha, and A. Kumar, *Photoconductivity and photo-detection response of multiferroic bismuth iron oxide.* Applied Physics Letters, 2014, **104**(13), 132910.

107. S.Y. Yang, L.W. Martin, S.J. Byrnes, T.E. Conry, S.R. Basu, D. Paran, L. Reichertz, J. Ihlefeld, C. Adamo, A. Melville, Y.H. Chu, C.H. Yang, J.L. Musfeldt, D.G. Schlom, J.W. Ager, and R. Ramesh, *Photovoltaic effects in $BiFeO_3$.* Applied Physics Letters, 2009, **95**(6), 062909.

108. G. Zhang, H. Wu, G. Li, Q. Huang, C. Yang, F. Huang, F. Liao, and J. Lin, *New high T_c multiferroics $KBiFe_2O_5$ with narrow band gap and promising photovoltaic effect.* 2013, **3**,1265.

109. C. Wang, D. Cao, F. Zheng, W. Dong, L. Fang, X. Su, and M. Shen, *Photocathodic behavior of ferroelectric $Pb(Zr,Ti)O_3$ films decorated with silver nanoparticles.* Chemical Communications, 2013, **49**(36), 3769.

110. J. Song, T.L. Kim, J. Lee, S.Y. Cho, J. Cha, S.Y. Joeng, H. An, W.S. Kim, Y.S. Jung, J. Park, G.Y. Jung, D.Y. Kim, J.Y. Jo, S.D. Bu, H.W. Jang, and S. Lee, *Domain-engineered $BiFeO_3$ thin-film photoanodes for highly enhanced ferroelectric solar water splitting.* Nano Research, 2017.

111. S. Li, J. Zhang, B.P. Zhang, W. Huang, C. Harnagea, R. Nechache, L. Zhu, S. Zhang, Y.H. Lin, L. Ni, Y.H. Sang, H. Liu, and F. Rosei, *Manipulation of charge transfer in vertically aligned epitaxial ferroelectric $KNbO_3$ nanowire array photoelectrodes.* Nano Energy, 2017,

35, 92.

112. W. Huang, R. Nechache, S. Li, M. Chaker, and F. Rosei, *Electrical and Optical Properties of Transparent Conducting p-Type $SrTiO_3$ Thin Films.* Journal of the American Ceramic Society, 2016, **99**(1), 226.

113. W. Huang, C. Harnagea, D. Benetti, M. Chaker, F. Rosei, and R. Nechache, *Multiferroic Bi_2FeCrO_6 based p-i-n heterojunction photovoltaic devices.* Journal of Materials Chemistry A, 2017, **5**(21), 10355.

114. *Molecular beam epitaxy (MBE)*, Zeljkovic lab, 2015, Available from: http://capricorn.bc.edu/wp/zeljkoviclab/research/molecular-beam-epitaxy-mbe/.

115. K. Wang, *Laser Based Fabrication of Graphene*, in *Advances in Graphene Science*, Chapter 4, M. Aliofkhazraei, Editor. 2013, Rijeka: InTech.

116. E. Robert, *Pulsed laser deposition of thin films: applications-led growth of functional materials*. 2007, New Jersey, USA: John Wiley & Sons, Inc.

117. M. Kubo, Y. Oumi, R. Miura, A. Stirling, A. Miyamoto, M. Kawasaki, M. Yoshimoto, H. Koinuma, *Atomic control of layer-by-layer epitaxial growth on $SrTiO_3$ (100) Molecular-dynamics simulations.* Physical Review B, 1997, **56**(20), 13535.

118. H. Wang, F. Chen, S. Dai,T. Zhao, H. Lu, D. Cui, Y. Zhou, Z. Chen, and G. Yang, *Sb-doped $SrTiO_3$ transparent semiconductor thin films.* Applied Physics Letters, 2001, **78**(12), 1676.

119. T. Zhao, H. Lu, F. Chen, S. Dai, G. Yang, and Z. Chen, *Highly conductive Nb doped $SrTiO_3$ epitaxial thin films grown by laser molecular beam epitaxy.* Journal of Crystal Growth, 2000, **212**(3), 451.

120. H. Tabata and T. Kawai, *Dielectric properties of strained (Sr,Ca)TiO_3/(Ba,Sr)TiO_3 artificial lattices.* Applied Physics Letters, 1997, **70**(3), 321.

121. N. Shanthi and D.D. Sarma, *Electronic structure of electron doped $SrTiO_3$: $SrTiO_{3-\delta}$ and $Sr_{1-x}La_xTiO_3$.* Physical Review B, 1998, **57**(4), 2153.

122. E.J. Cukauskas, S.W. Kirchoefer, W.J. Desisto, and J.M. Pond, *$Ba_{(1-x)}Sr_xTiO_3$ thin films by off-axis cosputtering $BaTiO_3$ and $SrTiO_3$.* Applied Physics Letters, 1999, **74**(26), 4034.

123. M. Choi, A.B. Posadas, C.A. Rodriguez, A. O'Hara, H. Seinige, A.J. Kellock, M.M. Frank, M. Tsoi, S. Zollner, V. Narayanan, and A.A. Demkov, *Structural, optical, and electrical properties of strained La-doped $SrTiO_3$ films.* Journal of Applied Physics, 2014, **116**(4), 043705.

124. L. Zhao, L. Fang, W. Dong, F. Zheng, M. Shen, and T. Wu, *Effect of charge compensation on the photoelectrochemical properties of Ho-doped $SrTiO_3$ films.* Applied Physics Letters, 2013, **102**(12), 121905.

125. M. Markovich, J. Roqueta, J. Santiso, E. Lakin, E. Zolotoyabko, and A. Rothschild, *Epitaxial growth of Nb-doped $SrTiO_3$ films by pulsed laser deposition.* Applied Surface Science, 2012, **258**(23), 9496.

126. S. Dai, H. Lu, F. Chen, Z. Chen, Z. Ren, and D.H.L. Ng, *In-doped $SrTiO_3$ ceramic thin films.* Applied Physics Letters, 2002, **80**(19), 3545.

127. H. Kato, T. Okumura, E. Sakai, H. Kumigashira, and T. Higuchi, *Hole and Ion Conductions of Sc-Doped $SrTiO_3$ Thin Film Prepared by RF Magnetron Sputtering.* Transactions of the Materials Research Society of Japan, 2012, **37**(4), 571.

128. K. Iwashina and A. Kudo, *Rh-Doped $SrTiO_3$ Photocatalyst Electrode Showing Cathodic Photocurrent for Water Splitting under Visible-Light Irradiation.* Journal of the American Chemical Society, 2011, **133**(34), 13272.

129. H. Guo, L. Liu, Y. Fei, W. Xiang, H. Lü, S. Dai, Y. Zhou, and Z. Chen, *Optical properties of p-type In-doped $SrTiO_3$ thin films.* Journal of Applied Physics, 2003, **94**(7), 4558.

130. A.R. Denton and N.W. Ashcroft, *Vegard's law.* Physical Review A, 1991, **43**(6), 3161.

131. T. Fix, R. Bali, N. Stelmashenko, and M.G. Blamire, *Influence of the dopant concentration in In-doped $SrTiO_3$ on the structural and transport properties.* Solid State Communications, 2008, **146**(9), 428.

132. J. Tauc, *Optical properties and electronic structure of amorphous Ge and Si.* Materials Research Bulletin, 1968, **3**(1), 37.

133. L.J. Meng, and M.P. dos Santos, *Investigations of titanium oxide films deposited by d.c. reactive magnetron sputtering in different sputtering pressures.* Thin Solid Films, 1993, **226**(1), 22.

134. N.A. Hill, *Density Functional Studies of Multiferroic Magnetoelectrics.* Annual Review of Materials Research, 2002, **32**(1), 01.

135. B. Zhou, L. Xiao, T.J. Li, J. Zhao, Z. Lai, and S. Gu, *Absorption redshift in TiO_2 ultrafine particles with surfacial dipole layer.* Applied Physics Letters, 1991, **59**(15), 1826.

136. W. Xu, J. Yang, W. Tang, Y. Zhang, and X. Tang, *Oxygen vacancy induced photoluminescence and ferromagnetism in $SrTiO_3$ thin films by molecular beam epitaxy.*

Journal of Applied Physics, 2013, **114**(15), 154106.

137. T. Choi, S. Lee, Y.J. Choi, V. Kiryukhin, and S.W. Cheong, *Switchable Ferroelectric Diode and Photovoltaic Effect in $BiFeO_3$.* Science, 2009, **324**(5923), 63.
138. P. Maksymovych, S. Jesse, P. Yu, R. Ramesh, A.P. Baddorf, and S.V. Kalinin, *Polarization Control of Electron Tunneling into Ferroelectric Surfaces.* Science, 2009, **324**(5933),1421.
139. A. Moliton and J.M. Nunzi, *How to model the behaviour of organic photovoltaic cells.* Polymer International, 2006, **55**(6), 583.
140. A.W. Hains, A.B.F. Martinson, M.D. Irwin, H. Yan, and T.J. Marks, *Bulk-heterojunction organic solar cells: Interfacial engineering routes to increased open-circuit voltage and power conversion efficiency.* Polymer Materials Science Engineering, 2007, **96**, 814.
141. P. Baettig and N.A. Spaldin, *Ab initio prediction of a multiferroic with large polarization and magnetization.* Applied Physics Letters, 2005, **86**(1), 012505.
142. T. Arima, Y. Tokura, J.B. Torrance, *Variation of optical gaps in perovskite-type 3d transition-metal oxides.* Physical Review B, 1993, **48**(23), 17006.
143. R. Zimmermann, P. Steiner, R. Claessen, F. Reinert, S. Hüfner, P. Blaha and P. Dufek, *Electronic structure of 3d-transition-metal oxides: on-site Coulomb repulsion versus covalency.* Journal of Physics: Condensed Matter, 1999, **11**(7), 1657.
144. H. Dong, C. Chen, S. Wang, W. Duan, and J. Li, *Elastic properties of tetragonal $BiFeO_3$ from first-principles calculations.* Applied Physics Letters, 2013, **102**(18), 182905.
145. H.L. Liu, M.K. Lin, Y.R. Cai, C.K. Tung, and Y.H. Chu, *Strain modulated optical properties in $BiFeO_3$ thin films.* Applied Physics Letters, 2013, **103**(18), 181907.
146. A. Vailionis, H. Boschker, W. Siemons, E.P. Houwman, D.H.A. Blank, G. Rijinders, and G. Koster, *Misfit strain accommodation in epitaxial ABO_3 perovskites: Lattice rotations and lattice modulations.* Physical Review B, 2011, **83**(6), 064101.
147. A. Ohtomo, S. Chakraverty, H. Mashiko, T. Oshima, and M. Kawasaki, *Spontaneous atomic ordering and magnetism in epitaxially stabilized double perovskites.* Journal of Materials Research, 2013, **28**(5), 689.
148. J.H. Park, J. Seo, S. Park, S.S. Shin, Y.C. Kim, N.J. Jeon, H.W. Shin, T.K. Ahn, J.H. Noh, S.C. Yoon, C.S. Hwang, and S.I. Seok, *Efficient $CH_3NH_3PbI_3$ Perovskite Solar Cells Employing Nanostructured p-Type NiO Electrode Formed by a Pulsed Laser Deposition.* Advanced Materials, 2015, **27**(27), 4013.

149. L. Wang, H. Ma, L. Chang, C. Ma, G. Yuan, J. Wang, and T. Wu, *Ferroelectric $BiFeO_3$ as an Oxide Dye in Highly Tunable Mesoporous All-Oxide Photovoltaic Heterojunctions.* Small, 2017, **13**, 1602355.

150. M. Alexe and D. Hesse, *Tip-enhanced photovoltaic effects in bismuth ferrite.* Nature Communications, 2011, **2**, 256.

151. S. Chatterjee, A. Bera, and A.J. Pal, *p–i–n Heterojunctions with $BiFeO_3$ Perovskite Nanoparticles and p- and n-Type Oxides: Photovoltaic Properties.* ACS Applied Materials & Interfaces, 2014, **6**(22), 20479.

152. K. Sun, M.T. McDowell, A.C. Nielander, S. Hu, M.R. Shaner, F. Yang, B.S. Brunschwing, and N.S. Lewis, *Stable Solar-Driven Water Oxidation to O_2(g) by Ni-Oxide-Coated Silicon Photoanodes.* The Journal of Physical Chemistry Letters, 2015, **6**(4), 592.

153. J. Li and N. Wu, *Semiconductor-based photocatalysts and photoelectrochemical cells for solar fuel generation: a review.* Catalysis Science & Technology, 2015, **5**(3), 1360.

154. Q. Yu, X. Meng, T. Wang, P. Li, and J. Ye, *Hematite Films Decorated with Nanostructured Ferric Oxyhydroxide as Photoanodes for Efficient and Stable Photoelectrochemical Water Splitting.* Advanced Functional Materials, 2015, **25**(18), 2686.

155. F. Wu, Y. Yu, H. Yang, L.N. German, Z. Li, J. Chen, W. Yang, L. Huang, W. Shi, L. Wang, and X. Wang, *Simultaneous Enhancement of Charge Separation and Hole Transportation in a TiO_2–$SrTiO_3$ Core–Shell Nanowire Photoelectrochemical System.* Advanced Materials, 2017, **29**(28), 1701432.

156. R. Wick and S.D. Tilley, *Photovoltaic and Photoelectrochemical Solar Energy Conversion with Cu_2O.* The Journal of Physical Chemistry C, 2015, **119**(47), 26243.

157. V. Patil, J. Pradeep, C. Manik, C. Manik, and S. Shashwati, *Synthesis and Characterization of Co_3O_4 Thin Film.* Soft Nanoscience Letters, 2012, **2**(1), 01.

158. P. Zhai, Q. Yi, J. Jian, H. Wang, P. Song, C. Dong, X. Lu, Y. Sun, J. Zhao, X. Dai, Y. Lou, H. Yang, and G. Zou, *Transparent p-type epitaxial thin films of nickel oxide.* Chemical Communications, 2014, **50**(15), 1854.

159. W.P. Gomes, F. Cardon, *Electron energy levels in semiconductor electrochemistry.* Progress in Surface Science, 1982, **12**, 155.

160. D.E. Scaife, *Oxide semiconductors in photoelectrochemical conversion of solar energy.* Solar Energy, 1980, **25**, 41.

161. E.Y. Tsymbal, A. Gruverman, V. Garcia, M. Bibes, A. Barthélémy, *Ferroelectric and multiferroic tunnel junctions*, MRS Bulletin, 2012, **37**, 138.

162. R. van de Krol and M. Grätzel, *Photoelectrochemical Hydrogen Production*. 2012, **102**, Berlin, Germany: Springer.

163. L. Ji, M.D. McDaniel, S. Wang, A.B. Posadas, X. Li, H. Huang, J.C. Lee, A.A. Demkov, A.J. Bard, J.G. Ekerdt, and E.T. Yu, *A silicon-based photocathode for water reduction with an epitaxial $SrTiO_3$ protection layer and a nanostructured catalyst.* Nature Nanotechnology, 2015, **10**(1), 84.

Appendix A

List of Acronyms

FE	Ferroelectric
TCOs	Transparent Conducting Oxides
BFO	$BiFeO_3$
BFCO	Bi_2FeCrO_6
ITO	Tin-doped Indium Oxide
STO	$SrTiO_3$
SRO	$SrRuO_3$
NSTO	Nb-doped $SrTiO_3$
LAO	$LaAlO_3$
PLD	Pulsed Laser Deposition
RHEED	Reflection High-Energy Electron Diffraction
MBE	Molecular Beam Epitaxy
PV	Photovoltaic
PEC	Photoelectrochemical
FESC	Ferroelectric Solar Cell
BPVE	Bulk Photovoltaic Effect
PCE	Power Conversion Efficiency
AFM	Atomic Force Microscopy
PFM	Piezoresponse Force Microscopy
XRD	X-Ray Diffraction
XRR	X-ray Reflection
RSM	Reciprocal Space Maps
XPS	X-ray Photoelectron Spectrometry
UPS	Ultraviolet Photoelectron Spectroscopy
PL	Photoluminescence
TRPL	Time-Resolved Photoluminescence
EQE	External Quantum Efficiency

EIS	Electrochemical Impedance Spectroscopy
M-S	Mott-Schottky
S-Q	Shockley-Queisser
SEM	Scanning Electron Microscopy
UV-Vis	Ultraviolet-Visible
IPCE	Incident Photon-to-Current Efficiency
RHE	Reversible Hydrogen Electrode
ABPE	Applied Bias Photon-to-current Efficiency
RT	Room Temperature

Appendix B

Résumé

L’introduction

Récemment en raison de la propriété unique sur la force motrice énorme grâce à la séparation effective des photoporteurs chargés, des oxydes ferroélectriques sont devenus plus en plus attractifs sur des applications de la conversion d'énergie solaire, par exemple, des photodétections, des photovoltaïques et des photocatalyses. Il y a 50 ans depuis la découverte de l'effet photovoltaïque (PV) sur les matériaux ferroélectriques, les cellules solaires ferroélectriques (FESC en anglais) sont de plus en plus étudiées en raison de nombreux avantages, comme la structure simple, la fabrication facile ainsi que les matériaux abondants et chimiquement stables. Dans les cellules solaires de diode *p-n* ou Schottky, la séparation des photoporteurs chargés est fortement dépendante du champ électrique incorporé. Différent avec celui-là, la polarisation ferroélectrique (FE) joue un rôle dominant sur la séparation et le transport des charges dans FESC. Les signes de photocourant et de phototension pourront être reversés par la commutation de la polarisation FE. FESC peuvent générer des tensions en circuit ouvert qui sont supérieures à leurs bandes interdites des matériaux FE (jusqu'à 30 V) qui dépassent la limite Schottky-Queisser observée dans les cellules semiconducteures conventionnelles.

Les dispositifs photovoltaïques ferroélectriques montrent un faible rendement en conversion d’énergie depuis longtemps alors qu’il y a une nouvelle percée majeure sur l’utilisation des matériaux multiferroïques. Les multiferroïques qui combinent deux fonctionnalités ferroïques (particulièrement FE et ferromagnétique ou ferroélastique) généralement possèdent un paramètre

magnétique en outre le FE et l'interaction entre les électrons qui pourra ajuster la bande interdite par l'ordre magnétique vers la valeur plus petite (ex., 2,6–2,7 eV pour $BiFeO_3$ et 1,4–2,4 eV pour Bi_2FeCrO_6) comparée aux matériaux FE (ex., 3,2–3,6 eV pour $Pb(Zr,Ti)O_3$ dopé au La et 3.2 eV pour $BaTiO_3$). Parmi ces multiferroïques, Bi_2FeCrO_6 (BFCO) qui est un cristal ordonné au site B avec la structure de double pérovskite est plus prometteur dans les applications PV et photoélectrochimiques (PEC) en raison de la bande interdite étroite, le coefficient d'absorption optique énorme ($2,5\times10^5$ cm^{-1}), la grande polarisation FE restante (55 μC cm^{-2} en direction pseudo-cubique [001] à la température ambiante) et aussi la grande magnétisation (160 emu cm^{-3}, 2 μ_B par unité de formule).

Nos études sur des dispositifs PV et PEC à base des couches minces BFCO dernièrement démontrent un rendement efficace en conversion d'énergie (de l'énergie solaire à électrique ou chimique). Dans le BFCO multiferroïque, une plus faible bande interdite et une plus grande polarisation FE prouvent respectivement efficacement promouvoir la génération et la séparation des photoporteurs chargés. Le BFCO monocristallin avec une grande ordonnance cationique Fe/Cr (0,9−5,1%) a montré la plus petite bande interdite (1,2−1,6 eV) accompagnée de la faible polarisation FE (5−25 μC cm^{-2}), ainsi démontrant donc un comportement de semiconducteurs. Malgré la plus grande absorption optique à la couche mince BFCO, le faible champ électrique interne en induisant par la faible polarisation FE pourra diminuer la puissance de séparation des photoporteurs chargés et augmenter la perte de la recombinaison qui va en plus réduire la performance des dispositifs PV. Ces résultats clairement montrent une relation entre les propriétés optique, FE et la structure cristalline des couches minces BFCO. Afin de bien exploiter les propriétés semiconductrices de BFCO dans les applications PV et PEC, une architecture de dispositif de *p-i-n* doit être développée. Donc, un absorbeur intrinsèque est sandwiché entre un

semiconductor fortement dopé par type-*p* et -*n*. L'absorbeur intermédiaire absorbe une certaine partie du spectre solaire, et les couches adjacentes (électrodes) sont nécessaires à extraire les transporteurs photogénérés pour le transport à la charge électrique externe.

La couche de type-*p* permet que les photons incidents est possible d'entrer dans la couche absorbante intrinsèque (*i*) du dispositif pour la conversion aux photoporteurs chargés. Cela s'exige que toutes les autres couches "passive" sauf les couches fonctionnelles du dispositif qui se trouvent sur le chemin des photons en traversant l'absorbeur ne devrait pas absorber ou refléter toute la lumière avant qu'ils atteignent à l'absorbeur intermédiaire. C'est-à-dire que la couche de fenêtre doit être transparente, par exemple, d'avoir une plus large bande interdite que l'absorbeur intermédiaire intrinsèque (*i*), et donc plus petit du coefficient d'absorption de la lumière en utilisant pour la conversion optique. La couche de fenêtre doit avoir la conduction électrique du trou pour transporter les trous photogénérés et bloquer les électrons photogénérés. En conséquence, l'oxyde de type-*p* doit être conducteur et transparent, donc, *p*-TCOs. De plus, il y a plein de choix des semiconducteurs de type-*n* qui sont structuralement appropriés au BFCO, comme le $SrTiO_3$ dopé au Nb avec la structure pérovskite qui est similaire à BFCO (double pérovskite) sur la constante de réseau cristallin en induisant un petit décalage du réseau cristallin, et donc conduisant un haut ordonné cationique Fe/Cr dans BFCO monophasé.

En outre, les propriétés relatives aux l'absorption de lumière large, le transfert de charge ultra rapide dans structure cristalline de double pérovskite et la polarisation FE accordable de BFCO permettent de fabriquer un photodétecteur réglable et sensitif avec la photoréponse rapide à base des couches minces FE.

Les objectifs :

Cette thèse est motivée par deux objectifs principaux:

(1) Synthèse et étude des propriétés physiques (ex., structurales, électriques et optiques) sur des couches minces de type-*p* (*p*-TCOs) avec les dopages variés;

(2) Fabrication et investigation des dispositifs à base des couches minces épitaxiales de BFCO multiferroïque pour des applications de la conversion d'énergie solaire efficace, y compris les photodétecteurs et les dispositifs PV et PEC.

Ces résultats obtenus dans cette thèse sont résumés par deux parties suivantes:

La première partie, nous avons synthétisé les couches minces d'oxyde de type-*p*, conductrices et transparentes, comme le $SrTiO_3$ dopé à l'indium avec les dopages variés, et systématiquement étudié des propriétés structurales, électriques et optiques sous différentes conditions de dépôt. On décrit cette partie par la suite:

Partie I. Les oxydes transparents et conducteurs de type-*p* (*p*-TCOs)

Chapitre 4 Les couches minces épitaxiales de $SrTiO_3$ dopé à l'indium de type-*p*

Ce chapitre présente les semiconducteurs de type-*p* transparents à base sur $SrTiO_3$ (STO). Les couches minces épitaxiales STO dopé à l'indium ($SrIn_xTi_{1-x}O_3$, $0 \leq x \leq 0.15$, ISTO) ont crû sur substrat $LaAlO_3$ (LAO) (100)-orienté et monocristallin sous des conditions de dépôt variées (ex., la température, la pression partielle d'oxygène) par la méthode hybride en combinant l'ablation du laser pulsé (PLD en anglais) et l'épitaxie par jets moléculaire (MBE en anglais). La température de la cellule Knudsen MBE était manipulée pour contrôler le dopage de l'indium dans la couche mince STO, et pour étudier l'effet du dopage d'indium sur les propriétés physiques (ex., structurales, optiques, électriques) de couches minces ISTO.

Des couches STO primitives ($SrIn_xTi_{1-x}O_3$, lorsque x=0) sont isolantes électriques. Dans **Figure R1**(a), la résistivité des couches minces ISTO diminue fortement lorsque x augmente de 0,005 à 0,1, et puis descend lentement lorsque x augmente de 0,1 à 0,15. La résistivité est quasi-stable à 10^{-2} Ω cm lorsque $x \geq 0{,}1$. Des mesures de l'effet Hall confirment que les porteurs chargés majeurs dans la couche ISTO sont des trous, c.-à-d., type-*p*. La concentration de trous est d'environ 0,7–3,1 × 10^{19} cm^{-3} et la mobilité est d'environ 0,7–5,2 cm^2/Vs à x varié entre 0,005 et 0,15.

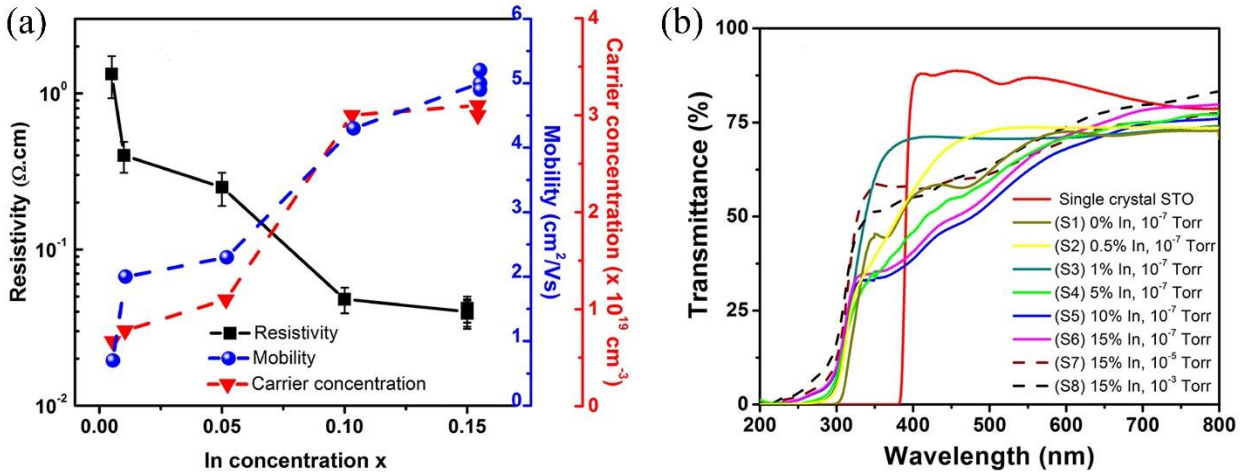

Figure R1. (a) Mesures de l'effet Hall sur couches minces ISTO avec concentration d'indium variée (x) représentant la résistivité, la mobilité et la concentration des trous. (b) Mesures de transmission de la lumière UV-Vis sur des couches minces ISTO (dopage d'indium au niveau de 0−15%) crûes sous différents paramètres de croissance.

Dans **Figure R**1(b), les spectres de transmission à la lumière ultraviolette-visible (UV-Vis.) sur des couches minces ISTO en 100 nm d'épaisseur montrent une nature transparente sur des couches minces ISTO au dopage de 0 à 15%, et comparés avec STO monocristallin. Les couches minces en croissant à 10^{-7} Torr d'oxygène manifestent d'être transparentes avec l'augment doux de transmittance de 70 à 75% quand le dopage d'indium monte de 0 à 15%. Des couches minces (x=0,15) en croissant à 10^{-7}, 10^{-5} et 10^{-3} Torr montrent la transparence similaire environ de 75%.

Le STO monocristallin indique une plus grande transparence que les autres, plus de 80%. Les résultats relatifs à ce chapitre sont publiés à:

***W. Huang**, R. Nechache, S. Li, M. Chaker, F. Rosei, Electrical and optical properties of transparent conducting p-type $SrTiO_3$ thin films. J. Am. Ceram. Soc. **99** [1], 226–233, 2016.*

La deuxième partie, on élabore des méthodes pour :

(a) Synthèse des couches minces épitaxiales de BFCO monocristallin et ordonné cationique, et comprendre leurs propriétés physiques (ex., structurales, électroniques, optiques et ferroélectriques);

(b) Évaluation sur le potentiel des applications de la conversion d'énergie solaire: photodétecteurs, photovoltaïques et photoélectrochimiques. On décrit par la suite pour cette partie:

Partie II. Les couches minces Bi_2FeCrO_6 (BFCO) pour la conversion d'énergie solaire

Chapitre 5 Photodiodes réglables et sensitifs à base des couches minces épitaxiales BFCO

Ce chapitre raconte la fabrication des photodiodes à base des couches minces BFCO multiferroïque par la technique PLD en décrivant dans la **Figure R2**(a). Une dépendance non-linéaire de la densité de courant (*J*) en fonction du champ électrique appliqué (*E*) selon la direction de *E*. La conductivité augmente rapidement avec croissance de l'intensité de la lumière de 50 à 100 mW cm^{-2} à n'importe quel *E*. Des courbes *J*(*E*) des dispositifs à la température ambiante (~300 K) montrent un comportement de diode. La densité de courant de saturation inversé est d'environ 0,22 μA cm^{-2} à −22,05 kV cm^{-1} mesurée sous l'illumination d'un soleil. Nous avons trouvé un facteur d'idéalité de diode sur n≈5,0 à 300 K et un champ électrique partiel de 9,80 kV cm^{-1}.

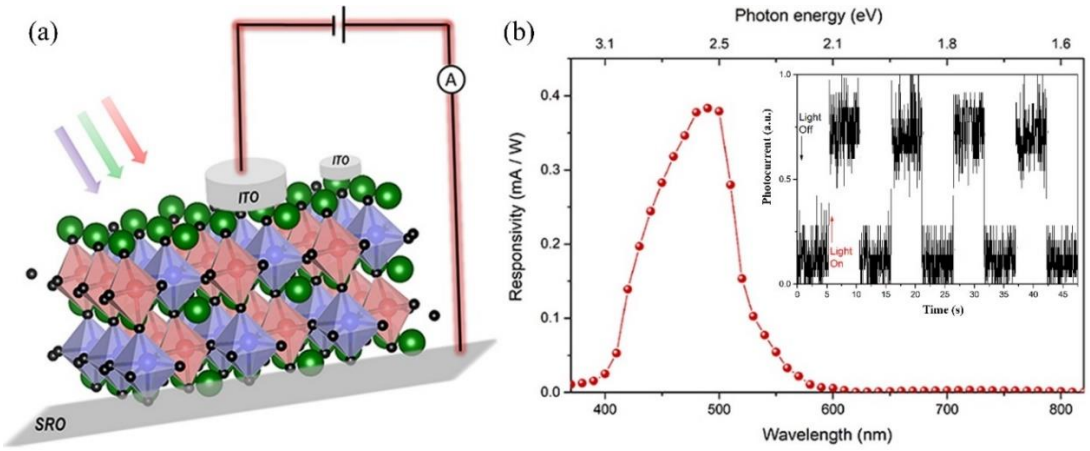

Figure R2. (a) Schéma d'une photodiode basée sur des couche minces BFCO. (b) Photoresponsivité des spectres à longueur d'onde de 500 nm à 0 V de la tension partielle. L'encart montre le photocourant varié avec la durée du temps.

Afin d'étudier l'effet de la polarisation sur des propriétés photo-électriques des couches minces BFCO multiferroïque, nous avons répété la mesure $J(E)$ après la couche BFCO était polarisée par différents impulsions de haute tension sous l'éclairage d'un soleil (100 mW cm^{-2}). L'effet de polarisation sur les courbes $J(E)$ du dispositif s'est expliqué au-dessous.

D'abord, on a trouvé un renforcement en densité de photocourant de court-circuit (J_{sc}) par deux ordres de grandeur par rapport à celle de l'état vierge (sans polarisation). J_{sc}≈+2 µA cm^{-2} en l'état positif lorsque J_{sc}≈+4 µA cm^{-2} après la couche polarisée par –15 V qui est renforcée par des centaines de fois en comparant à l'état vierge sous illumination. Cela indique que les dispositifs en l'état polarisé sous illumination montrent une propriété PV.

Ensuite, on constant que la forme des courbes $J(E)$ était changé et devenue presque symétrique au respect de: $J(E)|_{P_{up}} \approx -J(-E)|_{P_{down}}$ ce qui propose que l'alignement de la bande d'énergie dans le dispositif est inversé sur deux interfaces avec la commutation de la polarisation FE.

Figure R2(b) représente une photoréponse à la longueur d'onde d'entre 400 et 560 nm, et une chute à 500 nm. La photoresponsivité maximale sur 0,38 mA/W s'est trouvée autour de la longueur d'onde de 500 nm. L'encart montre une région de la photocourant variée avec la durée du temps, ce qui présente une réponse avec le temps d'environ de 68 ms dans la lumière visible. Les résultats relatifs à ce chapitre sont publiés à:

***W. Huang**, J. Chakrabartty, C. Harnagea, D. Gedamu, I. Ka, M. Chaker, F. Rosei and R. Nechache, Highly-Sensitive Switchable Heterojunction Photodiode based on Epitaxial Bi_2FeCrO_6 Multiferroic Thin Films, ACS Appl. Mater. Interface, **10** (15), 12790–12797, 2018.*

Chapitre 6 Les cellules solaires efficaces avec la hétérojonction *p-i-n*.

Cette partie présente la fabrication des dispositifs PV basée sur des couches minces BFCO en sandwichant entre le substrat STO dopé au Nb de type-*n* (NSTO) et la couche mince NiO de type-*p* par PLD. Pour comparaison, nous avons aussi fabriqué des couches minces BFCO en 120 nm d'épaisseur sous différents paramètres de croissance (ex., température du substrat, fréquence du laser, pression d'oxygène), et donc obtenu des bandes interdites variées de 1,7 à 2,4 eV correspondantes aux différents ordonnés cationiques Fe/Cr (R=0,29 – 0,68%).

Figure R3(a) manifeste les courbes *J-V* de hétérojonction *i-n* et *p-i-n* mesurées sous lumière d'un soleil. Cela montre la densité de courant de court-circuit (J_{sc}), la tension de circuit-ouvert (V_{oc}) et le facteur de remplissage (FF en anglais) qui sont 2,77 mA cm^{-2}, 0,44 V and 42%, respectivement, donc obtenue 0,5% de rendement en conversion d'énergie (PCE en anglais) pour hétérojonction *i-n*, et 7,97 mA cm^{-2}, 0,53 V, 48%, respectivement, et donc obtenue un PCE sur 2,0% pour hétérojonction *p-i-n*. V_{oc}, J_{sc} and PCE de hétérojonction *p-i-n* ont tout renforcé par facteurs de 1, 3 et 4 respectivement par rapport à celle de hétérojonction *i-n*. La photocourant est

renforcé fortement grâce à la contribution principale: la production PV qui provient de photoporteurs excités générés dans les couches minces BFCO et éventuellement l'augmentation de la force motrice par le champ électrique en promouvant par des régions de déplétion formées aux interfaces entre *p*-*i* et *i*-*n* dans la hétérojonction *p*-*i*-*n*.

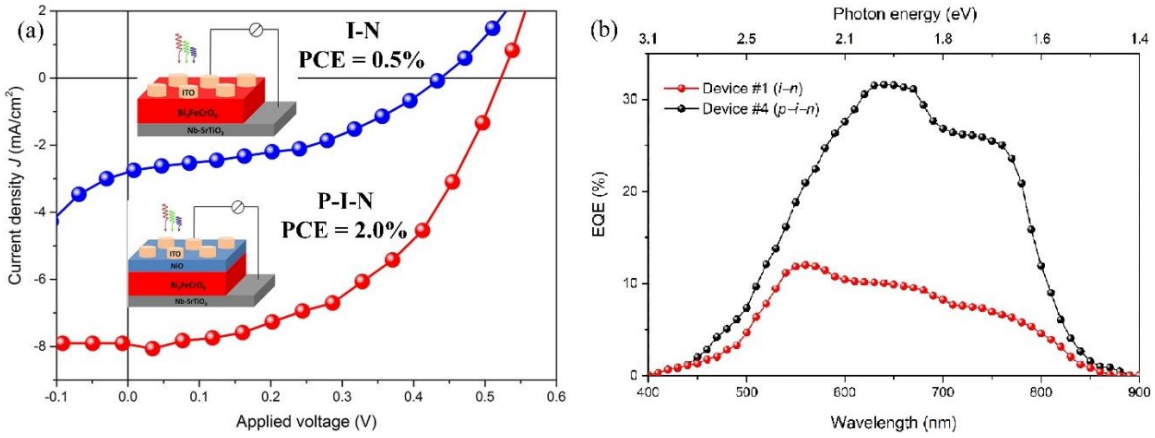

Figure R3. (a) Courbes relatives à la densité de courant (*J*) et la tension appliquée (*V*) sous illumination d'un soleil (AM 1.5G) avec dispositifs d'*i*-*n* (BFCO/NSTO) et de *p*-*i*-*n* (NiO/BFCO/NSTO). Les encarts montrent le diagramme des dispositifs. (b) Correspondantes aux courbes d'efficacité quantique externe (EQE).

Les mesures d'efficacité quantique externe (EQE) (**Figure R3**(b)) des dispositifs de hétérojonctions *i*-*n* et *p*-*i*-*n* ont été effectuées après la polarisation spontanée à la surface (appliqué +8 V à NSTO). La valeur d'EQE commence à augmenter à 850 nm, ensuite reste d'un plateau à 760 nm, puis jusqu'à un pic à 650 nm (1,9 eV) en atteignant la valeur maximale sur 32%. EQE maximale sue *p*-*i*-*n* est beaucoup plus élevée que celui de la jonction *i*-*n* (environ de 12%). Ces résultats démontrent clairement que la réponse PV est principalement donnée par photoporteurs excités dans BFCO et que la couche mince NiO dans la hétérojonction *p*-*i*-*n* a induit l'extraction de photoporteurs plus efficace. Les résultats relatifs à ce chapitre sont publiés à:

W. Huang, *C. Harnagea, D. Benetti, M. Chaker, F. Rosei and R. Nechache, Multiferroic Bi_2FeCrO_6 based p-i-n Heterojunction Photovoltaic Devices, J. Mater. Chem. A,* ***5****, 10355–10364, 2017.*

Chapitre 7 Photoanodes de hétérojonction basée sur des couches minces BFCO avec *p*-TCOs pour l'oxydation d'eau solaire.

À la fin, on représente des photoélectrodes de hétérojonction basée sur des couches minces BFCO recouvertes par la couche mince NiO qui est transparente et conductrice, et leur utilisation sur le craquage de l'eau solaire. La performance photoélectrochimique (PEC) et le renforcement de densité de courant ont été atteints, et la stabilité de photoanode *p*-NiO/*n*-BFCO était observée.

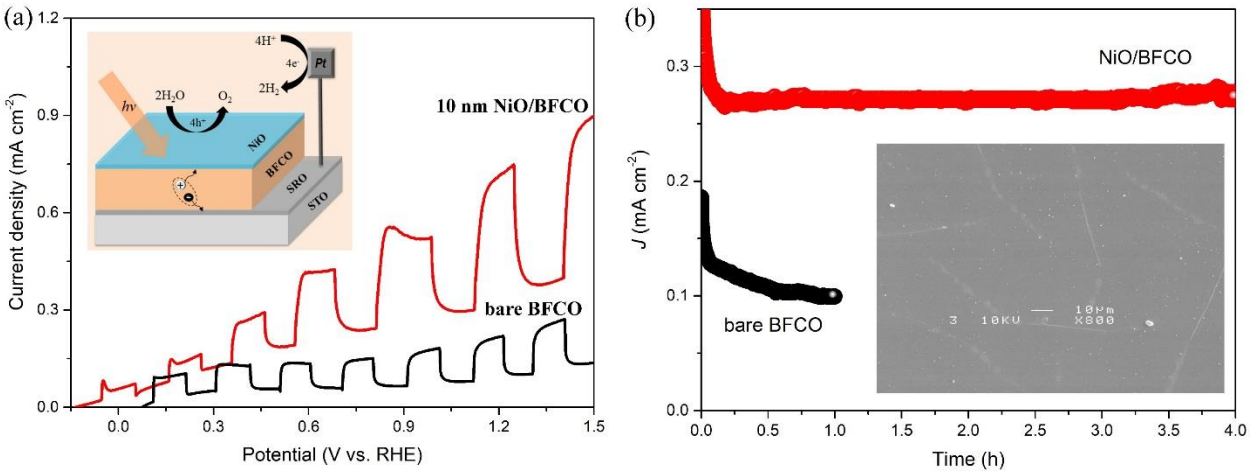

Figure R4. (a) Densités de courant versus tension appliquée (vs. RHE) sur photoanodes BFCO avec/sans la couche mince NiO en 10 nm d'épaisseur dans l'électrolyte de Na_2SO_4 (1 M) sous la lumière hachée; L'encart montre le schéma de photoanode de hétérojonction NiO/BFCO/SRO dans une cellule PEC pour dissociation de l'eau. (b) Stabilité de photoanodes BFCO avec/sans la couche mince NiO dans Na_2SO_4 (1 M) à +0,9 V vs. RHE sous AM 1,5 G. L'encart montre une image de MEB de la surface de NiO/BFCO après la mesure de la stabilité de 4 heures.

Figure R4(a) raconte que la photoelectrode BFCO sans la couche NiO à l'état vierge montre une densité de courant anodique (*J*) sur +0,1 mA cm^{-2} au +1,23 V (vs. Électrode Réversible à Hydrogène, RHE en anglais) après soustraction du courant à l'obscurité dans l'électrolyte de Na_2SO_4 (1 M) à pH 6.8. Le diagramme du dispositif de hétérojonction NiO/BFCO est montré dans l'encart de la **Figure R4**(a). Photoanodes de 10 nm NiO/BFCO ont atteint une *J* d'environ +0,4 mA cm^{-2} à +1,23 V (vs. RHE), ce qui est renforcée par quatre fois par rapport à la photoanode BFCO sans la couche protectrice NiO en raison de la réduction de recombinaison des photoporteurs dans hétérostructures NiO/BFCO/SRO.

Les mesures de stabilité ont été effectuées à l'aide de la chronoampérométrie fixé au potentiel de +0,9 V (vs. RHE) dans 1 M Na_2SO_4 sous l'illumination d'un soleil (AM 1,5G). Dans la **Figure R4**(b), la photodiode de 10 nm NiO/BFCO a démontré une légère réduction au début de mesure, puis s'est stabilisée à la densité de courant d'environ 0,27 mA cm^{-2} à l'opération continue de 4 heures. Alors que la densité de photocourant sur photoanodes BFCO sans la couche mince NiO a diminué de 34% au début de 5 minutes, et puis a descendu de 20% en reste 1 heure. L'encart montre une image de la surface de NiO/BFCO après la mesure de la stabilité de 4 heures enregistrée par la microscopie électronique à balayage (MEB). Il n'y a pas de modification importante sur la surface de NiO après le travail de 4 heures sous illumination. Les résultats relatifs à ce chapitre sont publiés à:

***W. Huang**, C. Harnagea, X. Tong, D. Benetti, S. Sun, M. Chaker, F. Rosei, and R. Nechache, Enhanced Photoelectrochemical Performance in Multiferroic Oxide Thin Films coated with p-Type Transparent Conducting Oxides, **Submitted**, 2018.*

En conclusion, tout d'abord, nous avons synthétisé des couches minces conductrices et transparentes (TCOs) de type-*p* à base de STO dopé au indium ($SrIn_xTi_{1-x}O_3$, $0 \leq x \leq 0.15$) sous différentes conditions de dépôt (pression d'oxygène, température du substrat, etc.) par une méthode hybride combinant PLD et MBE, et après systématiquement étudié leur propriétés structurales, électriques et optiques. Cela pourra être utilisé dans les photoélectrodes pérovskites, les optoélectroniques, etc.

Ensuite, nous avons réussi à synthétiser des couches minces épitaxiales BFCO multiferroïque crûs sur des substrats cristallins adéquates (STO, NSTO) sous différents paramètres de croissance (pression d'oxygène, température, fluence de laser, etc.) par PLD. Après, nous avons étudié des propriétés des couches minces BFCO pour la suite sur des dispositifs électroniques. Par exemple, chimiques, structurales, électriques, électroniques, optiques, ferroélectriques et ferromagnétiques.

Enfin, nous avons fabriqué des dispositifs basés sur des couches minces BFCO par PLD. Nous avons investigué des propriétés fonctionnelles des dispositifs à base de couches minces BFCO (ex., photoconductrices, photovoltaïques, photoélectrochimiques) pour des applications de la conversion d'énergie solaire correspondantes aux photodétecteurs, cellules photovoltaïques et photocatalyseurs. Ces travaux démontrent un potentiel énorme sur des matériaux multiferroïque, particulièrement sous la forme de couche mince épitaxiale, pour la conversion d'énergie solaire fiable, durable, et écologique.